Techniques for the Design and Analysis of Sodium Magnetic Resonance Imaging Sequences

by

Chengchuan Wu

ORCID: 0000-0002-9642-8970

A thesis submitted in total fulfillment for the
degree of Doctor of Philosophy

in the
Department of Biomedical Engineering
School of Engineering
THE UNIVERSITY OF MELBOURNE

March 2024

Abstract

Sodium is one of the most vital electrolytes in the human body, participating in fundamental roles such as homeostasis regulations and cell membrane transports. Sodium-23 magnetic resonance imaging (^{23}Na MRI) provides a novel technology to non-invasively measure the *in-vivo* ^{23}Na distribution. Recognising the potential implications of sodium MRI, the last decades have seen an increase in clinical studies utilising ^{23}Na MRI as the primary research tool.

^{23}Na MRI is particularly challenging due to the complex nuclear spin properties and the limited abundance of ^{23}Na in the human body. Although recent advancements have significantly improved the imaging outcome, ^{23}Na MRI still suffers from drawbacks including low signal-to-noise ratio, low spatial resolution and prolonged scan times. These drawbacks have hindered its practicality in clinical routines.

This work focuses on ^{23}Na MRI sequences and seeks to address the outstanding requirements in three parts.

In Part I, a consolidated formalism for the ^{23}Na spin dynamics in biological environments is derived, enabling straightforward and efficient simulations.

In Part II, a novel sequence, TriNa, is proposed for efficient acquisition of two types of ^{23}Na MRI contrast. The sequence also incorporates a post-processing correction for B_0 inhomogeneity artifacts.

Lastly, Part III demonstrates that 2D half-pulse projection reconstruction imaging can achieve higher image fidelity with a low number of total repetitions, compared to 3D hard-pulse projection reconstruction imaging. The findings thus confirm that 2D imaging frameworks are more suitable for rapid ^{23}Na MRI.

Acknowledgements

Throughout my PhD journey, there have been many people who have helped me. To them, I would like to express my great gratitude.

First and foremost, I would like to express my deepest gratitude to my excellent supervisors. Professor Leigh Johnston, I was very fortunate to have become one of your PhD students and conducted research under your guidance. Thank you for investing time in weekly project discussions over the past years. Your wisdom, generosity and patience have been the greatest support to my research and life. Dr. Yasmin Blunck, thank you for generously sharing your extensive knowledge and expertise that have guided me through projects from scratch, including programming sequences and operating the scanners. Your dedication and consistent encouragement have helped me overcome challenges along the way. I also would like to thank the advisory committee chair, Professor Peter Lee, for keeping my candidature on track.

I am very lucky to have had the opportunity to work in the Melbourne Brain Centre Imaging Unit. This group has been offering generous assistance and fostering a sense of belonging that has supported my research and enhanced my confidence. Special thanks to Rebecca Glarin, Brad Moffat, Didi Chi, Negin Yaghmaie, Ed Green and Braden Thai for helping the experiments run smoothly, especially during the special and challenging Covid era. I also would like to express my thanks to my colleagues I have worked alongside for their support and inspiring discussions: Myrte Strik, Igor Tyshchenko, Madeleine Bullock, Gihan Ruwanpathirana, Mara Quach and Warda Syeda.

Thanks for the love from my family and friends. My parents, Benxia Shang and Kejian Wu, have been encouraging me to explore further. Their trust in me is an invaluable gift. My deep thanks go to my friends: Ruqian Lyu, Bowen Zhang, Rena Ren, Shanlu Feng and Xin Li for the laughter and companionship. Thank you for being part of my life.

Declaration of Authorship

I, Chengchuan Wu, declare that this thesis titled, 'Techniques for the Design and Analysis of Sodium Magnetic Resonance Imaging Sequences' and the work presented in it are my own. I confirm that:

- The thesis comprises only my original work towards the Doctor of Philosophy except where indicated in the preface;
- due acknowledgement has been made in the text to all other material used; and
- the thesis is fewer than the maximum word limit in length, exclusive of tables, maps, bibliographies and appendices as approved by the Research Higher Degrees Committee.

Signed: 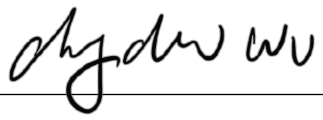

Date: 4 March 2024

List of Publications

The work presented in this thesis has produced the following publications and conference presentations.

Journal paper

- **Wu, C.**, Blunck, Y., Johnston, L.A. (2022). "The 'Spin-3/2 Bloch Equation': System matrix formalism of excitation, relaxation, and off-resonance effects in biological tissue", *Magnetic Resonance in Medicine*, 88(3):1370-1379.

Conference abstracts

- **Wu, C.**, Blunck, Y., Johnston, L.A. "Simultaneous acquisition of Spin-density-weighted and SNR-enhanced Fluid-attenuated ^{23}Na MRI images (SELA)", *Proceedings of 2020 ISMRM & SMRT Virtual Conference & Exhibition*, Online, 2020.
- **Wu, C.**, Blunck, Y., Johnston, L.A. "A Simulator for ^{23}Na Dynamics in Biological Tissue", *Proceedings of 2021 ISMRM & SMRT Annual Meeting & Exhibition*, Online, 2021.
- **Wu, C.**, Blunck, Y., Johnston, L.A. "2D ultra-short TE imaging for ^{23}Na MRI using half-pulse excitation", *Proceedings of Joint Annual Meeting ISMRM-ESMRMB & ISMRT 31st Annual Meeting*, London, 2022.
- **Wu, C.**, Blunck, Y., Johnston, L.A. "2D UTE imaging for rapid ^{23}Na MRI", *Proceedings of the 4th Annual Meeting of ANZ ISMRM Chapter*, Sydney, 2022.

Contents

List of Figures

List of Tables

Chapter 1

Introduction

Sodium is an essential element associated with human health. Nearly 100% of naturally occurring sodium is the sodium-23 (^{23}Na) isotope with a spin number of 3/2, which exhibits nuclear magnetic resonance (NMR) in response to specific magnetic field perturbations and emits electromagnetic waves. Such phenomenon has been utilised for non-invasive imaging since the 1980s (Ra, Hilal, Oh, & Mun, 1988), encouraged by the revolutionary and significantly successful in-vivo proton magnetic resonance imaging (^{1}H MRI). To date, ^{23}Na MRI can be performed on many clinical and preclinical MRI systems equipped with X-nuclei extensions, facilitating research on various parts of the human body such as the brain, cartilage, heart, muscle and kidney. In this chapter, sodium physiology with a special focus on the brain, ^{23}Na MRI methodology and application are reviewed.

1.1 Sodium in the Human Body

Sodium mostly exists as cations (Na^{+}) in the human body, including the brain, heart, kidneys, eyes and cartilage, participating in fundamental physiological activities such as osmotic pressure maintenance and neural action potential transmission (Madelin, Lee, Regatte, & Jerschow, 2014). Sodium is highly regulated in cells. A large concentration difference across the cell membrane is maintained by the collective effects of concentration gradient, cell membrane permeability, voltage potential and active transport. Sodium cannot pass the hydrophobic membrane interior which repels cations (Berg, Tymoczko, & Stryer, 2002). It can enter cells without energy consumption by passing through certain specific channels. This is called *facilitated diffusion* or *passive transport* (Berg et al., 2002). Sodium outflux, which is against the concentration gradient,

is produced by *active transport*. The sodium/potassium-ATPase (Na^+/K^+-ATPase) repeatedly exchanges three intracellular sodium ions with two extracellular potassium ions to actively control the ion concentration gradient across the membrane (Madelin, Lee, et al., 2014).

Extracellular sodium is one of the primary regulators of cellular osmolarity which underpins cell homeostasis. Changes in this pathway can trigger cascaded effects. For instance, a mild decrease in extracellular sodium concentration in brain grey matter reduces osmolarity, leading to neuron swelling, narrower gaps between neuron membranes and consequently making neuron firing more proactive (Somjen, 2004). A more pronounced decrease in extracellular sodium concentration inducing severe swelling can cause cell rupture.

In the nervous system, sodium is actively involved in neural signal transmission. The voltage potential across a neuron is -70 mV at the resting state. When a stimulus arrives, the permeability of the membrane changes, allowing sodium ions to enter the cell. The sodium influx increases voltage potential to about +30 mV. The neuron becomes active and propagates the stimulus downstream. After stimulation, Na^+/K^+-ATPase pumps restore sodium and potassium concentrations while the neuron returns to the resting state (Pohl, Wheeler, & Murray, 2013).

Sodium ions show various interactions and functions within the complex environments of the brain. Its concentration varies across brain cell types, measured to be 10 mM in neurons and 50 mM in astrocytes (Somjen, 2004). In cerebrospinal fluid (CSF) environments, there is a high sodium concentration, in the range of 135-150 mM (Madelin & Regatte, 2013), to counter the chloride cations and maintain electroneutrality. The CSF environment is relatively homogeneous for sodium, containing extremely low levels of macromolecules, such as proteins and proteoglycans, that interact with sodium cations. CSF occupies the brain ventricles, the subarachnoid spaces, where it forms channel networks and exchanges sodium and other substances with parenchyma, and the perivascular spaces which surround small arteries and arterioles penetrating tissue regions (K. R. Thulborn, 2018).

Sodium concentrations in the tissue interstitial space and the vascular space are similar to CSF. The interstitial space makes up 15-30% volume of the brain parenchyma (Syková & Nicholson, 2008; Gilles, Nagel, & Madelin, 2017). It is normally of narrow geometry between cell membranes with extracellular matrix, binding sites and metabolites (Syková & Nicholson, 2008). The vascular space occupies 3% of the brain volume and contains blood cells, plasma proteins and lipids (K. R. Thulborn, 2018).

Beyond the brain, sodium is also accumulated and regulated in the articular cartilage. Articular cartilage consists of $15-30\%$ of cross-linked glycosaminoglycans (GAG) which provide compressive elasticity (K. R. Thulborn, 2018). GAG contains negatively charged groups that attract sodium ions. The sodium concentration in articular cartilage is as high as 300 mM and linearly proportional to GAG concentration (Feldman, Stobbe, Watts, & Beaulieu, 2013; Madelin, Lee, Inati, Jerschow, & Regatte, 2010; Wheaton et al., 2004).

Sodium plays an important role in the kidney. During the filtration in the glomerulus, sodium, water, glucose and other small molecules and ions enter filtrates. Subsequently, sodium is actively reabsorbed into the medulla (Maril et al., 2006), forming osmotic pressure that reabsorbs water from filtrates (Pohl et al., 2013). In addition, sodium facilitates the co-transportation of glucose from the filtrate to the proximal tubule wall using sodium concentration gradients (Stolte, Hare, & Boylan, 1972).

1.2 The Development of ^{23}Na MRI Sequences

^{23}Na MRI is significantly more challenging than ^{1}H MRI. One of the biggest obstacles is that low ^{23}Na concentrations in biological environments limit the NMR signal strength. Further, the nature of ^{23}Na spin-3/2 leads to additional imaging challenges: observable magnetisation decays rapidly after excitation; low gyromagnetic ratio not only reduces the sensitivity of ^{23}Na magnetisation but also requires high-performance gradients and radiofrequency (RF) transmit coils. These factors have profoundly restricted sequence design and the applicability of ^{23}Na MRI.

Despite these challenges, advances have been made in pulse sequence development. ^{23}Na MRI shares many fundamental methodologies with ^{1}H MRI. Its sequence design must account for basic MRI requirments such as hardware constraints and safety regulations, but differences between these two modalities exist in terms of the imposed challenges. Sequences dedicated for ^{23}Na MRI have been proposed address these requirements more efficiently. Furthermore, specialised design strategies have been explored including novel image contrast, signal enhancement and acquisition optimisation, which have expanded the potential applications of ^{23}Na MRI. These advances will now be outlined.

1.2.1 Contrast Design and Sequence Optimisation

Concentration quantification

Quantitative ^{23}Na MRI has shown promising potential in clinical research (K. R. Thulborn, 2018). Spin density-weighted (SDW) sequences produce image intensities approximately proportional to the total sodium concentration (TSC, also known as apparent TSC). However, it is important to note that there are potential hardware and sequence limitations that may bias mapping results.

Firstly, ^{23}Na spins in cells and tissue interstitial spaces exhibit a bi-exponential relaxation, with the time constant of the fast component as short as hundreds of milliseconds (Blunck et al., 2018; Burstein & Springer Jr, 2019). To address this issue, ultra-short-TE (UTE) acquisition techniques are commonly used. However, since the relaxation is in a comparable time scale as the RF system dead time, during which the RF system switches from transmit to receive mode, part of the tissue signals has decayed before being detected.

Secondly, a relatively long repetition time (TR) is required to minimise T_1 weighting, particularly for the ^{23}Na in the fluid. Theoretically, fluid longitudinal magnetisation can recover 95% with a TR of 180 ms, according to measured T_1 values of around 60 ms at 7 T (Coste et al., 2019; Kratzer et al., 2021). However, such a long recovery time limits the efficiency of an SDW scan. In practice, the TR is slightly shortened to balance T_1 weighting bias and sequence efficiency.

In addition to the SDW sequence, TSC can also be imaged using a short-TR variable flip angle (VFA) method (Coste et al., 2019). The TSC image is derived after T_1-correction based-on the VFA model and its quality has been shown comparable to the one produced by a SDW sequence (Coste et al., 2019). Moreover, VFA sustains an extra benefit as it can provide an accompanying T_1 map.

Processing methods to associate image intensities with TSC values also affect the TSC accuracy. A linear model is usually employed in the post-processing step. The coefficients in the linear model can be estimated using intensities in the background, where the concentration is zero, and fluid regions such as CSF and vitreous humour, where a TSC value is presumed (Worthoff, Shymanskaya, & Shah, 2019; Gerhalter et al., 2021; Blunck et al., 2020). Calibration phantoms with known concentrations and ^{23}Na relaxation properties are also commonly used. The phantoms can be placed alongside the subject within the imaging field of view (FOV) (Huhn, Engelhorn, Linker, & Nagel, 2019; Inglese et al., 2010; Gast et al., 2021). However, it has been shown that such method can lead to quantification errors due to B_1 field inhomogeneity (Baron, Potze,

& Sijens, 2023). Alternatively, they can be scanned in an additional session to accommodate a larger phantom volume and to avoid field inhomogeneity-related errors (Lu, Atkinson, Claiborne, Damen, & Thulborn, 2010; K. Thulborn et al., 2016). Phantoms can also assist the T_1 relaxation correction for sequences with a shortened TR (Inglese et al., 2010).

Intracellular weighting

Dedicated sequence designs have been developed to detect intracellular sodium concentrations (ISC) which are deemed more sensitive to tissue abnormalities.

Triple quantum filtering (TQF) is a phenomenon that exclusively occurs in nuclei with a spin number greater than 1. A TQF sequence applies a group of phase-cycled pulses to selectively produce signals from the "slow environments", such as tissue (Hancu, Boada, & Shen, 1999). A more in-depth explanation on TQF will be provided in Chapter 2. Unfortunately, ^{23}Na TQF signals are weak and susceptible to B_0 inhomogeneity and stimulated echo interference. To improve scanning efficiency, the standard TQF sequence can be modified for an additional complimentary single-quantum signal acquisition (Fiege, Romanzetti, Mirkes, Brenner, & Shah, 2013). Furthermore, sophisticated phase cycling combinations are available for artifact reduction (Fleysher, Oesingmann, & Inglese, 2010; Fiege et al., 2013; Tanase & Boada, 2005b; Matthies, Nagel, Schad, & Bachert, 2010; Hoesl, Schad, & Rapacchi, 2020).

Fluid attenuation by inversion recovery (FLAIR) is also a viable option for ISC weighting. For an enhanced signal-to-noise ration (SNR), the inversion in ^{23}Na FLAIR is usually produced by a soft rectangular inversion pulse (SIRFLA), which significantly reduces the RF energy deposition to meet specific absorption rate (SAR) constraints (R. Stobbe & Beaulieu, 2005; Feldman et al., 2013; Wilferth et al., 2019). However, the SNR benefit comes at the expense of increased B_0 inhomogeneity artifacts in the SIRFLA sequence due to incomplete fluid suppression. In applications such as imaging the knee joint at 7 T, the susceptibility issue may be prominent due to local complex anatomy and abundant diamagnetic calcium. It has been demonstrated that an adiabatic inversion pulse, which is robust against the field inhomogeneities, can acquire an ISC-weighted image with adequate fluid suppression (Madelin et al., 2010). Furthermore, a shaped pulse optimised by control theory can be employed as a substitute for the adiabatic pulse, which effectively reduces SAR while maintaining similar fluid suppression efficacy (Lee, Xia, Madelin, & Regatte, 2016).

Parametric mapping

The spin-3/2 sodium exhibits bi-exponential relaxation in a "slow environment" (such as tissue) and mono-exponential relaxation in a "fast environment" (such as fluid). Since the bi-exponential decay is much stronger than the mono-exponential one, maps of relaxation time constants may reveal some information about the environment properties.

Parametric measurements in ^{23}Na MRI faces substantial difficulties. T_1 mapping sequences unavoidably impose T_1 weighting, which further attenuates the inherently weak ^{23}Na signal. Likewise, T_2 mapping sequences also suffer low signal issues as they necessitate refocusing pulses which delay readouts and increase power deposition. Therefore, these two measurements are deemed impractical and rarely used in ^{23}Na MRI.

In contrast, T_2^* mapping has received greater interest as it can be measured by multi-echo gradient echo (ME-GRE) sequences which are more SNR efficient. The T_2^* and simultaneous TSC mapping using a 3D radial ME-GRE sequence have been studied and optimised for sequence parameters including the number of echoes, readout length (Blunck et al., 2018) and echo spacing (Lommen et al., 2018).

The fitted models for the bi-exponential T_2^* relaxation have an influence on the result. Most studies use a model with a fixed ratio of 60:40 for the fast and slow components, implicitly assuming that each voxel consists of solely one compartment. However, this assumption may not hold as voxels in ^{23}Na MRI are generally coarse and heterogeneous. A gamma mixture model can account for the variation in the component fractions and has been shown to provide more accurate results than the fixed-ratio one (Syeda, Blunck, Kolbe, Cleary, & Johnston, 2019).

Additionally, parametric mapping can be performed by ^{23}Na MR fingerprinting (MRF). MRF is a sequence paradigm acquiring "randomly" weighted NMR signals from a randomised pulse train and reconstructing parametric images by matching the signals with a simulated dictionary. The novel ^{23}Na MRF approach has been shown to efficiently provide T_1, T_2^* and B_0 maps within a practical scan time, a task that was once considered to be time-prohibitive (Kratzer et al., 2020, 2021).

Techniques for sequence enhancement

Sequence parameter tuning for maximised SNR efficiency can be achieved by solving an optimisation problem to account for ^{23}Na nuclei properties, scanner limitations and safety constraints. Due to the complex spin-3/2 behaviour, the solutions are typically sought from ^{23}Na spin-3/2 simulations. Simulation-based optimisation has been applied

for SDW (R. Stobbe & Beaulieu, 2008b), TQF (Tsang, Stobbe, & Beaulieu, 2012) and SIRFLA sequences (R. Stobbe & Beaulieu, 2005).

Specialised ^{1}H-^{23}Na dual-nuclei imaging techniques have been developed to improve the efficiency of multi-modal scan protocols. It has been demonstrated that the ^{1}H signal and the ^{23}Na signal can be simultaneously acquired in one readout, producing ^{1}H MRF and ^{23}Na SDW image in a single scan and significantly reducing the total scan time compared to the standalone sequences (Yu, Madelin, Sodickson, & Cloos, 2020). The ^{1}H-^{23}Na dual-nuclei imaging technique can also be used to improve ^{23}Na image quality. For the purpose of motion correction, ^{1}H navigator scans can be inserted into a ^{23}Na SDW sequence to make use of the long system idle time between the end of a readout and the next RF excitation (Wilferth et al., 2022).

1.2.2 Acquisition Strategies for ^{23}Na MRI

Sampling efficiency optimisation

^{23}Na MRI sequences typically employ an isotropic non-Cartesian acquisition scheme, which collects the data in a circularly symmetric two- or three-dimensional k-space. Effects from the sampling pattern, T_2 relaxation and data weighting have an influence on the quality of the image (Lauzon & Rutt, 1996; Rahmer, Börnert, Groen, & Bos, 2006; Pipe, 2000). The basic 3D non-Cartesian form is projection reconstruction (PR, also known as radial) (Nielles-Vallespin et al., 2007), where the k-space trajectories start at the centre and extend radially to the peripheral k-space, allowing for immediate readout actuation after RF excitation that minimises the signal decay. Moreover, the concurrent relaxation becomes isotropic in 3DPR, preventing its blurring side effect from aggravating along one image orientation.

One of the limitations of 3DPR is the low sampling efficiency as it requires repeated acquisitions around 3 times more than conventional Cartesian sampling (Boada, Gillen, Shen, Chang, & Thulborn, 1997). The prolonged scan time can be reduced by 60% to 70% using the twisted projection imaging (TPI) modification, in which the radial lines are switched to spirals at a certain k-space radius (Boada, Gillen, et al., 1997). Such a twisting design has a high demand for the hardware. In FlexTPI, variable total gradient amplitude is employed to shorten the TPI readout duration under gradient slew rate constraints, achieving higher TPI imaging efficiency and quality (Lu et al., 2010).

The reduced SNR efficiency resulting from inhomogeneous k-space sampling also has a considerable impact. Improvement can be achieved by modifying the radial readout

gradient design for a more homogeneous data density distribution. This has been concurrently considered in TPI design (Boada, Gillen, et al., 1997). Another non-Cartesian acquisition for optimal SNR efficiency is the density-adapted projection reconstruction acquisition (DA-3DPR) (Nagel et al., 2009). DA-3DPR utilises a designated gradient waveform to distribute more sampling points at the distal part of the radial spoke such that the overall density is balanced in the k-space. In addition to the resultant sampling homogeneity, the gradient waveform is also beneficial for relaxation effect reduction, leading to SNR improvement by a factor of 1.8 compared to the standard 3DPR (Nagel et al., 2009).

Sampling density weighted apodization

Postprocessing filters serve multiple purposes in ^{23}Na MRI, such as noise and artifact suppression. It is worth noting that their benefits usually come with the cost of image resolution.

Acquisition techniques can be extended to include filtering, which is also known as sampling density weighted apodization (SDWA). SDWA can be realised by altering the sampling density of a sequence, similar to the methods that improve SNR by homogeneous sampling. For example, increasing the sampling density near the k-space centre in TPI can form an inherent low-pass filter, which has been shown to be more advantageous than the postprocessing counterpart in terms of SNR as the inherent filter avoids attenuating signals (Boada, Shen, Chang, & Thulborn, 1997; R. Stobbe & Beaulieu, 2008a). Likewise, SDWA can be implemented in DA-3DPR (Konstandin & Nagel, 2013). Notably, the relaxation effect has a considerable influence. With a long acquisition window augmenting tissue ^{23}Na relaxation, a post-acquisition filter can have superior performance to SDWA (Konstandin & Nagel, 2013).

Anisotropic imaging

Increasing the resolution of a 3D isotropic image results in a cubically decreased SNR. A slice thickness detached from the in-plane resolution by design can alleviate the heavy SNR penalty. Realising this function while preserving the UTE capability requires further sequence modification to the general centre-out 3D sequences, such as DA-3DPR (Nagel, Weber, Wolf, & Semmler, 2012). A dedicated 3D sequence acquisition-weighted stack of spiral (AWSOS) separates the gradient slice-phase encoding and the in-plane centre-out spiral encoding to enable voxel anisotropy (Qian, Zhao, Zheng, Weimer, & Boada, 2012). The readout starts immediately following the slice-phase encoding, which varies in duration as needed, resulting in slight blurring in the slice direction. These

two sequences have been demonstrated suitable for imaging muscles that have elongated structure (Utzschneider et al., 2021).

Another ^{23}Na imaging modality allowing for anisotropic voxels is 2D imaging. The reduction in image dimensions lowers the spatial encoding requirement, making 2D imaging suitable for rapid acquisition, for example, electrocardiographically gated ^{23}Na MRI (Konstandin & Schad, 2013). Specialised pulses, including the half pulse and the Fermi pulse, are required for UTE-enabled slice-selective excitation (Konstandin, Nagel, Heiler, & Schad, 2011; Konstandin & Schad, 2013). However, shaped excitation pulses have to be shortened to minimise ^{23}Na relaxation effect, consequently requiring a high RF transmit voltage and causing high SAR. These issues can be mitigated by the variable-rate selective excitation (VERSE) technique by concurrently tampering the RF pulse and gradient shapes (Conolly, Nishimura, Macovski, & Glover, 1988; Konstandin et al., 2011; Konstandin & Schad, 2013).

1.3 Chapter Outlines

Chapter 2 reviews the theoretical background. In Section 1, a brief quantum mechanical description of the spin-3/2 ^{23}Na NMR is provided, including excitation, relaxation and other spin dynamical behaviours. Section 1 is closely related to the spin-3/2 formalism in Chapter 3. In Section 2, an overview of MRI is provided, with a particular focus on spatial encoding methodologies. The section introduces the mathematical description of slice-selective excitation, including the theory of inherently focused half pulses which is implemented in Chapter 5. Furthermore, the theory of MRI acquisition is explained, focusing on 2DPR and 3DPR in Chapter 4 and Chapter 5.

Chapter 3 introduces a consolidated Spin-3/2 Bloch Equation (SBE) fully characterising the sodium spin dynamics in biological environments. Based on the formalism, simulations were performed on classical ^{23}Na MRI sequences and compared to other existing methods. The efficiency and accuracy of the SBE-based simulation have been demonstrated.

Chapter 4 presents a novel sequence design enabling simultaneous ^{23}Na SDW and FLAIR acquisition (TriNa). TriNa combines SDW and FLAIR sequences so that the SNR efficiency is improved. In addition, a post-processing method is proposed to address the B_0 inhomogeneity artifacts. TriNa has shown superior image quality and efficiency compared to standalone FLAIR sequences.

Chapter 5 concerns the image quality in rapid ^{23}Na MRI. The chapter assesses the half pulse selective excitation of 2D imaging and evaluates the performance of 2DPR and

3DPR. The comparison finds that using 2DPR is beneficial when image fidelity is sought within a limited scan time.

Chapter 2

Fundamental Theory

An overview of the important theory in ^{23}Na MRI is given in this chapter. The first part reviews key knowledge from the literature to understand the basics of ^{23}Na NMR. The second part summarises the basics of imaging methodology.

2.1 ^{23}Na NMR

The NMR phenomenon arises from the *nucleus spin*, which is one of the fundamental properties of a particle. This section follows the framework of quantum mechanics in reference to Levitt (2008); van der Maarel (2003a); Keeler (2010); Man (2006); Rooney and Springer (1991); Bowden and Hutchison (1986); Madelin, Lee, et al. (2014); Blunck (2018); R. Stobbe (2010).

States and Operators

The introduction of ^{23}Na NMR starts with the statements of two very important postulates in quantum mechanics:

> A quantum mechanical system consists of *states* which can be described by orthonormal (orthogonal and normalised) *wavefunctions*.
>
> The outcome of an observation is not deterministic. The observable physical quantity is associated with an operator, which is a function acting on a system, with its eigenvalues being the possible results.

Following the postulates, a nucleus Ψ can be represented by a linear combinations of orthonormal wavefunctions ψ

$$\Psi = \sum_n a_n |n\rangle \tag{2.1}$$

where $|n\rangle \equiv \psi_n$ represents the n-th state (wavefunction) and a_n is the coefficient associated with the probability of the state.

The "*bra*" ($\langle\cdot|$) and "*ket*" ($|\cdot\rangle$) are of Dirac notation. Equation 2.1 can be represented by a column vector, denoted by $|\Psi\rangle$ in the basis of $\{|n\rangle\}$:

$$|\Psi\rangle = \begin{pmatrix} a_1 \\ \cdots \\ a_n \\ \cdots \end{pmatrix}, \tag{2.2}$$

where $|n\rangle$ is a unit vector in the representation.

$\langle\Psi|$ is the adjoint of $|\Psi\rangle$:

$$\langle\Psi| = (|\Psi\rangle)^\dagger = \left(a_1^*, \ldots, a_n^*, \ldots\right), \tag{2.3}$$

where the asterisk (*) denotes the complex conjugates.

An operator $\hat{Q}$, conventionally denoted by a hat ascent ($\hat{}$), converts the system from one state to another, for example, $|\Psi_2\rangle = \hat{Q}\,|\Psi_1\rangle$. Following the formalism of the state vector, an operator can be represented by a matrix.

Spin is one of the fundamental states of a nucleus. A representation of the nucleus can be found by relating its spin to the z-component *angular momentum* $\hat{I}_z$. It can be shown that they form an eigensystem:

$$\hat{I}_z\,|I, M\rangle = M\,|I, M\rangle, \tag{2.4}$$

where the notation $|n\rangle$ is replaced by $|I, M\rangle$ detailing the spin states as distinctive wave functions of *spin quantum number* I and *azimuthal quanmtum number* M. The notation z is used according to the convention and also for the static magnetic field.

For the ^{23}Na spin, $I = 3/2$ whereas M has one of these values: $-\frac{3}{2}, -\frac{1}{2}, +\frac{1}{2}, +\frac{3}{2}$. According to postulates, the possible outcomes of $\hat{I}_z$ are enumerated by M, corresponding to $|I, M\rangle$, which is termed the *Zeeman eigenstate*.

Angular Momentum, Rotation and Magnetic Moment

As shown in Equation 2.4, the spin is mathematically related to the angular momentum of a nucleus. Hence, the angular momentum operator $\hat{\boldsymbol{I}}$ is of importance in the context. Note that the bold font indicates a vector physical quantity in the three-dimensional space.

One of the important properties of the $\hat{\boldsymbol{I}}$ is that its components follow *cyclic commutation*:

$$\left[\hat{I}_x, \hat{I}_y\right] = i\hat{I}_z, \tag{2.5}$$

which still holds when x, y and z in the equation cyclically permute, that is, $x \rightarrow y, y \rightarrow z, z \rightarrow x$. The square brackets, named *commutator*, is for the operation $[\hat{A}, \hat{B}] = \hat{A}\hat{B} - \hat{B}\hat{A}$.

The angular momentum operators are closely related to *rotation operators*, which is defined as

$$\hat{\boldsymbol{R}}(\beta) = \exp\left\{-i\beta\hat{\boldsymbol{I}}\right\}, \tag{2.6}$$

where β is the rotation angle.

Notably, they satisfy:

$$[\hat{R}_x, \hat{I}_x] = 0, \tag{2.7}$$

$$\hat{R}_x(\beta)\hat{I}_y\hat{R}_x(-\beta) = \hat{I}_y\cos\beta + \hat{I}_z\sin\beta. \tag{2.8}$$

Likewise, these relationships also obey the cyclic commutation.

The *nucleus magnetic moment operator* $\hat{\boldsymbol{\mu}}$ is another operator linked to the angular momentum,

$$\hat{\boldsymbol{\mu}} = \gamma\hat{\boldsymbol{I}}, \tag{2.9}$$

where γ is the gyromagnetic ratio. For ^{23}Na, $\gamma = 71 \times 10^6$ rad$\cdot$ s$^{-1}\cdot$ T^{-1} (Gast, Platt, Nagel, & Gerhalter, 2023).

Hamiltonian Operator

The nucleus can also be characterised in terms of its energy perspective through the Hamiltonian operator $\hat{H}$, which reveals the interactions between the spin and the local energy field.

The eigenvalues, ω_n, of a Hamiltonian specifies the value of energy for $|n\rangle$ of a system Ψ:

$$\hat{\mathcal{H}} |n\rangle = \omega_n |n\rangle , \tag{2.10}$$

$$\omega_n = \frac{\pi^2 n^2 \hbar}{2m}, \tag{2.11}$$

where the calligraphic font indicates that the Hamiltonian is in natural units, $\hat{\mathcal{H}} = \hat{H}/\hbar$. $\hbar$ is the reduced Plank's constant and m is the mass of the nucleus.

The energy is also associated with the dynamics of Ψ, described by the Schrödinger Equation:

$$\frac{\partial}{\partial t} |\Psi\rangle (t) = -i\hat{\mathcal{H}} |\Psi\rangle (t) . \tag{2.12}$$

The Hamiltonian operator comprises several components corresponding to various magnetic or electric fields.

Zeeman Hamiltonian

Suppose there is a strong static external magnetic field for the NMR experiment, with the magnitude denoted as B_0 and the direction denoted as z by convention.

The Hamiltonian operator representing the energy is found to be

$$\hat{\mathcal{H}}_0 = -B_0 \hat{\mu}_z = -\gamma B_0 \hat{I}_z . \tag{2.13}$$

According to Equation 2.11, $\hat{\mathcal{H}}_0$ describes four energy states, termed the Zeeman energy splitting,

$$\hat{\mathcal{H}}_0 |I, M\rangle = M\omega_0 |I, M\rangle , \tag{2.14}$$

where $\omega_0 = -\gamma B_0$ is the *Larmor frequency* of the spin.

Solving Equation 2.12 and Equation 2.13 gives the change of spin between an initial time point, t_0, and a later time point, t_1:

$$\begin{aligned} |\Psi\rangle (t_1) &= \exp\{-i\omega_0 (t_1 - t_0) \hat{I}_z\} |\Psi\rangle (t_0) \\ &= \hat{R}_z (\omega_0 (t_1 - t_0)) |\Psi\rangle (t_0) , \end{aligned} \tag{2.15}$$

which implies that the spin "rotates" about the z-axis under the static field. This is a phenomenon called *precession*.

Density Operator

In an experiment, it is an ensemble of spins that is observed. To describe them, an abstract operator termed *density operator* $\hat{\rho}$ is constructed where the matrix entries represent the probabilities of the states of the ensemble. The entry of the m-th row and n-th column can be found as

$$\rho_{mn} = \overline{a_m a_n^*}, \tag{2.16}$$

where the overline ($\overline{\cdots}$) means averaging over the ensemble. The entries ρ_{nn}, termed *populations*, represent the fractional population of the spin state $|I, M\rangle$ in the ensemble, whereas those ρ_{mn} with $m \neq n$, termed *coherences*, abstractly represents the mixed states. Additionally, the *coherence order* is defined as the difference of azimuthal quantum number M between the mixed states. For ^{23}Na, the density operator $\hat{\rho}$ is a 4-by-4 matrix consisting of 16 entries and up to 3rd-order coherences.

The density operator $\hat{\rho}$ finds the expectation value of an operator $\hat{Q}$ by

$$\langle \hat{Q} \rangle = \mathrm{Tr}\{\hat{\rho}\hat{Q}\}, \tag{2.17}$$

where $\langle \cdot \rangle$ is the expectation and Tr is the trace.

Equation 2.17 reveals the relevance of the quantised physical quantity to the experiment observation.

The dynamics of the density operator are governed by the Liouville-von Neumann Equation:

$$\frac{\partial \hat{\rho}}{\partial t} = -i[\hat{\mathcal{H}}, \hat{\rho}], \tag{2.18}$$

which has a solution

$$\hat{\rho}\,(t) = e^{-i\hat{\mathcal{H}}t}\,\hat{\rho}\,(0)\,e^{i\hat{\mathcal{H}}t}. \tag{2.19}$$

Notably, the solution with Zeeman Hamiltonian between t_0 and t_1 takes the form

$$\hat{\rho}\,(t_1) = \hat{R}_z\,(\omega_0\,(t_1 - t_0))\,\hat{\rho}\,(t_0)\,\hat{R}_z\,(-\omega_0\,(t_1 - t_0))\,. \tag{2.20}$$

Bulk Magnetisation

The notion of density operator links the physical quantities in the scope of quantum mechanics to those in classical electromagnetism. Of most importance in NMR is the *bulk magnetisation* $\mathbf{M}$ as it is closely related to the signal.

The bulk magnetisation is defined as the volume density of the total magnetic in the macroscopic level,

$$\mathbf{M} = \frac{N}{V}\mathrm{Tr}\{\hat{\rho}\hat{\boldsymbol{\mu}}\} = \frac{N\gamma}{V}\mathrm{Tr}\{\hat{\rho}\hat{\boldsymbol{I}}\}. \tag{2.21}$$

where N is the number of the nuclei and V is the volume.

At thermal equilibrium, the populations obey the *Boltzmann distribution* and the coherences vanish. The resultant density operator $\hat{\rho}_{\mathrm{eq}}$ is:

$$\hat{\rho}_{\mathrm{eq}} = \frac{1}{2I+1}\frac{\hbar\gamma B_0}{k_B T}\hat{I}_z, \tag{2.22}$$

where k_B is the *Boltzmann constant* and T is the temperature.

Equation 2.21 and Equation 2.22 indicate that the bulk magnetisation is pointed along the z-axis at thermal equilibrium, depicting the *polarisation* phenomenon.

Rotating Frame

Changing the reference frame can facilitate the description of complex quantum mechanical phenomena. In the previous sections, the view of an external observer is presumed, that is, the *laboratory frame*. The most essential movement of the spin observed in the laboratory frame is the precession about the z-axis. However, the spin will appear to be stationary when it is viewed in a *rotating frame* at the Larmor frequency. Therefore, transforming to the rotating frame helps simplify the movement and the corresponding mathematical description. According to the linear transformation, the laboratory frame $\{|n\rangle\}$ and the rotating frame $\{|n\rangle\}^{\star}$ satisfy

$$\{|n\rangle\}^{\star} = \hat{R}_z\left(\omega_0 t\right)\{|n\rangle\}, \tag{2.23}$$

where the symbol "$\star$" denotes the expression in the rotating frame.

The change of reference frame concurrently changes the expression in the new basis according to the linear transformation rule:

$$|\Psi\rangle^{\star} = \hat{R}_z\left(-\omega_0 t\right)|\Psi\rangle. \tag{2.24}$$

The observation of a stationary spin is reflected by expressing the spin in Equation 2.15 in the rotating frame

$$\begin{aligned}
\hat{R}_z^{-1}\left(-\omega_0 t_1\right)|\Psi\rangle^{\star}\left(t_1\right) &= \hat{R}_z\left(-\omega_0\left(t_1-t_0\right)\right)\hat{R}_z^{-1}\left(-\omega_0 t_0\right)|\Psi\rangle^{\star}\left(t_0\right) \\
|\Psi\rangle^{\star}\left(t_1\right) &= \hat{R}_z\left(-\omega_0 t_1\right)\hat{R}_z\left(-\omega_0\left(t_1-t_0\right)\right)\hat{R}_z^{-1}\left(-\omega_0 t_0\right)|\Psi\rangle^{\star}\left(t_0\right) \\
&= |\Psi\rangle^{\star}\left(t_0\right).
\end{aligned} \tag{2.25}$$

The same conclusion can be drawn from the dynamics, as Equation 2.12 in the rotating frame is expressed as

$$\begin{aligned}
\frac{d\,|\psi\rangle^{\star}}{dt} &= \left\{\frac{d}{dt}\hat{R}_z\left(-\omega_0 t\right)\right\}|\psi\rangle + \hat{R}_z\left(-\omega_0 t\right)\left\{\frac{d}{dt}|\psi\rangle\right\} \\
&= i\omega_0\hat{I}_z\,|\psi\rangle^{\star} - i\omega_0\hat{I}_z\,|\psi\rangle^{\star} \\
&= 0,
\end{aligned} \tag{2.26}$$

which implies $\hat{\mathcal{H}}_0^{\star} = 0$ and no precession in the rotating frame Schrödinger Equation.

Transforming an operator to the new basis is non-trivial, as the basis transformation $\hat{R}_z\left(t\right)$ is time-dependent. Nevertheless, all physical relationships and their equations hold regardless of the reference frame. In the remaining content of this thesis, all equations will be expressed in the rotating frame. For brevity, the "$\star$" symbol is dropped.

RF Pulse Excitation

In NMR experiments, RF radiation applies an oscillating magnetic field $\mathbf{B_1}$ perpendicular to $\mathbf{B_0}$. $\mathbf{B_1}$ precesses about $\mathbf{B_0}$ at Larmor frequency ω_0 to achieve resonance with the precession of the spin. The Liouville-von Neumann Equation in the rotating frame becomes

$$\frac{\partial\hat{\rho}}{\partial t} = i\left[\hat{\mathcal{H}}_1, \hat{\rho}\right], \tag{2.27}$$

where $\hat{\mathcal{H}}_1$ arises from the RF field interaction.

By default, $\mathbf{B_1}$ is assumed to be aligned with the x-axis of the rotating frame and thus $\hat{\mathcal{H}}_1$ takes the form

$$\hat{\mathcal{H}}_1 = -\omega_1\hat{I}_x, \tag{2.28}$$

where $\omega_1 = -\gamma B_1$ is named *nutation frequency*.

The solution to Equation 2.27 with an initial condition $\hat{\rho} = \hat{\rho}_{\text{eq}}$ and a *flip angle* $\theta = \omega_1 \tau$ is found to be

$$\begin{aligned} \hat{\rho}(\tau) &= \hat{R}_y(\theta)\,\hat{\rho}_{\text{eq}}\hat{R}_y(-\theta) \\ &= \frac{1}{2I+1}\frac{\hbar\gamma B_0}{k_B T}\left(-\hat{I}_y\cos\theta + \hat{I}_z\sin\theta\right). \end{aligned} \tag{2.29}$$

The transverse component $\hat{I}_y \propto \hat{M}_y$ precesses in the laboratory frame, inducing voltage signals in the receiver coil according to Faraday's Law.

Relaxation

Relaxation is the process when the spins gradually lose their coherence and return to the thermal equilibrium after a perturbation. The predominant driven force of ^{23}Na relaxation is the *electric field gradient* (EFG). The ^{23}Na spin interacts with the EFG through its quadrupolar electric moment, shifting the energy levels, which in turn change the precession frequency. The shifts vary over ^{23}Na spins and their bulk effect fundamentally gives rise to relaxation features that can be observed in an NMR signal spectrum.

The Hamiltonian corresponding to the EFG interaction can be decomposed into a static (first-order) component $\hat{\mathcal{H}}_{QS}$ and a time-variant (second-order) component $\hat{\mathcal{H}}_{QF}(t)$. $\hat{\mathcal{H}}_{QS}$ takes the form:

$$\hat{\mathcal{H}}_{QS} = \frac{1}{6}\omega_Q\left[3\hat{I}_z^2 - I(I+1)\right] \tag{2.30}$$

where ω_Q denotes the temporally and spatially averaged quadrupolar interaction frequency (or quadrupolar coupling frequency, quadrupolar beating frequency). $\hat{\mathcal{H}}_{QS}$ causes constant energy level shifts, manifested by a split NMR spectrum (Figure 2.1C). In the time domain, such splitting is equivalent to signal oscillation at ω_Q.

ω_Q is dependent on environmental factors including the orientation with respect to the static field, the levels of anisotropy and homogeneity. The orientation modulates the value of ω_Q (for more details, refer to Man (2006)). However, this factor has been commonly neglected in biological ^{23}Na MRI as including such effect in research models would greatly complicate research questions. The anisotropy of the environment results in structurally aligned EFG such that large ω_Q can be retained from spatial averaging. Conversely, the homogeneity negatively impacts ω_Q as it introduces variation and broadens the spectrum. The broadening in turn leads to shorter relaxation, as dictated by the Fourier relationship.

$\hat{\mathcal{H}}_{QF}(t)$ has a complicated form (for full details, refer to Man (2006)). It is related to the molecular Brownian motion in the surrounding environment. The time scale of motion,

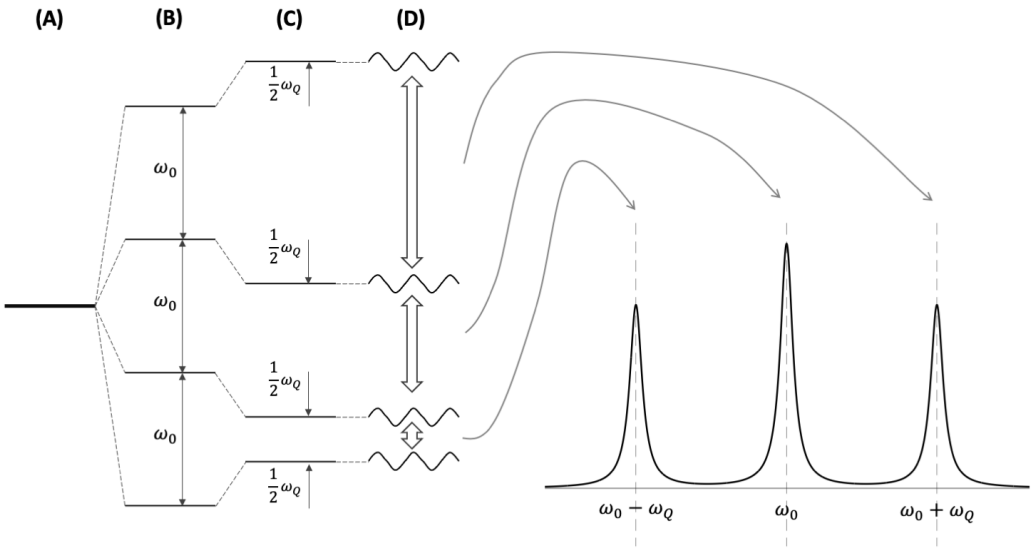

FIGURE 2.1: Graphical representation of the spin-3/2 energy levels. (A) No energy difference without an external magnetic field. (B) Spin states exhibit Zeeman splitting under $\hat{\mathcal{H}}_0$. (C) $\hat{\mathcal{H}}_{QS}$ shifts up $\left|\frac{3}{2}, -\frac{3}{2}\right\rangle$ and $\left|\frac{3}{2}, \frac{3}{2}\right\rangle$ by $\omega_Q/2$ while shifts down $\left|\frac{3}{2}, -\frac{1}{2}\right\rangle$ and $\left|\frac{3}{2}, \frac{1}{2}\right\rangle$ by $\omega_Q/2$, leading to a split NMR spectrum. (D) The time-varying $\hat{\mathcal{H}}_{QF}$ causes energy fluctuation and line widening. The block double arrows illustrate the first-order coherence (transverse magnetisation). This graph is adapted from Man (2006).

characterised by the *correlation time* τ_c, varies significantly among environments. In a slow-motion environment where $\omega_Q \tau_c \gg 1$, $\hat{\mathcal{H}}_{QF}(t)$ induces fluctuation in the energy levels and broadened peaks in the spectrum (Figure 2.1D). Such broadening by motion not only decreases the relaxation times but also gives rise to the biexponential character of ^{23}Na relaxation. In a fast-motion environment where $\omega_Q \tau_c \ll 1$, $\hat{\mathcal{H}}_{QF}(t)$ is too frequent to couple with spin rotations and therefore narrowed peaks can be observed, which corresponds to long relaxation.

In general, there are four types of environments (Figure 2.2):

- Type a: slow-motion ($\omega_0 \tau_c \gg 1, \omega_Q \tau_c \gg 1$), anisotropic and homogeneous environments such as single or liquid crystals. In a Type-a environment, the spectrum exhibits three peaks that are "motionally broadened" but distinctively separated by large ω_Q. Type-a environments are unlikely to exist in a biological system.

- Type b: slow-motion ($\omega_0 \tau_c \gg 1, \omega_Q \tau_c \gg 1$), anisotropic and inhomogeneous environments, which represents some biological tissue. Compared to a Type-a spectrum, the random distribution of EFG orientations results in reduced ω_Q and the broadening of the side peaks.

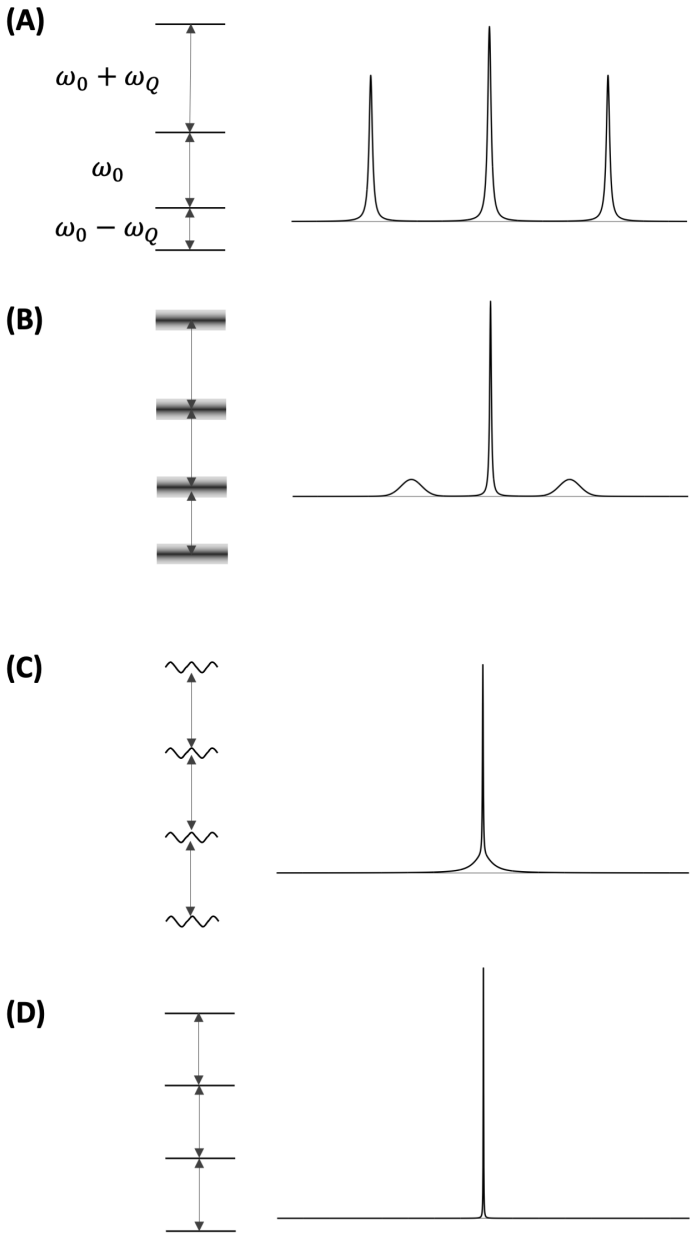

FIGURE 2.2: Illustration of the ^{23}Na energy levels in different environments on the left column and the corresponding NMR spectra on the right. (A) Type a: a large ω_Q alters the "satellite" energy level gaps and leads to distinctive peaks in the spectrum. (B) Type b: wide-spread distribution of EFG reduces ω_Q, narrowing the gaps and broadening the peripheral peaks. (C) Type c: ω_Q vanishes and energy levels fluctuate with dynamically changing EFG. The spectrum exhibits one motionally broadened peak. (D) Type d: EFG interaction vanishes due to fast motion. The spectrum exhibits one extremely narrow peak. This figure was generated for illustrative purpose, based on the result in Rooney and Springer (1991).

- Type c: slow-motion ($\omega_0\tau_c > 1, \omega_Q\tau_c \ll 1$) environments such as extracellular space where ^{23}Na interacts with large protein molecules. The increased temporal variation of EFG leads to smaller ω_Q ($\omega_Q = 0$ if it is also isotropic) and the spectrum peaks merge. Therefore, only one broadened peak can be distinguished.
- Type d: fast-motion ($\omega_0\tau_c \ll 1$) and isotropic ($\omega_Q = 0$) environments such as CSF. In this case, only one extremely narrow peak exists and the relaxation appears to be mono-exponential.

In Chapter 3, the formalism pertaining to ^{23}Na relaxation in the biological environments will be discussed.

Spherical Tensor Operator

Spherical tensor operators $\hat{T}$ are a set of spherical harmonics of *rank* n, *coherence order* q. A set of spherical tensor operators forms a complete basis for any operator, facilitating an elegant and concise description and providing an explicit matrix representation for the spin ensemble dynamics.

The components with non-zero order are conventionally converted into symmetric $\hat{T}_{n,q}(s)$ and antisymmetric $\hat{T}_{n,q}(a)$ combinations with q ranging from $0, \ldots, n$:

$$\begin{aligned} \hat{T}_{n,q}(s) &= \frac{1}{\sqrt{2}}\left(\hat{T}_{n,-q} + \hat{T}_{n,q}\right) \\ \hat{T}_{n,q}(a) &= \frac{1}{\sqrt{2}}\left(\hat{T}_{n,-q} - \hat{T}_{n,q}\right) \end{aligned} \tag{2.31}$$

Their relationships with the angular momentum operator are tabulated in the literature (c.f. Blunck (2018); Madelin, Lee, et al. (2014)). The most important ones are

$$\hat{I}_x = \sqrt{5}\hat{T}_{11}(a), \quad \hat{I}_y = i\sqrt{5}\hat{T}_{11}(s), \quad \hat{I}_z = \sqrt{5}\hat{T}_{10}. \tag{2.32}$$

For the representation of the spin ensemble, the tensor operator basis up to the third rank suffice for the ^{23}Na density operator:

$$\hat{\rho} = \sum_{n,q} c_{n,q}(s,a)\hat{T}_{n,q}(s,a), \tag{2.33}$$

where c is the coefficient.

The RF Hamiltonian and the static quadrupolar Hamiltonian are readily given as

$$\hat{\mathcal{H}}_1 = \sqrt{5}\omega_1 \hat{T}_{11}(a), \tag{2.34}$$

$$\hat{\mathcal{H}}_{QS} = \omega_Q \hat{T}_{20}. \tag{2.35}$$

A generalised matrix representation of the Liouville-von Neumann Equation will be derived in Chapter 3 using the tensor operator formalism.

2.2 ^{23}Na MRI

In this part, the gradient system, which can temporarily alter the magnetic field, plays an important role. This hardware is deeply connected to a mathematical concept *k-space*, defined as the Fourier representation of the physical space.

The section begins by explaining selective excitation, which involves spatial encoding during RF excitation and introduces the concept of *excitation k-space*. Subsequently, the mathematical model of acquisition encoding and the *acquisition k-space*, also often referred to as the *k-space* for short, are explained in one dimension. The chapter also provides examples of 2D k-space for rectilinear and radial acquisitions. The section refers the works including Pauly et al. (1989); R. Stobbe (2010); Brown, Cheng, Haacke, Thompson, and Venkatesan (2014); Lauzon and Rutt (1996); Bracewell and Bracewell (1986); Jackson, Meyer, Nishimura, and Macovski (1991); Tsai and Nishimura (2000).

Selective excitation

The description of selective excitation can be given by the *small tip angle approximation* theory. One of the assumptions stated in the theory is that no relaxation occurs during the small tip angle excitation. As it starts from the thermal equilibrium, only the rank-1 of the 16 spherical tensor operators, which represent the magnetisation, can be generated under this assumption. Therefore, the formalism becomes identical to the spin-1/2 Bloch Equation.

In the basic form of slice-selective excitation, a constant gradient $\mathbf{G}$ is applied, linearly varying the Larmor frequency ω across the space $\mathbf{r}$ by $\omega(\mathbf{r}) = \omega_0 + \gamma\,\mathbf{G}\cdot\mathbf{r}$.

An RF field with amplitude B_1 interacts with the spins as described by the following Bloch equation:

$$\frac{d}{dt}\begin{bmatrix} M_x \\ M_y \\ M_z \end{bmatrix} = \begin{bmatrix} -T_2^{-1} & \gamma \mathbf{G}\cdot\mathbf{x} & -\gamma B_{1,y} \\ -\gamma \mathbf{G}\cdot\mathbf{x} & -T_2^{-1} & \gamma B_{1,x} \\ \gamma B_{1,y} & -\gamma B_{1,x} & -T_1^{-1} \end{bmatrix}\begin{bmatrix} M_x \\ M_y \\ M_z \end{bmatrix} + \begin{bmatrix} 0 \\ 0 \\ \frac{M_0}{T_1} \end{bmatrix}. \tag{2.36}$$

The small tip angle approximation also assumes that the longitudinal magnetisation M_z is equal to the equilibrium magnetisation M_0, and solves the Bloch equation at the end of the slice selection process $t = T$. A simplified version for intuition is given as followed:

$$M_{xy}(\mathbf{x}, T) = i\gamma M_0 \int_{\mathbf{k}(t=0)}^{\mathbf{k}(t=T)} \frac{B_1(\mathbf{k})}{|\mathbf{G}(\mathbf{k})|} \exp(i\mathbf{x}\cdot\mathbf{k})\, d\mathbf{k}, \tag{2.37}$$

where the spatial frequency variable $\mathbf{k}$ is given as

$$\mathbf{k}(t) = -\gamma \int_t^T \mathbf{G}(s)\, ds. \tag{2.38}$$

Equation 2.37 forms a Fourier transform between the variables $\mathbf{x}$ and $\mathbf{k}$. The latter's domain is termed *excitation k-space*. Equation 2.38 states that excitation k-space is traversed time-reversely and ended at the origin at T.

The weight $B_1(\mathbf{k})/|\mathbf{G}(\mathbf{k})|$ in Equation 2.37 determines the slice profile $M_{xy}(\mathbf{x}, \mathbf{T})$. Basically, a truncated sinc RF field and a concurrent constant slice-selective gradient can be used to approximate a rectangular magnitude profile. However, the resultant weight is shifted in the excitation k-space, leading to phase dispersion in the slice profile after the Fourier transform. It is therefore required a succeeding refocusing gradient such that the weight can be centred at the origin for an in-phase M_{xy} at $t = T$.

There exist inherently refocused slice-selective excitation methods. The half-pulse excitation repeats the sequence twice, each with a slice selective gradient with the polarity opposite to each other. Since the gradients have opposite signs, each repetition scans and weights the excitation k-space from one end to the centre. The summation of the weights is equivalent to the corresponding full-pulse method described in the previous paragraph and therefore the slice profiles are identical, but the refocusing gradient has been minimised (2.3). Hence, the half-pulse excitation can reduce the delay between excitation and readout, which is beneficial for preserving the fast-decaying signal in ^{23}Na MRI.

1D imaging

A brief overview of spatial encoding during acquisition will be reviewed, starting with one-dimensional examples for simplicity. When the signal is ready for acquisition, the

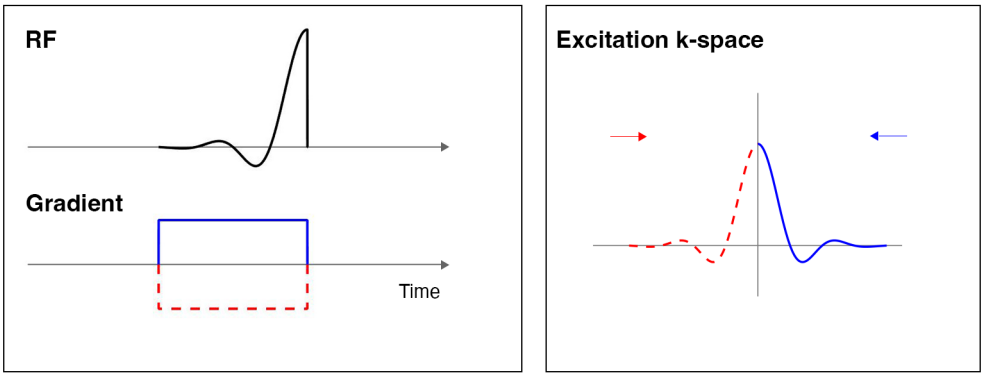

FIGURE 2.3: The half pulse excitation fulfils the excitation k-space weighting in two partitions, each starting at one end of the excitation k-space. Adopted from Pauly et al. (1989).

RF coil is then switched to the receive mode while the gradient is run in a designated scheme for spatial encoding. The execution of gradient traverse the *acquisition k-space*.

As a preparation step, define $t = 0$ at the point when the pulse ends; define the (*acquisition*) *k-space* as

$$\mathbf{k}(t) = \gamma \int_0^t \mathbf{G}(s)\, ds. \tag{2.39}$$

Comparing Equation 2.38 and Equation 2.39 reveals the inverse relationship between excitation and acquisition.

Consider the following scenario in one dimension: when the transverse magnetisation M_{xy} at *echo time (TE)* is ready for measurement, the gradient with constant gradient G plays out for spatial encoding. The modulated total magnetisation S across the dimension of x is a Fourier transform of M_{xy} to k-space:

$$S(t) = S(k) = \mathcal{F}\left\{M_{xy}(x,t)\right\} = \int_{-\infty}^{+\infty} M_{xy}(x,t) \exp(ixk)\, dx, \tag{2.40}$$

where $k = \gamma G t$. The time-dependent M_{xy} is subject to external and internal influences, such as off-resonance effect and transverse relaxation, which jointly act as a filter W during the modulation. This is explicitly modelled as

$$S(k) = \int_{-\infty}^{+\infty} W(k - k_{\mathrm{TE}})\, M_{xy}(x; \mathrm{TE}) \exp(ixk)\, dx. \tag{2.41}$$

For ^{23}Na magnetisation, especially those in slow-motion environments, the relaxation during the gradient period can be significant.

Since an MR imaged object is band-limited in x, $\mathcal{F}\left\{M_{xy}(x)\right\}$ spans an infinite extent in k-space. A gradient with duration T_{RO} reaches to the maximum frequency $k_m = \gamma G T_{\mathrm{RO}}$ and applies a rectangular window in k-space. The windowing corresponds to a sinc function in the image space with a main lobe of $\Delta x = \pi / k_m$ width, defining the *nominal image resolution*. The oscillations in the sinc function lead to *Gibbs ringing* artifacts.

While the gradient encodes the magnetisation, the RF coil is switched on to receive. The ADC samples at frequency $1/\Delta t$. Equivalently, the sampling takes place in k-space at $\Delta k = \gamma G \Delta t$:

$$S[n_k] = S(k) \times \sum_{n_k=-\infty}^{+\infty} \delta(k - n_k \Delta k). \tag{2.42}$$

The sampling theorem states that replicates of $s[n_x] = \mathrm{DFT}^{-1}\{S[n_k]\}$ in the image space are produced in Equation 2.42. To avoid replicates overlapping, the image FOV $= 2\pi/\Delta k$ has to be larger than the object size, referred to as the *Nyquist sampling criterion*.

A digital filter, denoted as $W[n_k]$, can be applied to the samples prior to the image reconstruction for purposes such as density compensation, Gibbs ringing suppression and noise reduction.

The inverse DFT reconstructs N-point samples to an N-point image

$$s[n_x] = \sum_{n_k=0}^{N-1} W[n_k]\, S[n_k] \exp\left(2\pi i \frac{n_x n_k}{N}\right). \tag{2.43}$$

Summarising the above process, the reconstructed image $s[n_x]$ is a period of the filtered, discretised and replicated $M_{xy}(x; \mathrm{TE})$.

The sampling can be characterised by the *point spread function (PSF)* while the overall process can be characterised by the *modulation transfer function (MTF)*.

Cartesian sampling

The equations in the previous subsection can be easily adapted to 2D or 3D sampling in a Cartesian (rectilinear) grid. An exemplary 2D formula is given here:

$$s[n_x, n_y] = \sum_{n_{k_x}=0}^{N_x-1} \sum_{n_{k_y}=0}^{N_y-1} S[n_{k_x}, n_{k_y}] \exp\left(2\pi i \left(\frac{n_x n_{k_x}}{N_x} + \frac{n_y n_{k_y}}{N_y}\right)\right). \tag{2.44}$$

The PSF is simply the n-dimensional combination of the 1D PSF.

To fully cover k-space without any crossover, the gradient usually pushes k to a starting point before the readout, then the acquisition scans a line in k-space. The preparation stage is called *phase encoding*, whereas the acquisition stage is called *frequency encoding*.

The fast decaying nature of ^{23}Na signal makes the MTF much blurry along the frequency encoding direction than the phase encoding direction.

Non-Cartesian sampling

Phase encoding-free, centre-out acquisition such as radial and spiral covers a disk area in 2D or a sphere in 3D. The operation connecting circularly symmetric image and k-space is the Hankel transform.

Let $\mathcal{H}$ denote the Hankel transform, $f(r)$ and $F(q)$ denote the Hankel transform pair, where r and q are the radius variable in the corresponding domain. Then

$$F(q) = \mathcal{H}\{f(r)\} = 2\pi \int_0^\infty f(r) J_0(2\pi r q)\, r dr, \tag{2.45}$$

$$f(r) = \mathcal{H}\{F(q)\} = 2\pi \int_0^\infty F(q) J_0(2\pi r q)\, q dq, \tag{2.46}$$

where J_n is the Bessel function of the n-th order.

The Bessel function $J_n(2\pi x)$ is the basis of the Hankel transform, like the unit circle $e^{i2\pi x}$ in the Fourier transform.

The following equations are two key Hankel transforms in 2D:

1. The Hankel transform of an infinitesimally thin ring:

$$\mathcal{H}\left\{\frac{1}{2}\delta(q-a)\right\} = \pi a J_0(2\pi a r). \tag{2.47}$$

2. The Hankel transform of a disk:

$$\mathcal{H}\left\{\mathrm{rect}\left(\frac{q}{2a}\right)\right\} = a\frac{J_1(2\pi a r)}{r}. \tag{2.48}$$

Here, $\mathrm{jinc}(r) = 2J_1(\pi r)/r$ is an analog to the sinc function.

As two examples closely relevant to the works in the later chapters, this subsection provided an introduction to 2D and 3D radial discrete sampling.

The 2D centre-out radial trajectory k_{2D} is parameterised by radius $r(t) = \gamma t\sqrt{G_x^2 + G_y^2}$ and azimuth $\theta = \tan^{-1}(G_y/G_x)$.

The 3D radial has an additional parameter φ for the polar angle. The parameters are defined by the gradient as

$$r(t) = \gamma t \sqrt{G_x^2 + G_y^2 + G_z^2} \tag{2.49}$$

$$\theta = \tan^{-1}\left(G_y / G_x\right) \tag{2.50}$$

$$\varphi = \cos^{-1}\left(G_z / \sqrt{G_x^2 + G_y^2 + G_z^2}\right). \tag{2.51}$$

The k-space is sampled radially per readout and azimuthally per repetition. One of the popular methods is Golden Angle Increment: $\theta_n = 2\pi n / \left(\sqrt{5}+1\right)$. The Nyquist criterion requires that the maximum space between two adjacent samples is smaller than 1/FOV. In 2D radial, the criterion is fulfilled on the circumference, with a maximum azimuthal distance $\Delta\theta$ satisfying $r_{max}\Delta\theta < 1/\text{FOV}$.

Sampling on a polar grid obtains a PSF whose main component is a jinc function and its replicated components exhibit various shapes. Moreover, aliasing might still exist even when the Nyquist criterion is met. These two properties makes the PSF different from the Cartesian one, whose replicates are identical and completely separated when fully sampled. In addition, the MTF of a radial scheme is isotropic since blurring effects are equal in all directions.

Density compensation

Prior to the reconstruction, k-space data requires proper weighting. An inhomogeneous sampling scheme comprises shift-variant delta functions, implicitly defined by the local density. Hence, a compensation function is needed to recover the sample density weights. Conversely, equidistant rectilinear sampling has inherent equal weighting for every sample and does not require density compensation.

For the radial sequences with uniformly-distributed azimuthal angles, the density compensation weightings can be found analytically

$$W_{2D}(\mathbf{k}) = ||\mathbf{k}||, \tag{2.52}$$

$$W_{3D}(\mathbf{k}) = ||\mathbf{k}||^2, \tag{2.53}$$

where the bold symbol indicates the discrete indices combination and $||\cdot||$ is the Euclidean norm.

Gridding reconstruction

MRI generally relies on the efficient Fast Fourier Transform algorithm for reconstruction with a practical computational cost. For non-Cartesian sampling, k-space data needs to be interpolated into a rectilinear grid, which is a process called "gridding".

There are several gridding methods. One is to convolve k-space with a shift-invariant gridding kernel C. It has been shown that a Kaiser-Bessel (KB) kernel is a practical choice for balanced accuracy and computation, which is given as:

$$C_{\mathrm{KB}}(n_k) = \frac{1}{V} I_0\left(\beta\sqrt{1-(2n_k/V)^2}\right), \tag{2.54}$$

where β and V are parameters of the kernel.

The density-weighted and gridded k-space becomes

$$S_{\mathrm{DG}}(n_k) = \left(\frac{S(n_k)}{W(n_k)} * C(n_k)\right) \cdot \text{Ш}(n_k), \tag{2.55}$$

where Ш denotes the comb function.

The final reconstructed image s_G can be obtained from the interim result after inverse FFT and de-apodization.

$$s_G(n_x) = \frac{\mathrm{FFT}^{-1}\{S_{\mathrm{DG}}(n_k)\}}{\mathrm{FFT}^{-1}\{CS_{\mathrm{DG}}(n_k)\}}. \tag{2.56}$$

Noise

Noise in the *in-vivo* MRI measurement arises from the physiological activities of the object and the random electron thermal movements in the scanner. The latter is of interest in this discussion.

Thermal noise energy is proportional to the temperature T and the effective resistance R of the measurement system, including the inherent resistor and the resistance from the loaded object. It is assumed to be "white", which means the energy is uniform across the frequency spectrum. During a readout, the ADC is tuned to a frequency bandwidth $BW = 1/\Delta t$, beyond which the noise is filtered out.

The variance of noise σ^2 is the quantity representing the energy and reflects the above factors in a physics model:

$$\sigma^2 = 4k_B TR \cdot BW. \tag{2.57}$$

For Cartesian sampling, it has been shown that the noise variance in a voxel will be $\sigma_i^2 = \sigma^2/N$ after reconstruction, where N is the number of voxels.

As for non-uniform sampling, density compensation can influence image noise. The variance in the image space is proportional to the integral of the density-compensated noise variance over k-space.

$$\sigma_i^2 \propto \frac{\sigma^2}{\int_K D\,(k)\,dk}, \tag{2.58}$$

where $D\,(k)$ is the density. According to the Cauchy-Schwartz inequality, $\int_K D\,(k)\,dk \leq \int_K 1dk = 1$, concluding that uniform sampling is the most efficient in suppressing image noise.

In conclusion, the technical review of the NMR and MRI theory from the signal generation to the image formation related to this thesis has been given in this chapter. The following chapters explore novel simulations, sequence designs and analysis for ^{23}Na MRI.

Chapter 3

The 'Spin-3/2 Bloch Equation': System Matrix Formalism of Excitation, Relaxation and Off-resonance Effects in Biological Tissue

3.1 Introduction

The sodium isotope ^{23}Na, with nearly 100% abundance, is the second largest NMR signal source in-vivo and offers great potential for non-proton imaging in clinical research studies as a sensitive biomarker of tissue viability and organ function (Madelin, Lee, et al., 2014; Madelin & Regatte, 2013; Ouwerkerk & Morgan, 2007). In particular, ^{23}Na MRI techniques targeting intracellular sodium are demonstrating promising outcomes: adiabatic inversion recovery (IR) has been used to quantify sodium in knee cartilage, with the potential to diagnose osteoarthritis (Madelin et al., 2013); simultaneous single-quantum- and triple-quantum-filtered imaging has been demonstrated in the prediction of gene mutation of cerebral gliomas (Shymanskaya et al., 2020).

Simulation is an important tool in ^{23}Na MRI sequence design and analysis, the basis of which is the chosen spin-3/2 dynamics formalism determining the mathematical expansion of the Liouville-von Neumann equation. Various formalisms have been derived, which were dependent on the motivation of the study; for simulations concerning sequences with short and strong RF pulses, a hard-pulse approximation is typically made to obtain a closed-form expression of the spin dynamics. These approaches model selected experiments such as triple-quantum filtering (TQF) (Tanase & Boada, 2005a; Fleysher et al., 2010; Hoesl et al., 2020) and steady-state free precession (Kharrazian & Jakob, 2006). For spin-3/2 dynamics under modulated RF pulses, the spin-1/2 Bloch Equation (BE) can be used as a first-order approximation (Kratzer et al., 2020; Madelin et al., 2010). While accurately describing the spin-3/2 behaviour in fast-motion environments such as fluid, the BE does not capture multiple-quantum coherences and the quadrupolar decay in slow-motion environments. In order to obtain a more accurate description that reduces approximation error of the simulations, a spin-3/2 formalism incorporating relaxation and excitation was proposed by Hancu et al (Hancu, van der Maarel, & Boada, 2000). This formalism has since been widely used to investigate the relaxation impacts on the signal (Hancu et al., 2000; Tsang et al., 2012), simulations of long pulses (R. Stobbe & Beaulieu, 2005; Feldman et al., 2013; Lee, Regatte, & Jerschow, 2009) and pulse trains (Gilles et al., 2017; Kratzer et al., 2021).

A key step in the derivation of an explicit formalism is the secularisation process in which the time dependency of the relaxation function is removed in order to obtain an expression for the relaxation. For spin-3/2 dynamics in condensed matter, secularisation has been carried out based on Redfield theory (Hancu et al., 2000; van der Maarel, 2003b, 2003a). This widely used derivation is confined to specific conditions, for example, on-resonance RF fields applied to anisotropic environments, and off-resonance RF applied to isotropic environments. It has remained unclear whether the secularised expression is valid under arbitrary conditions.

The purpose of the current chapter is to propose a generalised algebraic formalism representative of spin-3/2 systems in biological tissue, including relaxation during RF in isotropic and anisotropic media as well as a complete consideration of off-resonance effects in the secularisation process. We consolidate the treatment based on the irreducible spherical tensor operator (ISTO) and compile previously specific and isolated forms into a generalised system matrix equation, which we herein refer to (albeit somewhat facetiously) as the 'Spin-3/2 Bloch Equation' (SBE), with obvious analogy to the BE algebraic model of bulk magnetisation in biological tissue for spin-1/2 nuclei. The SBE system matrix enables full simulation of spin-3/2 dynamics in any numerical environment with a single call to a numerical integration function, obviating the need for piecewise treatment of excitation, relaxation and off-resonance embedded in previous ISTO-based simulators (Madelin, Lee, et al., 2014; Kratzer et al., 2021). While the demonstrations and discussion of SBE are focused on ^{23}Na imaging, the formalism can also apply to other MR-observable spin-3/2 nuclei, such as ^{35}Cl and ^{39}K.

The properties of the SBE are expounded by the generation of three types of ^{23}Na MRI sequences: soft rectangular pulse inversion, adiabatic inversion and triple-quantum filtering. This demonstrates the broad applicability of the proposed SBE framework across a wide range of sodium pulse sequences and provides insight into the deviation of the spin-3/2 system dynamics from their spin-1/2 system counterpart. Accuracy, computational efficiency and generalisability of SBE simulations are illustrated through MATLAB-based comparison with the Madelin, Lee, et al. and Kratzer et al. ISTO-based simulators.

3.2 Theory

In this work, all physical quantities are described in the RF rotating frame. The dynamics of the density operator, $\hat{\rho}$, can be described by the master equation incorporating the Redfield relaxation function, $\hat{\hat{\Gamma}}$ (Chapman et al., 2010),

$$\frac{d}{dt}\hat{\rho}(t) = -i[\hat{H}_D, \hat{\rho}(t)] - \hat{\hat{\Gamma}}\left(\hat{\rho}(t) - \hat{\rho}_0\right), \tag{3.1}$$

where $\hat{\rho}_0$ denotes the density operator at thermal equilibrium and $\hat{H}_D$ denotes the Hamiltonian of deterministic propagation, consisting of three terms,

$$\hat{H}_D = \hat{H}_\Delta + \hat{H}_1 + \hat{H}_{QS}. \tag{3.2}$$

Here, $\hat{H}_\Delta$, $\hat{H}_1$ and $\hat{H}_{QS}$ derive from the effective static magnetic field, the RF field and the time-averaged quadrupolar electric field gradient (EFG), respectively.

The relaxation function describes the interaction with the fluctuating quadrupolar Hamiltonian, $\hat{H}_{QF}$ (van der Maarel, 2003b),

$$\hat{\hat{\Gamma}}\left(\hat{\rho}(t)-\hat{\rho}_0\right)=\int_0^\infty\left[\hat{H}_{QF}(t),\left[\exp\left\{-i\hat{H}_D\tau\right\}\hat{H}_{QF}(t-\tau)\exp\left\{i\hat{H}_D\tau\right\},\hat{\rho}(t)-\hat{\rho}_0\right]\right]d\tau. \tag{3.3}$$

The SBE is a matrix representation of the master equation, Eq. 3.1,

$$\frac{d}{dt}\mathbf{P}=\mathbf{L}\mathbf{P}+\mathbf{C}. \tag{3.4}$$

where $\mathbf{L}$ is the system matrix and $\mathbf{C}$ the offset vector arising from $\hat{\rho}_0$ for system state $\mathbf{P}$ (i.e. the vector representation of $\hat{\rho}$). ISTO has been chosen as the basis for Eq. 3.4. The orthonormal unit tensor operator, denoted as $\hat{T}_{lm}$, represents the component of rank l and coherence m. A set of 16 ISTOs, with $l=0,1,2,3$, $m=1,\ldots,l$, form a complete space for spin-3/2. Furthermore, we can transform the ISTOs into the symmetric (s) and antisymmetric (a) combinations, by

$$\hat{T}_{lm}(s)=\frac{1}{\sqrt{2}}\left(\hat{T}_{l-m}+\hat{T}_{lm}\right) \tag{3.5a}$$

$$\hat{T}_{lm}(a)=\frac{1}{\sqrt{2}}\left(\hat{T}_{l-m}-\hat{T}_{lm}\right), \tag{3.5b}$$

so that $\hat{T}_{11}(a)$, $\hat{T}_{11}(s)$ and $\hat{T}_{10}$ are proportional to the x-, y- and z-magnetisation, respectively. Moreover, as far as most NMR and MRI applications are concerned, we can omit the $\hat{T}_{00}$ because it has no contribution to the contrast in an isolated spin ensemble. Here, we define the basis for Eq. 3.4 as

$$\begin{aligned}\{&\hat{T}_{10},\hat{T}_{11}(a),\hat{T}_{11}(s),\hat{T}_{20},\hat{T}_{21}(a),\hat{T}_{21}(s),\hat{T}_{22}(a),\hat{T}_{22}(s),\\&\hat{T}_{30},\hat{T}_{31}(a),\hat{T}_{31}(s),\hat{T}_{32}(a),\hat{T}_{32}(s),\hat{T}_{33}(a),\hat{T}_{33}(s)\}.\end{aligned} \tag{3.6}$$

The SBE system matrix $\mathbf{L}$ is parameterised by RF amplitude (nutation frequency), $\omega_1(t)$, the initial RF phase, ϕ_0 with reference to the x′-axis, off-resonance frequency, $\omega_\Delta(t)$, time-average residual quadrupolar frequency, ω_Q, and spectral densities, J_0, J_1 and J_2. Entries of $\mathbf{L}$ are colour-coded in Figure 3.1 in order to provide intuitive understanding of the origins of the terms.

In order to present a derivation of this formulation of $\mathbf{L}$, consider the decomposition of the system matrix,

$$\mathbf{L}=\mathbf{D}+\mathbf{R}, \tag{3.7}$$

into the commutation component, $\mathbf{D}$, and the relaxation component, $\mathbf{R}$.

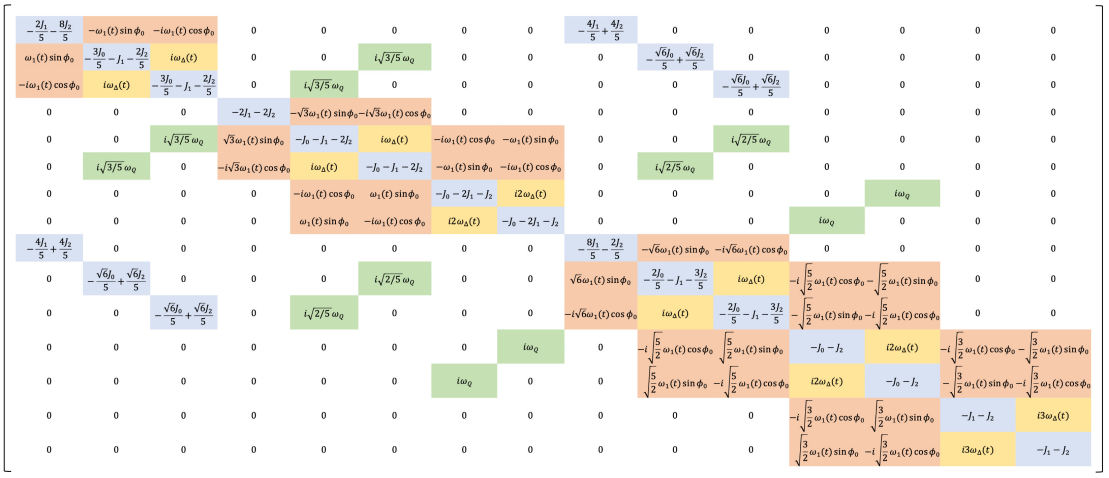

FIGURE 3.1: The SBE system matrix, $\mathbf{L}$, colour-coded to indicate the source of terms: Red-shaded entries are associated with RF excitation; Yellow-shaded entries are off-resonance terms; Green-shaded terms are associated with residual quadrupolar oscillation; Blue-shaded terms are associated with the fluctuating quadrupolar interaction.

3.2.1 The Commutation Component, D

The commutation matrix, $\mathbf{D}$, contains the deterministic spin dynamics, i.e. nutation, free precession and the time-average quadrupolar coupling. By definition,

$$\begin{aligned}\mathbf{D} &\triangleq -i[\hat{H}_D, \mathbf{E}] \\ &= -i\left[\sqrt{5}\omega_\Delta \hat{T}_{10} + \sqrt{5}\omega_1 e^{i\phi_0}\hat{T}_{11}(a) + \omega_Q \hat{T}_{20}, \mathbf{E}\right] \\ &= -i\left[\sqrt{5}\omega_\Delta \hat{T}_{10}, \mathbf{E}\right] - i\left[\sqrt{5}\omega_1 e^{i\phi_0}\hat{T}_{11}(a), \mathbf{E}\right] - i\left[\omega_Q \hat{T}_{20}, \mathbf{E}\right],\end{aligned} \tag{3.8}$$

where $\mathbf{E}$ is the identity matrix and is equivalent to the sum of the ISTO units. The matrix form of $\mathbf{D}$ is obtained by expansion of the commutators using commutation laws (Bowden & Hutchison, 1986, 1986; van der Maarel, 2003b).

The non-zero elements of $\mathbf{D}$ are identified in Figure 3.1 by shading: off-resonance precession (yellow), nutation (red), and static quadrupolar coupling (green).

3.2.2 The Relaxation Component, R

The relaxation function takes the following form with $\hat{H}_{QF}$ expressed in the tensor operator basis (Hancu et al., 2000):

$$\begin{aligned}\hat{\hat{\Gamma}}(\hat{\rho}) = -\int_0^\infty \sum_{m=-2}^{2} &\left[\hat{T}_{2m}, \left[e^{-i\hat{H}_D\tau}\hat{T}_{2m}^\dagger e^{i\hat{H}_D\tau}, \hat{\rho}\right]\right] \\ &\chi^2\langle\left[F_{2m}^*(t) - \left\langle F_{2m}^*\right\rangle\right]\left[F_{2m}(t-\tau) - \langle F_{2m}\rangle\right]\rangle e^{im\omega_r\tau}d\tau,\end{aligned} \tag{3.9}$$

where $\hat{T}^{\dagger}_{2m} = (-1)^m \hat{T}_{2-m}$, χ is the quadrupolar coupling constant, F_{2m} is the EFG tensor component, ω_r is the frequency of the rotating frame with respect to the laboratory frame, and $\langle\cdot\rangle$ and $*$ denote motion average and complex conjugation, respectively.

The integral in Eq. 3.9 is intractable except in certain cases. To the best of our knowledge, there is no matrix representation in the literature for the generalised case when $\hat{H}_\Delta$, $\hat{H}_1$ and $\hat{H}_{QS}$ co-exist. Here, we demonstrate that, given any practical $\hat{H}_D$ for ^{23}Na NMR in biological tissue environments, $\mathbf{R}$ has the same form as the case when $\hat{H}_D$ is absent, resulting in the relaxation matrix given by the blue shaded entries in Figure 3.1.

To demonstrate that relaxation rates are decoupled from the RF field, off resonance and anisotropy of the environment for ^{23}Na spin systems in biological tissue, consider the spectral density (van der Maarel, 2003b),

$$J(\omega) = \frac{(2\pi)^2}{20} \frac{\chi^2 \tau_c}{1 + (\omega\tau_c)^2}, \tag{3.10}$$

where τ_c is the correlation time. $J(\omega)$ has been shown to be a good approximation to the integral (van der Maarel, 2003b)

$$J(\omega) \approx \int_0^\infty \chi^2 \langle \left[F^*_{2m}(t) - \left\langle F^*_{2m} \right\rangle\right] \left[F_{2m}(t-\tau) - \langle F_{2m}\rangle\right] \rangle e^{i\omega\tau} d\tau. \tag{3.11}$$

This approximation will be used in the simplification of the relaxation function, Eq. 3.9. Considering now the argument of the double commutator of the relaxation function, the term $e^{-i\hat{H}_D\tau}\hat{T}^{\dagger}_{2m}e^{i\hat{H}_D\tau}$ represents the evolution of $T^{\dagger}_{2m}$ under the influence of $\hat{H}_D$. The corresponding dynamic equation is

$$\frac{d}{dt}\mathbf{T} = \mathbf{D}\mathbf{T}, \tag{3.12}$$

where $\mathbf{T}$ is an arbitrary quantity in ISTO space. The term $e^{-i\hat{H}_D\tau}\hat{T}^{\dagger}_{2m}e^{i\hat{H}_D\tau}$ is equivalent to the integral of Eq. 3.12 over $[0,\tau]$ with the initial condition $\mathbf{T}(0) = \hat{T}^{\dagger}_{2m}$. Note that $\mathbf{D}$ is skew-Hermitian and is therefore diagonalisable with purely imaginary eigenvalues. Eq. 3.12 can be rewritten as

$$\frac{d}{dt}\mathbf{T} = \mathbf{Q}^{-1} \begin{bmatrix} i\lambda_1 & & \\ & \ddots & \\ & & i\lambda_{15} \end{bmatrix} \mathbf{Q}\mathbf{T}, \tag{3.13}$$

where λ_k's are the eigenvalues and $\mathbf{Q}$ is the eigenvector matrix. By defining $\left[q_{1,s}, \ldots, q_{15,s}\right]^\top$ as the s-th column of $\mathbf{Q}$ corresponding to the initial condition such that $\mathbf{T}_s = \hat{T}_{2m}$, we

obtain the expression of the term $e^{-i\hat{H}_D\tau}\hat{T}_{2m}^{\dagger}e^{i\hat{H}_D\tau}$ in the $\{\hat{T}_{lm}\}$ basis,

$$\begin{aligned} e^{-i\hat{H}_D\tau}\hat{T}_{2m}^{\dagger}e^{i\hat{H}_D\tau} &= \mathbf{Q}^{-1}\begin{bmatrix} (-1)^m q_{1,s}e^{i\lambda_1\tau} \\ \vdots \\ (-1)^m q_{15,s}e^{i\lambda_{15}\tau} \end{bmatrix} \\ &= \frac{1}{\det(\mathbf{Q})}\begin{bmatrix} Q_{1,1} & \dots & Q_{15,1} \\ \vdots & \ddots & \vdots \\ Q_{1,15} & \dots & Q_{15,15} \end{bmatrix}\begin{bmatrix} (-1)^m q_{1,s}e^{i\lambda_1\tau} \\ \vdots \\ (-1)^m q_{15,s}e^{i\lambda_{15}\tau} \end{bmatrix} \\ &= \frac{1}{\det(\mathbf{Q})}\begin{bmatrix} (-1)^m \sum_k Q_{k,1}q_{k,s}e^{i\lambda_k\tau} \\ \vdots \\ (-1)^m \sum_k Q_{k,15}q_{k,s}e^{i\lambda_k\tau} \end{bmatrix} \\ &= \sum_{l=1}^{3}\sum_{n=-l}^{l}\sum_{k=1}^{15}\alpha_{klmn}e^{i\lambda_k\tau}\hat{T}_{ln}, \end{aligned} \tag{3.14}$$

where α_{klmn} is introduced to denote the coefficient. By the properties of Laplacian expansion (Liesen & Mehrmann, 2015),

$$\sum_k \alpha_{klmn} = \begin{cases} (-1)^m & \text{when } l = 2 \text{ and } n = m; \\ 0 & \text{otherwise.} \end{cases} \tag{3.15}$$

Substituting Eq. 3.14 into Eq. 3.9, we have

$$\hat{\hat{\Gamma}}(\hat{\rho}) = -\sum_{m=-2}^{2}\left[\hat{T}_{2m}, \left[\sum_{l,n}\sum_k \alpha_{klmn}J(m\omega_r + \lambda_k)\hat{T}_{ln}, \hat{\rho}\right]\right]. \tag{3.16}$$

The spectral density function can be approximated by observation that the eigenvalues are upper-bounded such that (Garren, 1968)

$$\lambda_k \leq 15\max\left(|d_{ij}|\right), \tag{3.17}$$

where d_{ij} are the elements of $\mathbf{D}$ dependent on ω_1, ω_Δ or ω_Q (red, yellow and green shaded entries in Fig.3.1). In biological MR experiments, λ_k ranges between $0 \sim 10^4$ Hz, much smaller than τ_c^{-1} (Rooney & Springer Jr, 1991; Shekar, Tang, & Jerschow, 2010), resulting in $\lambda_k\tau_c \ll 1$. In addition, $\omega_r \approx \omega_0$. We have $J(m\omega_r + \lambda_k) \approx J(m\omega_0)$

(also denoted as J_m). Hence,

$$\begin{aligned}\hat{\hat{\Gamma}}(\hat{\rho}) &\approx -\sum_{m=-2}^{2}\left[\hat{T}_{2m},\left[\sum_{l,n}\sum_{k}\alpha_{klmn}J_m\hat{T}_{ln},\hat{\rho}\right]\right] \\ &= -\sum_{m=-2}^{2}\left[\hat{T}_{2m},\left[\sum_{l,n}\sum_{k}\alpha_{klmn}\hat{T}_{ln},\hat{\rho}\right]\right]J_m \\ &= -\sum_{m=-2}^{2}\left[\hat{T}_{2m},\left[\hat{T}^{\dagger}_{2m},\hat{\rho}\right]\right]J_m.\end{aligned} \tag{3.18}$$

The double commutator in Eq. 3.18 now can be expanded using the commutation law (van der Maarel, 2003b). The resultant form of Eq. 3.18 implies that the relaxation rates are decoupled from the RF field, the off resonance and the anisotropy of the environment when the correlation time is sufficiently short.

3.2.3 The Offset Vector, C

At thermal equilibrium, $\hat{\rho}_0 = \mathbf{P}(0) = \hat{T}_{10}$, resulting in the offset vector of $\mathbf{C} = -\mathbf{R}\mathbf{P}(0)$,

$$\mathbf{C} = \left[\frac{2}{5}J_1 + \frac{8}{5}J_2, 0, 0, 0, 0, 0, 0, 0, \frac{4}{5}J_1 - \frac{4}{5}J_2, 0, 0, 0, 0, 0, 0\right]^{\top}. \tag{3.19}$$

3.2.4 The 'Adapted' Bloch Equation

The well-known BE describes the simultaneous effects of excitation, precession and relaxation as the dynamics of a magnetisation vector, written as

$$\frac{d}{dt}\begin{bmatrix} M_x \\ M_y \\ M_z \end{bmatrix} = \begin{bmatrix} -T_2^{-1} & -\omega_\Delta & \omega_1 \sin\phi_0 \\ \omega_\Delta & -T_2^{-1} & -\omega_1\cos\phi_0 \\ -\omega_1\sin\phi_0 & \omega_1\cos\phi_0 & -T_1^{-1} \end{bmatrix}\begin{bmatrix} M_x \\ M_y \\ M_z \end{bmatrix} + \begin{bmatrix} 0 \\ 0 \\ T_1^{-1} \end{bmatrix}, \tag{3.20}$$

where the net magnetisation $M_0 = 1$ is assumed.

The adapted BE for the spin-3/2 dynamics is the weighted linear combination of the short and long components,

$$\mathbf{M}(t) = 0.6\mathbf{M}_s(t) + 0.4\mathbf{M}_l(t), \tag{3.21}$$

where $\mathbf{M}_s$ and $\mathbf{M}_l$ is each a solution to BE with short and long T_2, respectively. The short and long transverse relaxation times, T_{2s} and T_{2l}, have the following relationship

with the spectral densities:

$$T_{2s} \approx \frac{1}{J_0 + J_1}, \quad T_{2l} = \frac{1}{J_1 + J_2} \quad when \quad \omega_Q < J_2, \tag{3.22a}$$

$$T_{2s} = \frac{1}{J_0 + J_1 + J_2}, \quad T_{2l} = \frac{1}{J_1 + J_2} \quad when \quad \omega_Q \geq J_2. \tag{3.22b}$$

3.3 Methods

Numerical integration was used to solve the SBE and BE in MATLAB (Mathworks, Natick, MA) using the Runge-Kutta method (ode45). The complete script is available at `https://github.com/MBCIU/Sodium_spin_dynamics_simulation`. SBE simulations were compared with the MATLAB-based spin-3/2 simulators of Kratzer et al. and Madelin, Lee, et al., as well as the adapted BE.

Three types of motion regimes mimicking biological environments were chosen with measured spectral density values taken from Wilferth et al (Wilferth et al., 2019):

1. **50 mM saline (isotropic, fast-motion regime):** $J_0 = J_1 = J_2 = 8.9$ Hz, $\omega_Q = 0$ Hz, $T_1 = T_{2s} = T_{2l} = 56.1$ ms;
2. **8% agar (isotropic, slow-motion regime):** $J_0 = 250$ Hz, $J_1 = 45.4$ Hz, $J_2 = 19.3$ Hz, $\omega_Q = 0$ Hz, $T_1 = 21.7$ ms, $T_{2s} = 3.4$ ms, $T_{2l} = 15.4$ ms;
3. **3% xanthan (anisotropic, slow-motion regime):** $J_0 = 319$ Hz, $J_1 = 28.2$ Hz, $J_2 = 28.1$ Hz, $\omega_Q = 61.8$ Hz, $T_1 = 17.3$ ms, $T_{2s} = 2.7$ ms, $T_{2l} = 17.8$ ms.

Pulse Duration Effect on Magnetisation Inversion

The quadrupolar relaxation effect is known to be significant in soft rectangular inversion pulses (R. Stobbe & Beaulieu, 2005). To compare the simulators in characterising the simultaneous effects of the spin-3/2 dynamics, rectangular inversion pulses with various durations were simulated, ranging from 0.5 ms to 20 ms.

Adiabatic Inversion Pulse

To examine the response of the ^{23}Na spin system to modulated pulses, the adiabatic Wide-band Uniform Rate and Smooth Truncation (WURST) inversion pulse sequence (Madelin et al., 2010) was simulated.

The amplitude of the pulse is modulated by

$$\omega_1(t) = 2\pi v_1 \left(1 - \left|\sin\left(\frac{\pi(2t - T_p)}{2T_p}\right)\right|^{20}\right), \tag{3.23}$$

where v_1 is the amplitude in Hz and the pulse duration T_p was chosen to be 10 ms. The frequency of the pulse is given by

$$\phi(t) = \frac{\pi \Delta f}{T_p} t^2, \tag{3.24}$$

where the frequency sweep range, Δf, was chosen to be 2 kHz.

While SBE's implementation uses ode45 for efficient computation of the simulation, other 3/2-spin simulators employ user-defined, linear-time steps during their calculations. To compare the accuracy and performance of the simulators, WURST simulations were run across a range of step sizes for the Madelin and Kratzer simulators, in order to compare accuracy and computational efficiency with the SBE approach.

Triple-Quantum Filtering

To examine multiple-quantum coherences, a six-step TQF experiment was simulated, following the three-pulse experiment setup in Hancu et al (Hancu et al., 1999), employing hard pulses of 500 μs. The first pulse was phase cycled through 30°, 90°, 150°, −150°, −90°, −30°. After the preparation time of 3 ms, the second pulse was applied with a phase offset of 90° with reference to the first pulse. The third pulse followed after a 400μs delay with 0° phase.

3.4 Results

Pulse Duration Effect on Magnetisation Inversion

The resultant longitudinal magnetisation evolutions during the 10-ms rectangular pulse are identical in saline, while the results from adapted BE deviate from the others in agar and, more manifestly, xanthan (Figure 3.2A). The differences between the spin-3/2 simulators and BE in the inverted longitudinal magnetisation amplitude are negligible when the pulse is short, but become more notable with increasing pulse length, except for saline in which there is no difference (Figure 3.2B). The results obtained by the spin-3/2 simulators are in agreement. Their output of time evolution trajectories under

the 10-ms rectangular pulse (Figure 3.2A) agree well with the literature (R. Stobbe & Beaulieu, 2005).

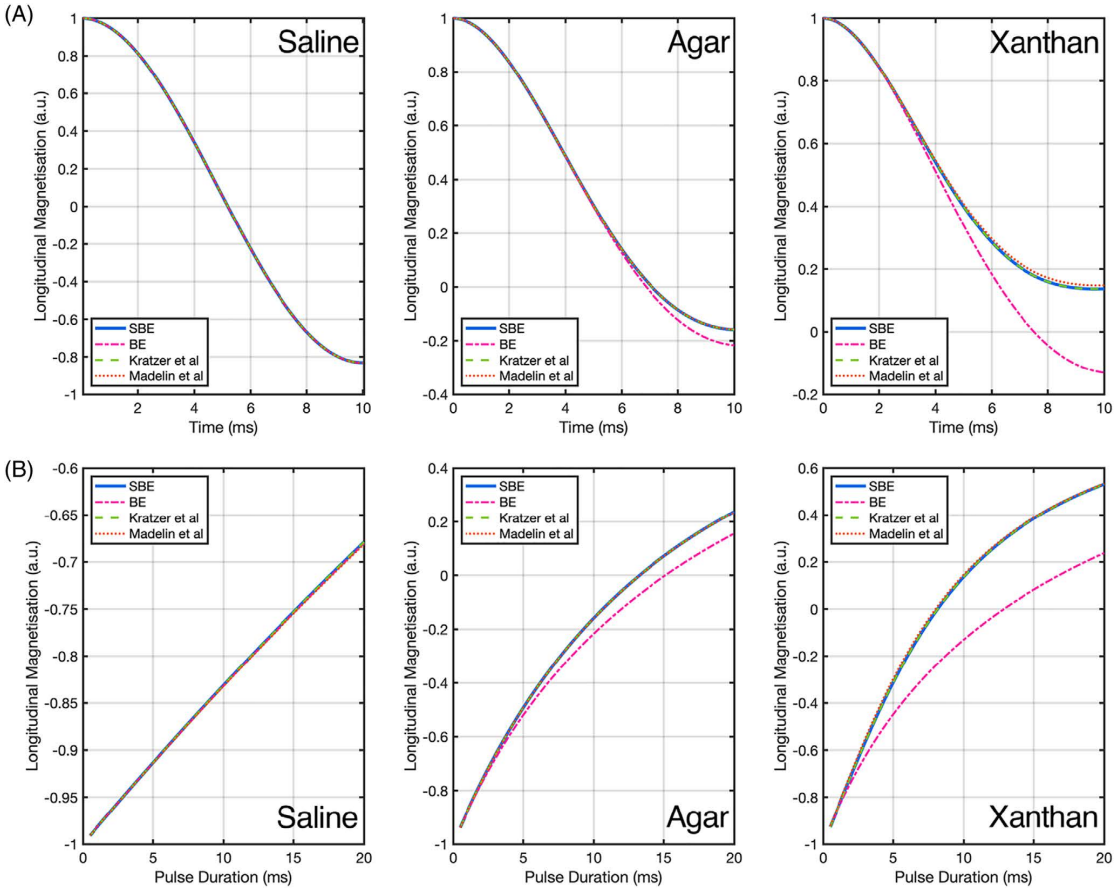

FIGURE 3.2: (A) The simulated time evolution of on-resonance ^{23}Na longitudinal magnetisation during a 10-ms rectangular pulse. (B) The dependence of longitudinal magnetisation on the rectangular pulse length. Kratzer and Madelin simulators were each run with 3000 time-steps.

Adiabatic Inversion Pulse

Simulations of magnetisation evolution during WURST inversion were compared. Again, the results are identical in saline. However, the differences between the spin-3/2 simulators and BE are less obvious in agar and xanthan (Figure 3.3A), compared to the results for the 10-ms soft pulse inversion in the previous simulation.

The results of the SBE, Madelin and Kratzer spin-3/2 simulators are in strong alignment with one another (Figure 3.3), when the number of time steps is large for the latter two simulators. Comparing the simulation results of simulators with linearly discretised time steps shows variations in the calculated magnetisation evolution, with more time steps, i.e. small step sizes, resulting in curves that approach SBE's output. Comparison of computational times of the spin-3/2 simulators (Table 3.1) highlights the computational

efficiency of SBE with its simulations being more than 10 times faster for simulations with high accuracy.

To demonstrate the capability of SBE, the inversion preparation stage of the WURST sequence was simulated with off-resonance frequencies ranging from -50 to 50 Hz (Figure 3.3C). The longitudinal magnetisation amplitude at the end of the inversion preparation stage is shown in Figure 3.3D. These results can be used to assess robustness against B_0 inhomogeneity and are in agreement with the literature (Madelin et al., 2010).

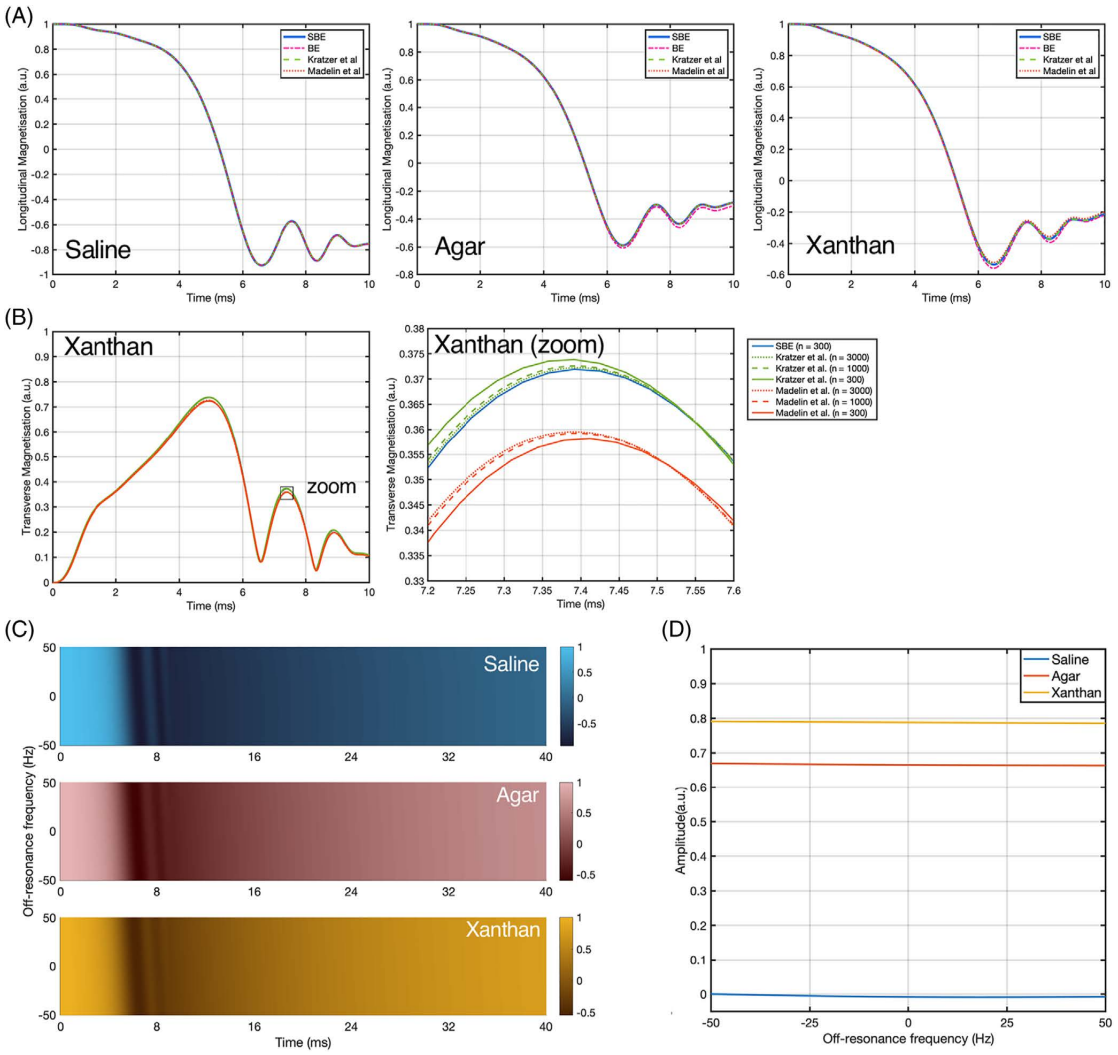

FIGURE 3.3: Simulated time evolution of on-resonance ^{23}Na (A) longitudinal magnetisation during the WURST IR pulse in saline, agar and xanthan, and (B) transverse magnetisation in xanthan. SBE simulation depicting (C) the amplitude of the longitudinal magnetisation during the inversion preparation stage of the WURST IR pulse with the influence of B_0 inhomogeneity, and (D) amplitude values at the end of the stage.

TABLE 3.1: Simulation run times of ^{23}Na in xanthan during WURST IR pulse.

Simulator	**Solver**	**Number of steps**	**Run time (ms)**[a]
SBE	ode45	300[b]	50±11
Kratzer et al (2021)	Eigen-decomposition method with linearly discretised time steps	3000	678±28
		1000	237±30
		300	71±10
Madelin et al (2014)	Consecutive operations (ω_1, ω_Q, ω_Δ, relaxation) with linearly discretised time steps	3000	1277±62
		1000	421±26
		300	133±25

[a] The measurements were repeated 100 times
[b] Note that the user-defined number of steps in the call to ode45 does not determine the step size chosen internally within the integration routine. The algorithm returns output that is interpolated to the user-defined number of steps.

Triple-quantum Filtering

TQF experiments constitute a significant aspect of spin-3/2 simulation and are the basis of TQF experiment design and signal analysis. As has been previously shown by Hancu et al (Hancu et al., 2000) and Tsang et al (Tsang et al., 2012) for an ISTO framework, we demonstrate the ability of SBE to provide the time evolution of the tensor components (Figure 3.4 and Figure 3.5A). The filtered outcome, which is the sum of the phase cycling steps with proper polarity toggling, clearly exhibits the rise of the observable signal (the rank-1 order-1 component) transferred from the rank-3 order-3 component as shown in Figure 3.5B.

3.5 Discussion

Based on the ISTO formalism for convenient description of spin-3/2 dynamics, we have shown that the Redfield equation can be simplified under the condition that the correlation time is sufficiently short, which is satisfied for ^{23}Na in biological tissue. This theoretical result implies that the RF field, the off resonance and the anisotropy of the biological tissue have a vanishing effect on the relaxation rates. This leads to a generalised description of the ^{23}Na spin system; the SBE captures the combined effect of the residual Zeeman field, the RF field, and the static and fluctuating components of EFG. Noticeably, incorporating relaxation under an off-resonance RF facilitates simulation of experiments such as spin locking, adiabatic RF irradiation and slice selective excitation. Although we restrict the discussion to ^{23}Na nuclei in this paper, the formalism is extendable to other spin-3/2 nuclei as long as the correlation time condition is satisfied.

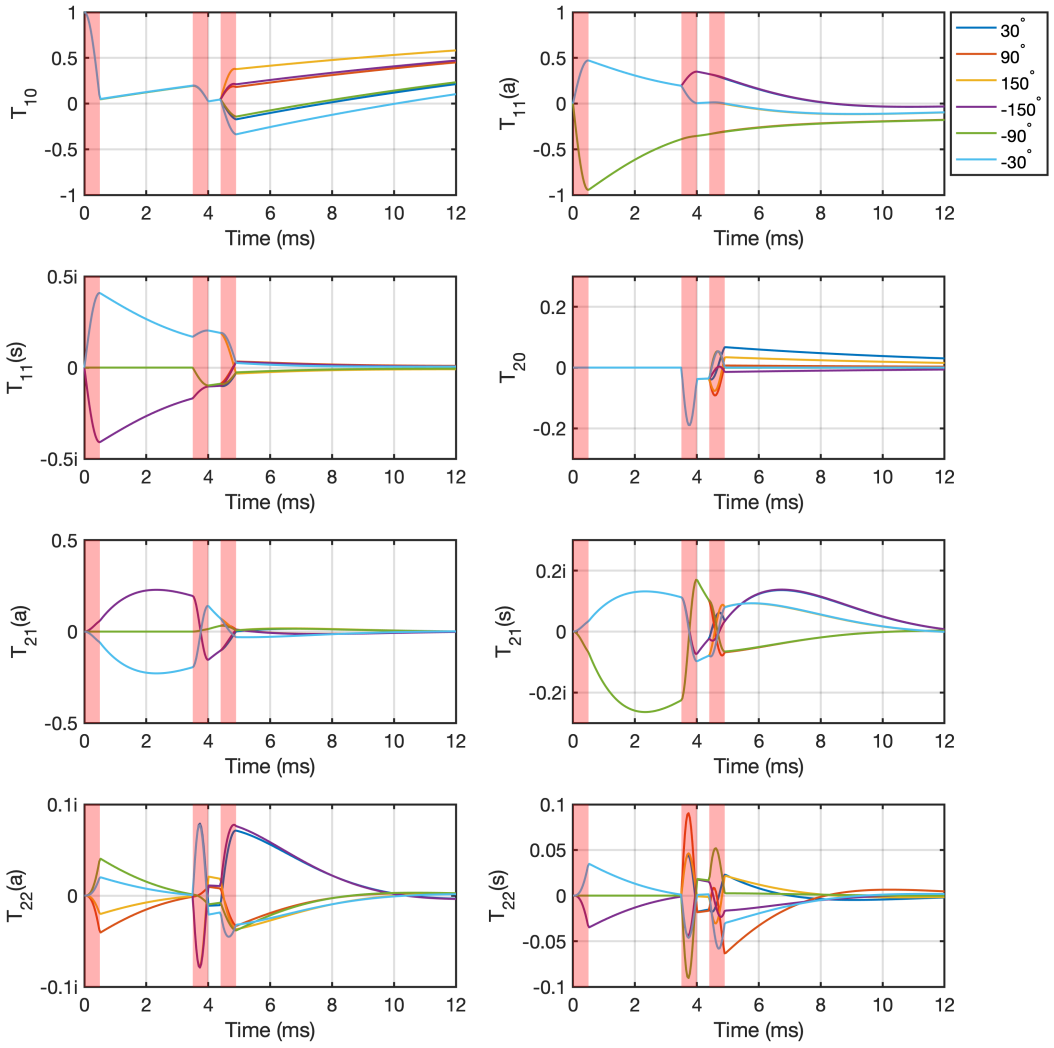

FIGURE 3.4: Evolution of the rank-1 and rank-2 components in each phase cycle of the three-pulse TQF experiments. Red bars indicate periods of RF excitation.

The SBE system matrix, **L**, is a structured, intuitive and accessible representation of sodium dynamics for the MRI research community that will enable advances in ^{23}Na pulse and pulse sequence design. It obviates the need for a piecewise treatment to analyse ^{23}Na sequences, with simulation rendered trivial; SBE simulation requires only the specification of the environment parameters, the pulse and gradient functions. The ability to simulate the spin-3/2 dynamics with a single call to a numerical integration routine results in considerably higher computation efficiency for SBE compared to the Madelin and Kratzer simulators; numerical integration routines of packages such as MATLAB have been developed over decades to dynamically adjust simulation step-sizes according to time-varying inputs. Thus the simulation of spin-3/2 dynamics with

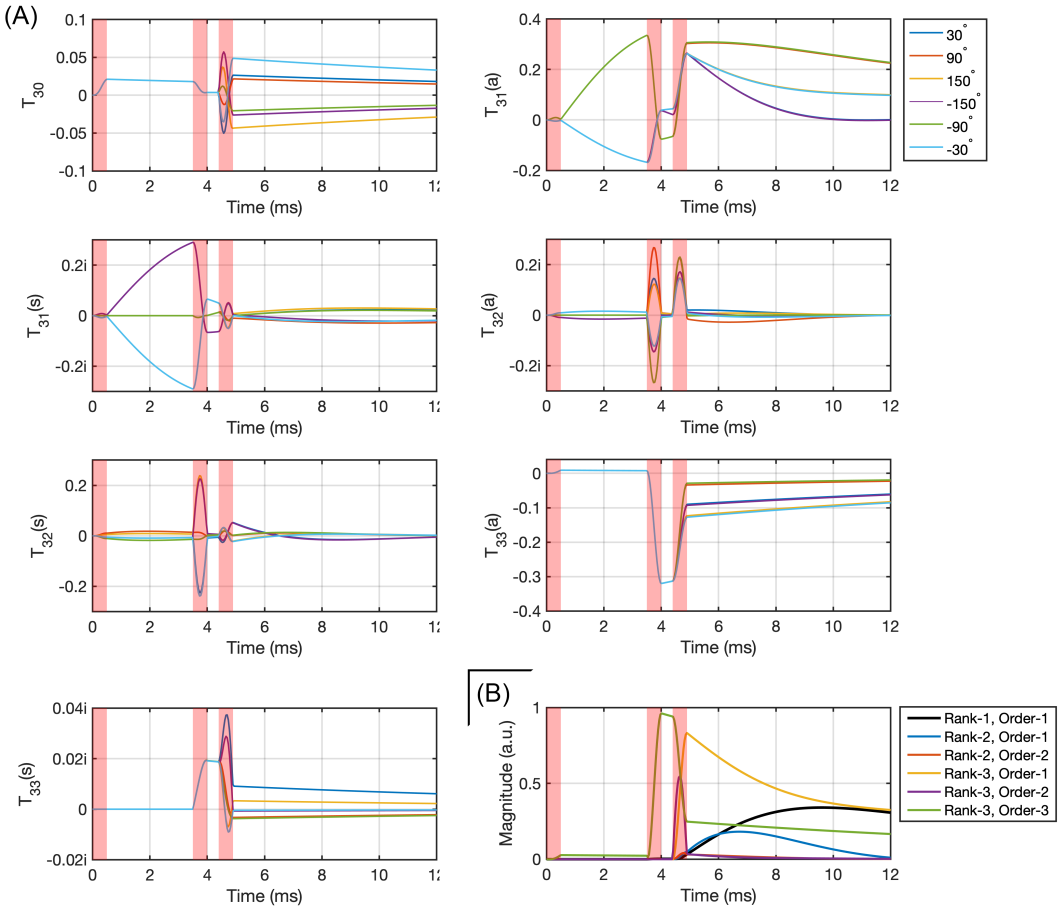

FIGURE 3.5: (A) Evolution of the rank-3 components in each phase cycle of the three-pulse TQF experiments. (B) The summed coherences of the phase cycling steps. Red bars indicate periods of RF excitation.

time-varying RF or gradients is best approached using the SBE formalism.

The behaviour of the SBE has been demonstrated through simulations, including the expected negligible difference between SBE and BE for fluid regions. However, for biological tissue environments, the deviations between spin-3/2 and spin-1/2 dynamics are more pronounced and depend on the specifics of the pulse sequence, necessitating a functional form for the spin system that elucidates meaning. For applications requiring accurate predictions, such as ^{23}Na-MRF, the SBE will be a crucial tool. Indeed, the recent results of Kratzer et al (Kratzer et al., 2021) confirm the performance gain from using the ISTO-based simulation of (Hancu et al., 2000), compared with their previous proof-of-concept study (Kratzer et al., 2020) using BE-based simulation. With the full description of the ^{23}Na spin dynamics, the SBE can be used for the biological environments in which the residual quadrupolar frequency is large, such as cartilage.

3.6 Conclusion

The ‘Spin-3/2 Bloch Equation’ has been formulated as a generalised representation of spin-3/2 dynamics in biological tissue environments, encapsulating excitation, relaxation and off-resonance effects for an intuitive, structured system representation that facilitates accurate and computationally efficient simulation for pulse sequence design.

Chapter 4

Triple-pulse ^{23}Na MRI Sequence (TriNa) for Simultaneous Acquisition of Spin-density-weighted and Fluid-attenuated Images

4.1 Introduction

Total sodium concentration (TSC) and, particularly, intracellular sodium concentration (ISC) are key biomarkers of cell physiology. Changes of ISC in a lesion might be related to the malfunction of Na^+-K^+ ATPase, while changes of TSC include those caused by increased extracellular volume or vascularisation (Madelin & Regatte, 2013). Both TSC and ISC are interesting imaging targets in ^{23}Na MRI. A spin density-weighted (SDW) sequence for TSC measurement typically consists of a short excitation pulse, a centre-out, an ultra-short TE (UTE) readout and a sufficiently long TR for the recovery to the thermal equilibrium (Ouwerkerk et al., 2008; Konstandin & Nagel, 2014). ^{23}Na FLAIR sequences are weighted towards ISC. One of the FLAIR variant sequences, soft inversion recovery fluid attenuation (SIRFLA) (R. Stobbe & Beaulieu, 2005), uses an elongated inversion pulse to reduce specific absorption rate (SAR) and enhance tissue-fluid contrast during the inversion for SNR efficiency. However, the narrow-bandwidth inversion pulse results in incomplete fluid suppression where the B_0 field is inhomogeneous (R. Stobbe & Beaulieu, 2005). In contrast, a hard pulse inversion recovery (HIR) uses a short inversion pulse by necessity, resulting in high SAR and, consequently, a long TR (Mennecke et al., 2021).

It has been shown that research can gain valuable insights on the in-vivo sodium by acquiring both SDW and FLAIR ^{23}Na images. For example, this combination can be used to quantify intracellular sodium concentrations and extracellular volume fractions the brain tissue (Madelin, Kline, Walvick, & Regatte, 2014), which might be effective in detecting pathologies in the brain. In brain tumour study, the dual contrast has been used to characterise grades and genotypes (Nagel et al., 2011; Nunes Neto et al., 2018). In multiple sclerosis lesions, concurrent changes of SDW and FLAIR signals have been found correlated to the disease progression (Biller et al., 2016; Mennecke et al., 2021; R. Stobbe et al., 2021). Although the clinical potentials of this sequence combination have been demonstrated in the literature, two obstacles hinder their practical use: one is the time consumption to acquire the two images, and the other is the limitation of the FLAIR sequences: HIR is SNR-inefficient whereas SIRFLA is sensitive to B_0 inhomogeneity. Thus, a design for higher efficiency and quality is pertinent.

In this work, a novel sequence, Triple-pulse ^{23}Na (TriNa) MRI sequence was proposed for the simultaneous acquisition of spin density-weighted (TriNa-SD) and fluid-suppressed (TriNa-FS) signals. It was shown that TriNa can achieve higher efficiency compared to the standalone sequences. Furthermore, the B_0 inhomogeneity robustness for TriNa-FS was strengthened by a proposed post-acquisition correction method, which suppresses the off-resonance artifacts using the acquired TriNa-SD and an additional B_0 map.

4.2 Methods

4.2.1 Sequence Design

The TriNa sequence consists of three non-selective, in-phase, 90° rectangular pulses (Figure 4.1). The first and the second pulses are separated by a delay τ, during which the TriNa-SD readout gradient and a subsequent rewinding gradient take place. This delay also benefits FLAIR contrast generation by introducing transverse relaxation, allowing ^{23}Na spins in different environments to decay differentially. The second readout gradient, to acquire the TriNa-FS signal, is applied after the third pulse. Both readouts use the 3D radial inside-out scheme with the spoke directions determined by Saff and Kuijlaars' algorithm (Saff & Kuijlaars, 1997).

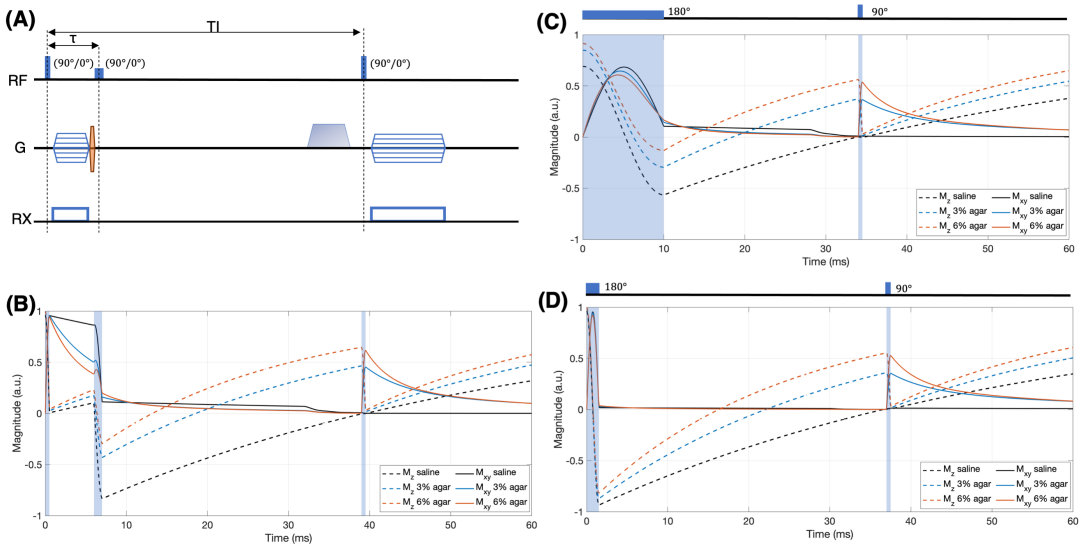

FIGURE 4.1: (A) TriNa diagram. The sequence consists of three in-phase 90° rectangular pulses. The first readout gradient is followed by a rewinding gradient. A spoiler gradient is applied prior to the third pulse to destroy any residual transverse magnetisation. Simulated magnetisation evolution of (B) TriNa, (C) SIRFLA and (D) HIR.

4.2.2 Simulation

To verify the design of TriNa, the sequence was simulated using Spin-3/2 Bloch Equation Simulator (Wu, Blunck, & Johnston, 2022) in MATLAB (Mathworks, Natick, MA, USA). Three environments were simulated with their spectral densities taken from the literature: (R. W. Stobbe & Beaulieu, 2014) (1) saline: $J_0 = J_2 = J_3 = 9.4$ Hz; (2) 3% agar: $J_0/J_1/J_2 = 190/21/14$ Hz; (3) 6% agar: $J_0/J_1/J_2 = 300/21/18$ Hz. The agar and saline are isotropic environments and therefore it is assumed that the residual quadrupolar frequency $\omega_Q = 0$.

For the simulation of the time evolution, the B_0 field is assumed to be Lorentzian-distributed with the reversible relaxation rate R_2' of 1 Hz. The magnetisation was integrated from 11 isochromats, equidistantly distributed between $-2R_2'$ and $2R_2'$, and weighted by the corresponding probability density function. The sequence was simulated with pulse lengths TP = 0.5/1/0.5 ms and TR = 210 ms. For the simulation with B_0 inhomogeneity, the simulations were repeated with the off-resonance frequency ω stepping through -80 to 80 Hz. TriNa simulations were compared to both SAR-matched SIRFLA (TP = 10/0.5 ms, TR = 100 ms) and SAR-matched HIR (TP = 1.5/0.5 ms, TR = 210 ms) simulations.

4.2.3 Experimental Data

^{23}Na MR images were acquired on a research 7T MRI scanner (Siemens Healthineers, Erlangen, Germany) with a dual-tuned ^{1}H-^{23}Na transmit/receive head coil (QED, Mayfield Village, OH, USA). Prior to acquisitions, shimming was performed using the vendor-provided routine on the ^{1}H signal.

Phantom

A cylindrical phantom consisting of five vials with various sodium concentrations and agar concentrations submerged in saline was imaged (Figure 4.2A). TriNa, SIRFLA and HIR were compared in two scenarios. The first scenario compared these three sequences with the acquisition time matched (10.5 mins). The second scenario matched the TriNa TA to the time required to acquire both standalone SDW and FLAIR sequences. With TR of 100 ms, SDW can acquire 3000 spokes in 5 minutes. Hence, the radial spokes in SIRFLA and HIR data were retrospectively subsampled by a factor of 2 (TA = 5.25 mins). The sequence parameters are listed in Table 4.1. Raw k-space data were conditioned by a Hanning filter to reduce Gibbs rings and noise. Image reconstruction was performed by non-uniform fast Fourier Transform provided in the Michigan Image Reconstruction Toolbox (Ann Arbor, MI, USA). All ^{23}Na images were normalised by their number of acquisition spokes.

In addition, a double-echo 3D-MERINA (Blunck et al., 2018) (TE = 0.4/8.4 ms) was implemented to measure the B_0 field. The phase images were unwrapped by PRELUDE (FSL, FMRIB, Oxford, UK).

	FA(°)	TP (ms)	TE (ms)	TR (ms)	TI (ms)	T_{RO} (ms)	resolution (mm)	Matrix	N_{proj}	TA (min)
TriNa	90/90/90	0.5/1/0.5	0.4/0.4	210	42	4/6	3.1/3.1 isotropic	64/64	3000	10.5
SIRFLA	180/90	10/0.5	0.4	97	30	6	3.1 isotropic	64	6500	10.5
HIR	180/90	1.5/0.5	0.4	210	39	6	3.1 isotropic	64	3000	10.5
SIRFLA	180/90	10/0.5	0.4	97	30	6	3.1 isotropic	64	3250	5.25
HIR	180/90	1.5/0.5	0.4	210	39	6	3.1 isotropic	64	1500	5.25

TABLE 4.1: ^{23}Na MRI sequence parameters for phantom experiments.

For SNR analysis, a region of interest was selected in the centre of the phantom. The SNR was calculated with correction for Rician noise (Gudbjartsson & Patz, 1995).

In Vivo

The *in-vivo* brain imaging was approved by the University of Melbourne Human Research Ethics Committee. Two volunteers (female, 23-year-old) were scanned with consent. For ^{23}Na, TriNa, SIRFLA and HIR were acquired, with the parameters in Table 4.2. B_0 field measurement was carried out by the vendor-provided GRE mapping sequence on the ^{1}H channel. In addition, ^{1}H MP2RAGE for anatomical reference was acquired using a 32-channel head coil (Nova Medical Inc., Wilmington, MA, USA) on the same scanner.

	FA(°)	TP (ms)	TE (ms)	TR (ms)	TI (ms)	T_{RO} (ms)	resolution (mm)	Matrix	N_{proj}	TA (min)
TriNa	90/90/90	0.5/1/0.5	0.4/0.4	210	42	4/6	3.1/3.8 isotropic	64/52	6000	21
SIRFLA	180/90	10/0.5	0.4	97	25	6	3.8 isotropic	52	13000	21
HIR	180/90	1.5/0.5	0.4	210	39	6	3.8 isotropic	52	6000	21

TABLE 4.2: ^{23}Na MRI sequence parameters for *in-vivo* experiments.

4.2.4 B_0 Inhomogeneity Artifact Correction for the Brain

TriNa-FS and SIRFLA are sensitive to B_0 inhomogeneity, as off-resonance reduces the depth of the inversion and results in hyper-intensity in the fluid-suppressed images. Here, a correction method for TriNa-FS is proposed. To discriminate environments where ^{23}Na spins exhibit different relaxation, the brain voxel is modelled as comprising intracellular (denoted by subscript "ic") and extracellular (subscript "ec") and fluid compartments (subscript "f"), similar to the one by Gilles et al. (2017). The longitudinal (superscript "(z)") and transverse (superscript "(xy)") bi-exponential relaxation functions are modelled as (van der Maarel, 2003b)

$$f^{(z)}(t) = \frac{1}{5}e^{-t/T_{1,s}} + \frac{4}{5}e^{-t/T_{1,l}}, \tag{4.1}$$

$$f^{(xy)}(t) = \frac{3}{5}e^{-t/T_{2,s}} + \frac{2}{5}e^{-t/T_{2,l}}, \tag{4.2}$$

where subscripts "s" and "l" denote short and long time constants, respectively. For the fluid compartment, $T_{1,s} = T_{1,l}$ and $T_{2,s} = T_{2,l}$ and the relaxation functions become mono-exponential.

For TriNa-FS, there are three relaxation weights that characterise the signal: the transverse relaxation during the first and the second pulses $f^{(xy)}(\tau)$, the longitudinal relaxation between the second and the third pulses $f^{(z)}(TI-\tau)$ and the transverse relaxation between the third pulse and the start of TriNa-FS acquisition $f^{(xy)}(TE)$. For brevity, let $a = f^{(xy)}(\tau), b = f^{(z)}(TI-\tau)$ and $c = f^{(xy)}(TE)$ in the following equations.

According to ^{23}Na NMR dynamics, the contribution to TriNa-FS intensity I^{FS} from a compartment i in a voxel is dependent on a coefficient k that converts magnetisation to voxel intensity, the ^{23}Na nuclei quantity m_i, the hard pulse flip angle θ, the off-resonance frequency ω and the relaxation weights, given as

$$I_i^{FS} = k\left|m_i c_i \sin\theta\left(1 - b_i\left(1 + a_i \sin^2\theta\cos\omega\tau\right)\right)\right| \quad i \in \{ic, ec, f\}\,. \tag{4.3}$$

With ideal $\theta = 90°$ and $\omega = 0°$, I_f^{FS} will be nulled, that is, $I_f^{FS} = k|m_f c_f\left(1 - b_f\left(1 + a_f\right)\right)| = 0$. However, a residual term typically exists in addition to the desired value in practice and the voxel intensity is

$$I^{FS} = k\left|\underbrace{\sum_{i\in\{ic,ec,f\}} m_i a_i b_i c_i \sin^3\theta\,(1-\cos\omega\tau)}_{\text{residual}} + \underbrace{\sum_{i\in\{ic,ec\}} m_i c_i \sin\theta\left(1 - b_i\left(1 + a_i\sin^2\theta\right)\right)}_{\text{desired}}\right|. \tag{4.4}$$

Likewise, the TriNa-SD intensity can be modeled as

$$I^{SD} = k\left|\sum_{i\in\{ic,ec,f\}} m_i c_i \sin\theta\right|. \tag{4.5}$$

To correct the residual term, assume that (i) the intracellular environment occupies around 80% volume with a sodium concentration of 10 mM in the brain tissue; (ii) the extracellular environment constitutes approximately 20% volume with a concentration of 150 mM; (iii) the fluid volume fraction is negligible in tissue and near 100% in CSF (K. Thulborn et al., 2016; Gilles et al., 2017). In this case, the extracellular compartment is the predominant source of the ^{23}Na spins and that $I^{SD} \gg I^{FS}_{\text{desired}}$ due to significantly weaker relaxation weighting. Equation 4.4 can be approximated by

$$I^{FS} \approx \left|\alpha I^{SD}\left(1 - \cos\left(\omega\tau\right)\right) + \beta\right|, \tag{4.6}$$

with model parameter α and β.

Estimates of α and β, $\hat{\alpha}$ and $\hat{\beta}$, can be obtained by a volume-wise nonlinear least squares fitting routine using the TriNa voxel vectors, $\mathbf{I}^{\mathbf{SD}}$ and $\mathbf{I}^{\mathbf{FS}}$, and an additional off-resonance map, $\mathbf{\Omega}$. The corrected intensity, $\tilde{\mathbf{I}}^{\mathbf{FS}}$, can be computed as

$$\tilde{\mathbf{I}}^{\mathbf{FS}} = \left|\mathbf{I}^{\mathbf{FS}} - \hat{\alpha}\mathbf{I}^{\mathbf{SD}}\left(1 - \cos \mathbf{\Omega}\tau\right)\right|. \tag{4.7}$$

Using the phantom experiment data, a bulk saline volume in the phantom was selected as the region of interest (ROI) to validate the correction method. For the *in-vivo* data, the correction method was applied to the entire brain region, with $\mathbf{\Omega}$ from the ^{1}H GRE converted to the ^{23}Na frequency and registered to $\mathbf{I}^{\mathbf{SD}}$ using the FSL Toolbox.

4.3 Results

The simulated magnetisation evolution for TriNa in three environments shows smooth decay during readout periods (Figure 4.2B). TriNa-FS has 24% (in 3% agar) and 15% (in 6% agar) higher peak intensities than SIRFLA (Figure 4.1C) and 29% (in 3% agar) and 17% (in 6% agar) higher peak than HIR (Figure 4.1D).

The TriNa-SD image clearly delineates the phantom boundaries and produces contrast associated with the ^{23}Na concentration (Figure 4.2B). In the FLAIR images, voxels from saline and 1% agar were strongly suppressed (Figure 4.2C-G). The FLAIR images visual qualities are in agreement with the corresponding measured SNR (Figure 4.2H). In the first scenario, the SNR values of TriNa-FS are 7-25% lower compared to SIRFLA (Figure 4.2D) but 8-12% higher compared to HIR (Figure 4.2F) in the 3% agar and 6% agar vial regions. In the second scenario, the SNR values in TriNa-FS are 6-29% higher than SIRFLA (Figure 4.2E) and 49-59% higher than HIR (Figure 4.2G).

As shown by the phantom data, TriNa-FS and SIRFLA are more sensitive to off resonances (Figure 4.3A-B and Figure 4.4A-B) whereas the HIR is robust (Figure 4.3C and Figure 4.4D). The phantom experiment results agree well with the simulation (Figure 4.3D). The model for correction illustrated in Figure 4.3A shows a good fit to the data.

The correction markedly reduced the fluid residual in TriNa-FS to the noise level (Figure 4.4A and Figure 4.4C), using the information provided in TriNa-SD and the B_0 map (Figure 4.4E-F). With correction, the fluid suppression is comparable between TriNa-FS (Figure 4.4C) and HIR (Figure 4.4D).

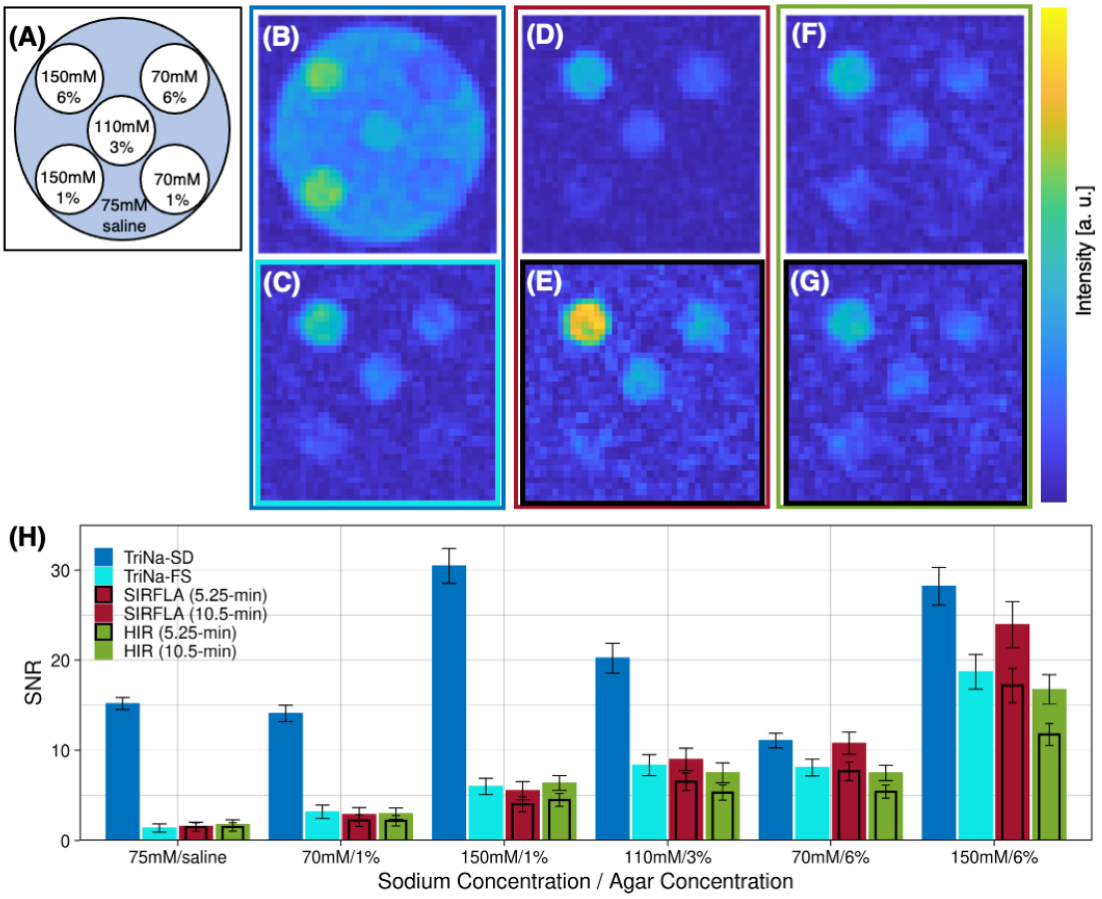

FIGURE 4.2: (A) The phantom schematic shows sodium concentration in mM and agar concentration in percentage. (B) Phantom TriNa-SD image and (C) TriNa-FS image were simultaneously acquired by TriNa in 10.5 minutes. (D) The SIRFLA image that was reconstructed from the data acquired in 10.5 minutes (the first scenario) and (E) from the data acquired in 5.25 minutes (the second scenario). (F) The HIR image reconstructed from the data acquired in 10.5 minutes and (G) in 5.25 minutes. Panels B-G are not displayed in the same colour window and some background voxels were cropped. (H) SNR analysis for the phantom experiment data.

The fitting model shows a good agreement with the *in-vivo* data (Figure 4.5A). With the parameters estimated by the model, most of the B_0 inhomogeneity-induced variation was rectified (Figure 4.5B). The correction can also be confirmed by the brain images. The artifacts located at the base of the frontal lobe and the front of the pons were mitigated (Figure 4.6A-B), making the corrected TriNa-FS more comparable to the B_0 inhomogeneity-insensitive HIR (Figure 4.6C). The correction was selectively applied to the regions with off resonance (Figure 4.6D-F).

The ^{23}Na images and the ^{1}H MP2RAGE from Volunteer II were compared (Figure 4.7). TriNa-SD demonstrates sufficient CNR to distinguish fluid and tissue voxels. In the parietal lobe of the FLAIR images, the highest SNR was achieved by SIRFLA, followed by TriNa-FS, matching the phantom study results. Bright artifacts appear in the base of the frontal lobe in the SIRLFA image (Figure 4.7D), where the B_0 field is distorted by

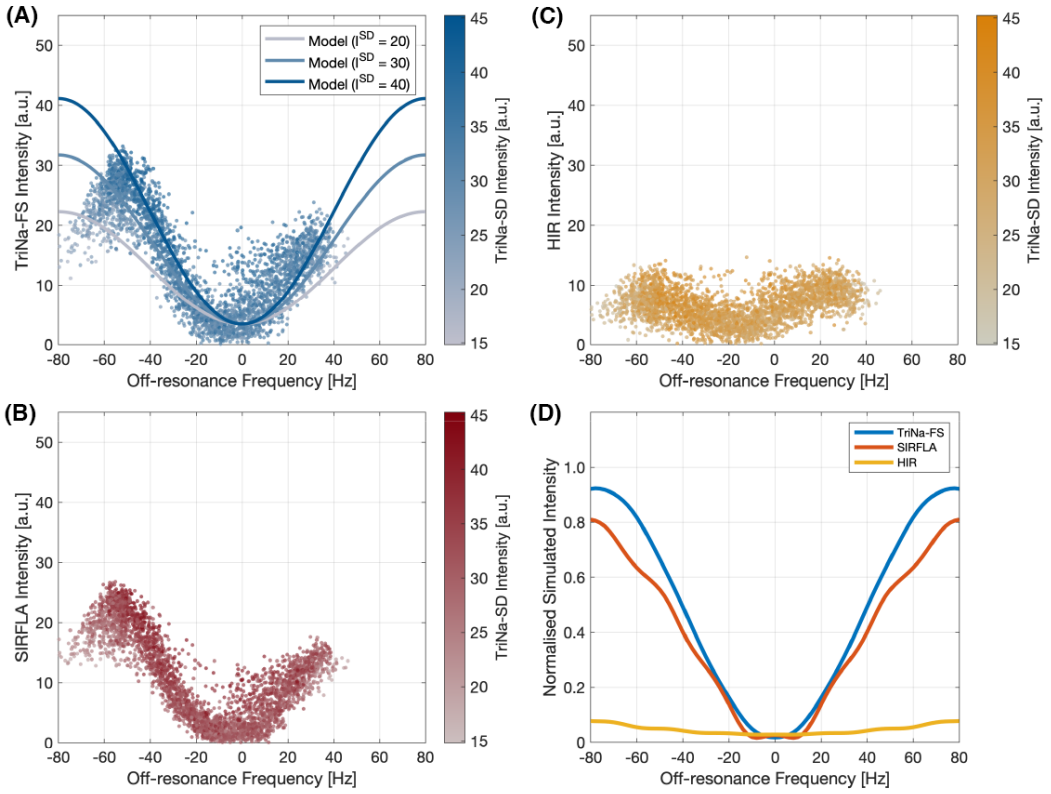

FIGURE 4.3: Scatter plots of phantom saline ROI intensity in (A) TriNa-FS, (B) SIRFLA and (C) HIR, in which the off resonance are plotted against the x-axes and the TriNa-SD intensities are represented by colour. In addition, the fitted model is illustrated by curves for TriNa-FS. (D) Simulated saline intensities under the off-resonance effect.

the nearby sinus air cavities. These artifacts are less obvious in the corrected TriNa-FS (Figure 4.7C) while they are not apparent in HIR (Figure 4.7E).

4.4 Discussion

The generation of FLAIR signal with three in-phase pulses is similar to Wong, Liu, Luh, Frank, and Buxton (2001). For ^{1}H MRI, except that TriNa does not contain a 180° refocusing pulse in between the first two pulses. The fast relaxation of the ^{23}Na spin makes it unnecessary, as a short τ of several milliseconds can greatly enhance tissue-fluid differentiation. Despite the absence of the refocusing pulse, there is no noticeable stimulated echo (STE) induced in TriNa, because the timings of the pulses, the low gyromagnetic ratio and the fast relaxation of ^{23}Na impede the development of the STE. The choice to not use the refocusing pulse reduces SAR and spares sequence vacancy for the TriNa-SD readout.

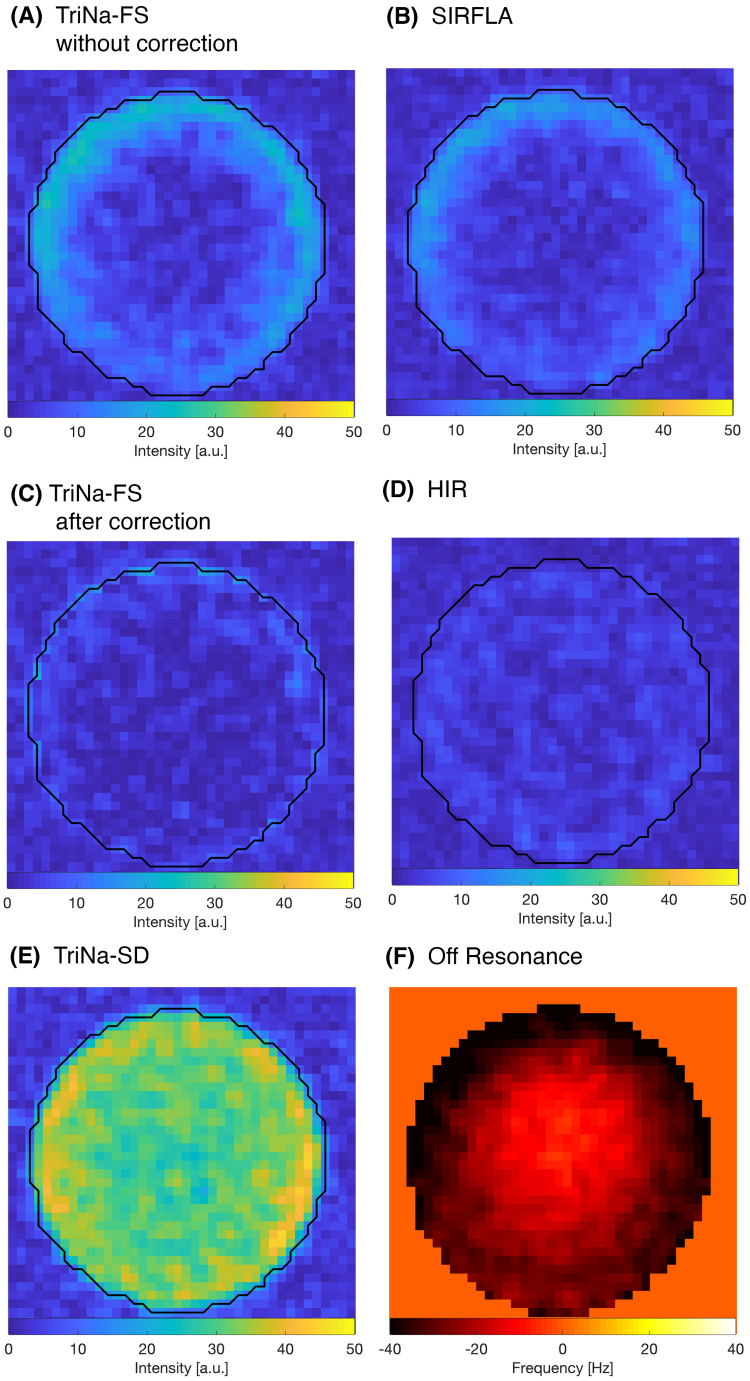

FIGURE 4.4: (A) TriNa-FS without correction shows hyper-intense saline induced by the B_0 inhomogeneity. The black line indicates the boundary of the ROI. (B) The corresponding SIRFLA image also exhibits B_0 inhomogeneity artifacts. (C) The correction has successfully suppressed the artifact, making the contrast similar to (D) the HIR image. (E) TriNa-SD and (F) a B_0 map acquired by MERINA were used in the correction.

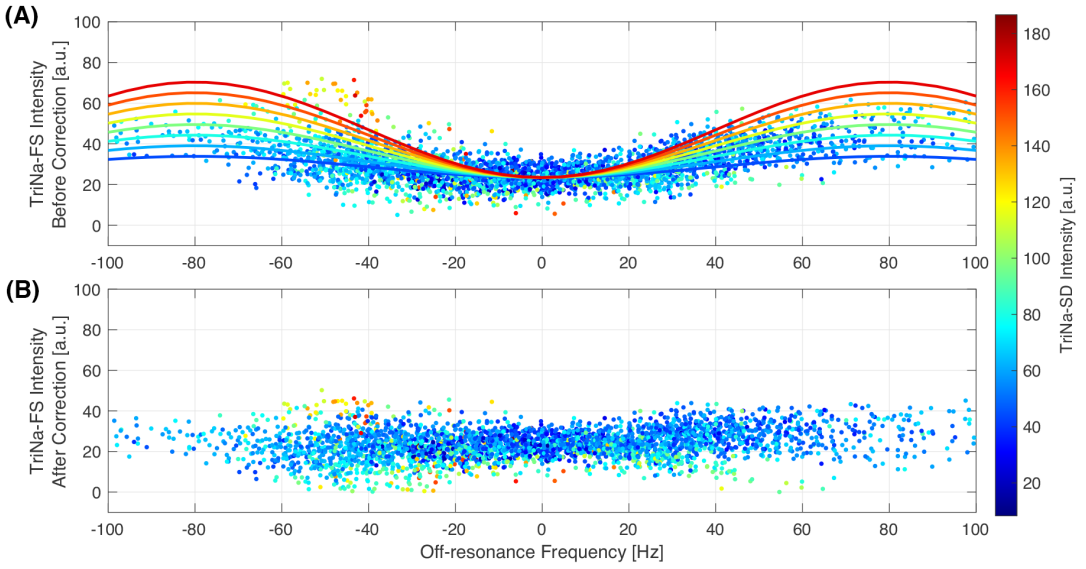

FIGURE 4.5: Scatter plots of TriNa-FS intensity against off-resonance frequency (A) before correction and (B) after correction. The fitted model is represented by curves. TriNa-SD intensity $\mathbf{I}^{\mathbf{SD}}$ is shown in colours ranging from 38 a.u. (blue) to 171 a.u. (red), with a step of 19 a.u.. A randomly selected subset of scatter points is used as the representation in the middle-frequency range for improved visualisation.

Although informative dual-contrast ^{23}Na MRI is favourable in clinical research, practical scan times have limited SNR and spatial resolution. TriNa alleviates this bottleneck with improved efficiency by simultaneous acquisition. As suggested by the phantom experiment, the SNR improvement to the FLAIR image can be as high as 59% (when compared to HIR). In the brain imaging experiments of this work, TriNa has demonstrated its higher efficiency compared to the standalone sequences, acquiring a nominal 3.1-mm isotropic SDW image and a 3.8-mm isotropic FLAIR image in 21 minutes. The SNR can be further improved by optimising the sampling density (Nagel et al., 2009; R. Stobbe & Beaulieu, 2008a).

In the human brain, ^{23}Na in fluid makes the major contribution to the total spin density in a voxel where there is CSF or vasculature (Madelin & Regatte, 2013). Therefore, incomplete fluid suppression caused by B_0 inhomogeneity could artifactually increase the voxel intensity by a significant amount. When this is a concern, HIR is preferred in spite of the low efficiency (Mennecke et al., 2021). For SIRFLA, the B_0 inhomogeneity robustness is related to the inversion pulse length and a trade-off for SNR (Feldman et al., 2013; Wilferth et al., 2019). Hence, SIRFLA's advantage is best shown where the B_0 field is adequately shimmed. This is similar to the raw TriNa-FS. The artifacts could be reduced by shortening τ or the duration of the second pulse, with the cost of SNR. Nevertheless, the raw TriNa-FS can be corrected with the self-provided TriNa-SD and an additional B_0 map, which adds only a couple of minutes when measured in the

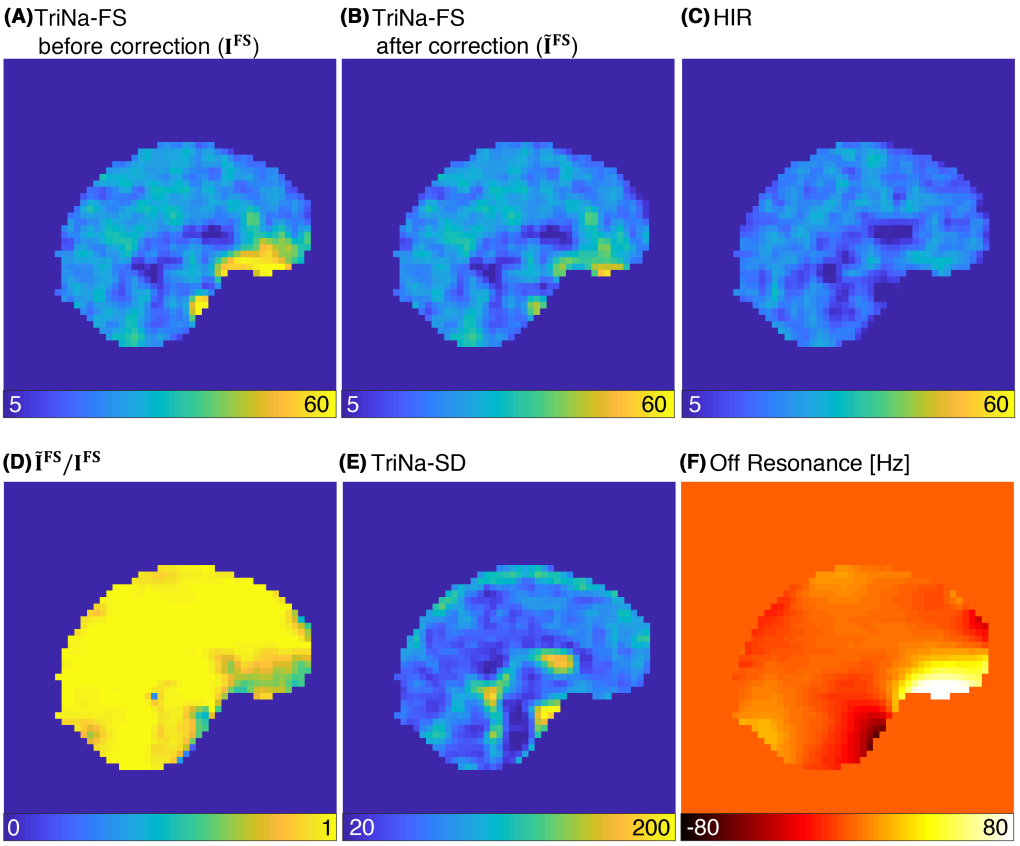

FIGURE 4.6: (A) A brain sagittal slice of TriNa-FS before correction. Artifacts are clearly shown in the base of the frontal lobe. (B) Most of these artifacts were removed after the correction. (C) The HIR image is not affected by B_0 inhomogeneity. (D) The ratio of $\tilde{\mathbf{I}}^{FS}$ to $\mathbf{I}^{FS}$ indicates that the correction only attenuates the hyper-intense regions and some part of the CSF regions, as referenced in (E) the TriNa-SD and (F) the B_0 map. Colours represent voxel intensities in (A-E) and frequency in (F).

^{1}H channel. A linear model is able to produce satisfactory voxelwise correction, mainly because the tissue voxels are the majority in the brain and the true contrast variation is much lower than the artifactual hyperintensity. The flip angle effect is simplified and implicit in the proposed model. For improved correction accuracy, one could refine the model and acquire a B_1 map at the expense of extra scan time. Nevertheless, B_1 inhomogeneity is not a major concern due to the relatively long RF wavelength in 7T ^{23}Na MRI. SIRFLA may be corrected by a similar method but the model may be more complicated, as the RF field and the residual B_0 field are coupled during the inversion. To the best of our knowledge, there is no published correction method for SIRFLA.

4.5 Conclusion

In this work, the novel TriNa sequence that simultaneous acquires ^{23}Na SDW and FLAIR images has been proposed. This design can acquire the images with improved SNR

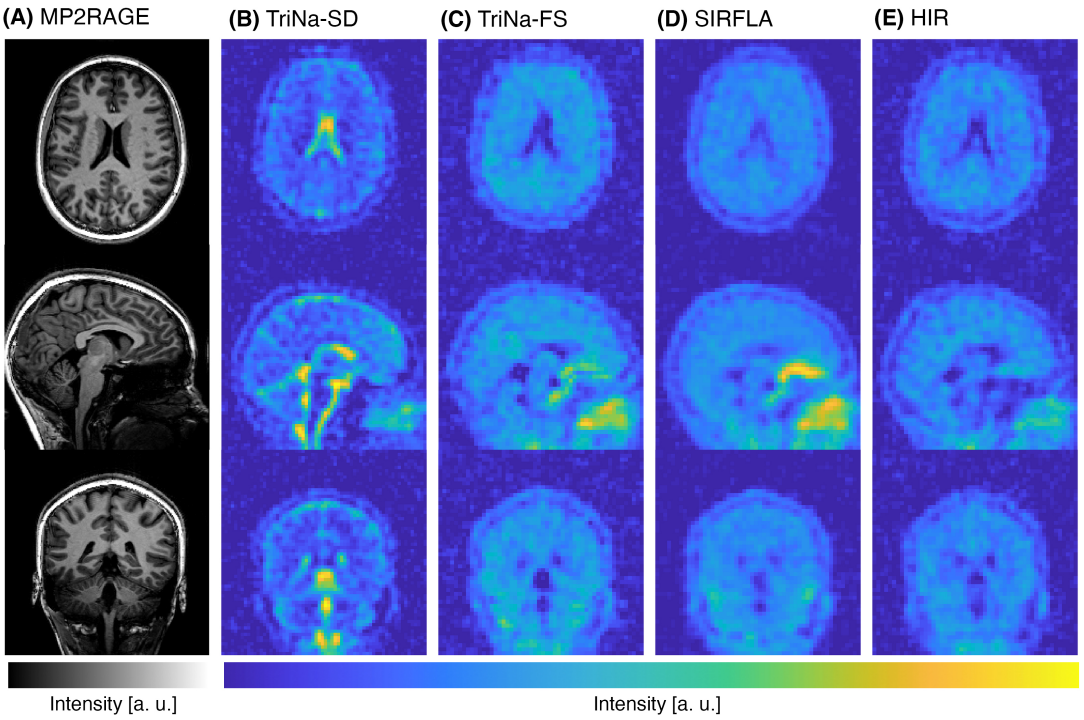

FIGURE 4.7: (A) 1 mm isotropic ^{1}H MP2RAGE anatomical image. (B) Nominal 3.1 mm isotropic TriNa-SD image, SNR is 20.6 in the CSF and 6.8 in the parietal tissue. (C) Corrected TriNa-FS image. A fringe can be seen in the base of the frontal lobe due to masking. (D) SIRFLA image. (E) HIR image. The nominal resolution is 3.8 mm isotropic for these FLAIR images. Their SNR values in the parietal tissue are 9.7, 12.2, and 8.5, respectively.

efficiency, as demonstrated by phantom and in-vivo experiments at 7 T. In addition, the B_0 inhomogeneity artifact in the FLAIR image can be corrected after acquisition. Given its advantageous efficiency and quality, TriNa could be an important tool for clinical research that relies on the dual ^{23}Na images to investigate brain pathologies, such as multiple sclerosis and gliomas.

Chapter 5

Challenges and Prospects of 2D Sodium Brain MRI

5.1 Introduction

Sodium (^{23}Na) is an essential electrolyte in the human body and is regulated by fundamental cellular activities. Its concentration anomaly could be an indication of cell damage or organ malfunction. *In-vivo* total sodium concentration (TSC) measurements by spin density-weighted (SDW) ^{23}Na MRI have provided valuable insights in many clinical studies, such as stroke, multiple sclerosis, gliomas and oesteo-arthritis (Madelin, Lee, et al., 2014; K. R. Thulborn, 2018).

^{23}Na MRI had been facing the challenge of low signals, necessitating extended scanning times for SNR compensation. This bottleneck has been significantly relieved over the past decades at the hardware level, including higher static field strength and more sensitive receiver coils (Wilferth et al., 2020). Following the hardware advancements, rapid SDW ^{23}Na MRI has become a compelling research area for their promising clinical applicability. For such a purpose, the 2D imaging technique is of interest, as it is a framework with high scan efficiency.

For 2D SDW ^{23}Na MRI, it is crucial to achieve slice selection while minimising tissue signal decay. For such a purpose, conventional full pulse excitation is disadvantageous for two reasons: (i) most of the signal is generated in the middle period of the excitation, leading to considerable relaxation loss at the end; (ii) a large refocussing gradient is required after the excitation, further prolonging the minimum TE. These limitations can be addressed using half pulses (HP). The standard HP sequence consists of the first half of an RF pulse and a slice-selective gradient, followed by a readout module (Pauly et al., 1989). Therefore, most of the signal is generated at the end of the HP, and only a minor refocussing gradient is needed to compensate the slice-selective gradient ramp down, which only delays the acquisition by a very short time. A full cycle of HP excitation involves two sequence repetitions doubling the acquisition time, with the slice-selective gradient switching its polarity between each repetition. Summing the signals from these HP repetitions abstractly applies a full RF pulse-shaped weighting to the excitation k-space, which is theoretically identical to the full pulse excitation. It has been shown that the HP excitation can reduce the TE to as short as 0.04 ms (Konstandin et al., 2011) and has been shown to improve the SNR by 26% compared to the full-pulse excitation (Wittrich et al., 2022) in ^{23}Na MRI. However, eddy currents in those slice-selective gradients can cause weighting errors, which increase with the gradient slew rate. HP slice profile distortion has been reported in several studies for ^{1}H MRI (Abe, 2013; Latta et al., 2020; Josan, Pauly, Daniel, & Pauly, 2009; Lu, Daniel, Pauly, & Butts Pauly, 2008). Nevertheless, it has not been evaluated for ^{23}Na MRI, which has to use a four-fold higher slice-selective gradient than the ^{1}H counterpart due to the lower gyromagnetic ratio of ^{23}Na nucleus.

3D imaging, a framework that most SDW ^{23}Na MRI sequences are based on, can also be used for rapid SDW ^{23}Na MRI. Although volumetric excitation introduces a high sampling requirement, 3D sequences can employ non-Cartesian acquisition schemes to undersample the k-space and save time. Owing to its incoherent property, non-Cartesian sampling can form an undersampled image with noise-like aliasing patterns, as opposed to structural overlapping in undersampled Cartesian schemes (Behl, Gnahm, Bachert, Ladd, & Nagel, 2016).

Imaging quality is influenced by various factors in addition to the framework type. Among them, the impact of relaxation can be profound in ^{23}Na MRI. Tissue signal loss can occur during excitation, especially in 2D imaging where shaped pulses are used. Furthermore, relaxation during readouts can broaden point spread functions (Rahmer et al., 2006), reducing the spatial resolution of a sequence but concurrently alleviating any existing aliasing. K-space data weighting also influences both resolution and aliasing (Pipe, 2000), akin to the relaxation effect. Finally, the overall impact can vary, dependent on the object being scanned.

Given both the advantage of high scan efficiency and the disadvantages of prolonged excitation and slice imperfection, it is unclear whether 2D imaging with HP can achieve higher image quality compared to the 3D imaging for rapid SDW ^{23}Na MRI. To determine the suitability of 2D imaging, this work (i) measured HP slice profiles for ^{23}Na MRI and evaluate the eddy current effect on the signal quality; (ii) compared 2D projection reconstruction (PR), and its counterpart, 3DPR, in terms of the image fidelity using simulations, phantom and in-vivo experiments at 7 T.

5.2 Theory and Methods

5.2.1 Slice Profile Error

Eddy currents affecting HP excitation occur during gradient ramps. The eddy current-induced field, $\vec{B}_e(t)$, can be modelled as a response to the change of the input gradient $\vec{G}$: (Bernstein, King, & Zhou, 2004)

$$\vec{B}_e(t) = \frac{d\vec{G}}{dt} \circledast g(t), \tag{5.1}$$

where $\circledast$ denotes convolution and g denotes the eddy current impulse response.

$\vec{B}_e$ induces phase error, ϕ, to the produced magnetisation. The accumulated amount during a time interval, T, can be approximated as a linear function of the slice offset,

z_0: (Bernstein et al., 2004)

$$\phi(z_0) = \gamma \int_0^T \vec{B}_e(t)\, dt \approx \gamma \left(z_0 \int_0^T G_z(t)\, dt + \int_0^T B_0(t)\, dt \right), \tag{5.2}$$

where G_z is the linear term and B_0 is the zeroth-order term of $\vec{B}_e(t)$ expanded along the z axis.

A half-sinc pulse generates the same slice frequency bandwidth (BW) as the original full-sinc pulse. According to the Fourier transform relationship between the sinc pulse and the rectangular slice profile, the BW, Δf, is determined by

$$\Delta f = 1/t_0, \tag{5.3}$$

where t_0 is the duration of the half-lobe in the HP.

The corresponding gradient amplitude to produce a slice with a thickness of Δz is

$$|\vec{G}| = \frac{2\pi\Delta f}{\gamma \Delta z}. \tag{5.4}$$

Assuming that the maximum gradient slew rate, $|\mathrm{SR}_{max}|$, is used, $T = |\vec{G}|/|\mathrm{SR}_{max}|$ and therefore,

$$\phi_{\mathrm{H}} = \phi_{\mathrm{Na}}. \tag{5.5}$$

5.2.2 Spin Density-weighted ^{23}Na MRI Simulation

SDW ^{23}Na MRI simulations were designed to include various effects, including HP slice profiles, sampling aliasing, signal relaxation, post-acquisition weighting and brain anatomy. A brain numeric phantom was produced by the following steps. First, partial volume estimation (PVE) maps for CSF, GM and WM compartments were derived from a high-resolution ^{1}H MP2RAGE image using the FAST algorithm (Zhang, Brady, & Smith, 2001). Second, the PVE maps were resampled to a lower resolution, with $84 \times 84 \times 84$ voxels in an isotropic FOV of 200 mm, and then scaled according to typical sodium concentrations. The scaling factors were 150 for CSF, 50 for GM and 30 for WM. To mimic voxel intensity variation in reality, the interim images were then point-wise multiplied with a spatially slow-varying 3D matrix, which was interpolated from a $10 \times 10 \times 10$ Gaussian distributed random numbers with zero mean and standard deviation of 0.1. The superposition of the three images was used as the ground truth (Figure 5.1A).

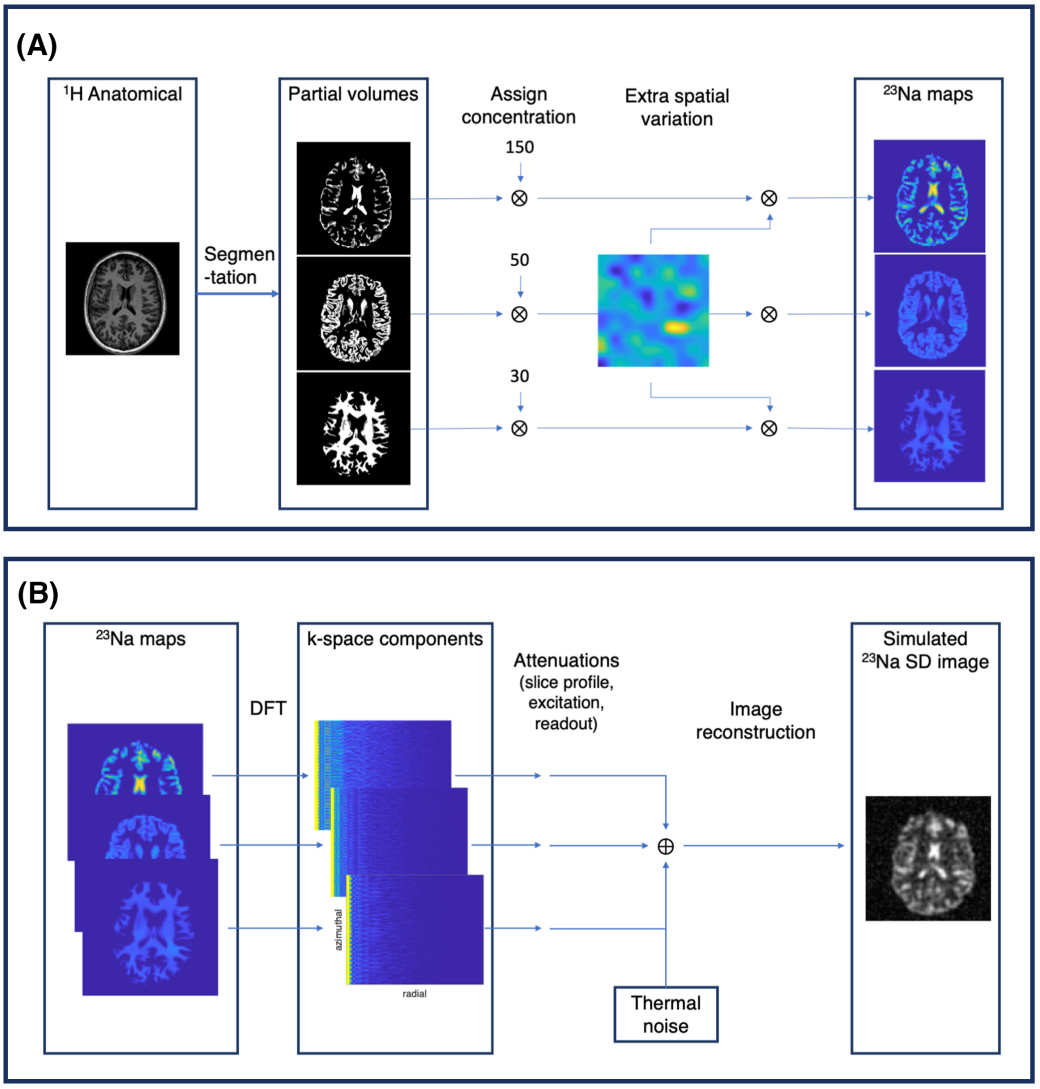

FIGURE 5.1: Simulation flowcharts showing (A) the process of creating a numeric brain phantom and (B) the readout and reconstruction simulations.

In the forward step, k-space components of each brain phantom compartment were obtained by separately performing discrete Fourier transform along projection trajectories (Figure 5.1B). For 2DPR, 500 spokes were generated for each axial slice, following the Golden Angle distribution (Winkelmann, Schaeffter, Koehler, Eggers, & Doessel, 2006). For 3DPR, 20,000 spokes were generated following Saff and Kuijlaars' distribution (Saff & Kuijlaars, 1997). A 10% signal loss was applied to the 2DPR samples to adjust for slice profile degradation, according to the phantom slice measurement in this work, which will be discussed in the following section. In addition, the relaxation effects during excitation and readout were applied, with decay rates referred to the measurements in Blunck et al. (2018). Relaxation attenuation during an HP (pulse length (TP) = 3 ms,

flip angle = 80°) and a rectangular pulse (TP = 0.5 ms, flip angle = 80°) were respectively calculated by the Spin-3/2 Bloch Equation (Wu et al., 2022). The magnitude of each forwarded k-space was weighted by corresponding T_2^* relaxation over a virtual 21 ms readout window.

For a fair comparison, simulated reconstructions were set to attain a virtual isotropic full width at half maximum (FWHM) of 5 mm. For 2DPR, the first 73 samples of each simulated projection were used and a 5-mm HP slice thickness was assumed, while the 3DPR used 84 samples. Raw data was incorporated with an additive noise, which was assumed to be Rayleigh distributed with a pragmatically chosen standard deviation. Noise energy was equivalent in both sequences since the bandwidth per sample was equal. Prior to non-uniform fast Fourier transform (NUFFT) reconstruction, Hann apodization was applied, combined with the density compensation weight W of radius k_r: $W_{2D}(k_r) = |k_r|$ and $W_{3D}(k_r) = k_r^2$.

Results of various averaging numbers N were simulated. For 2DPR, this averaging effect was achieved by scaling the noise standard deviation by $1/\sqrt{N}$. For 3DPR, the full-size k-space projections generated in the forward step were uniformly downsampled. Slice-by-slice fidelity comparisons between 2DPR and 3DPR were performed based on root mean square error (RMSE), mutual information (MI) and structural similarity (SSIM), which were calculated with respect to the ground truth and with the background voxels excluded by masking.

5.2.3 Experiments

All experiments were performed on a research 7T MRI scanner (Siemens Healthineers, Erlangen, Germany) equipped with a dual-tuned ^{1}H-^{23}Na transmit/receive head coil (QED, Mayfield Village, OH, USA) and a gradient system that allows a maximum strength of 70 mT/m and a maximum slew rate of 200 mT/m/s. HPs derived from a 3-lobe Hamming-windowed sinc were used for 2DPR slice selection, paired with a bipolar trapezoidal gradient and a subsequent short triangle refocusing gradient.

Slice profile measurement

HP slice profiles were assessed on a cylindrical phantom containing sodium sulphate solution. A 1D spin-echo sequence (Fabich, Benning, Sederman, & Holland, 2014) scanned along the physical z-gradient direction, stepping through -40, -20 and 0 mm and covering a 100 mm distance at 0.25 mm resolution for each measurement (Figure 5.2). A ^{23}Na HP

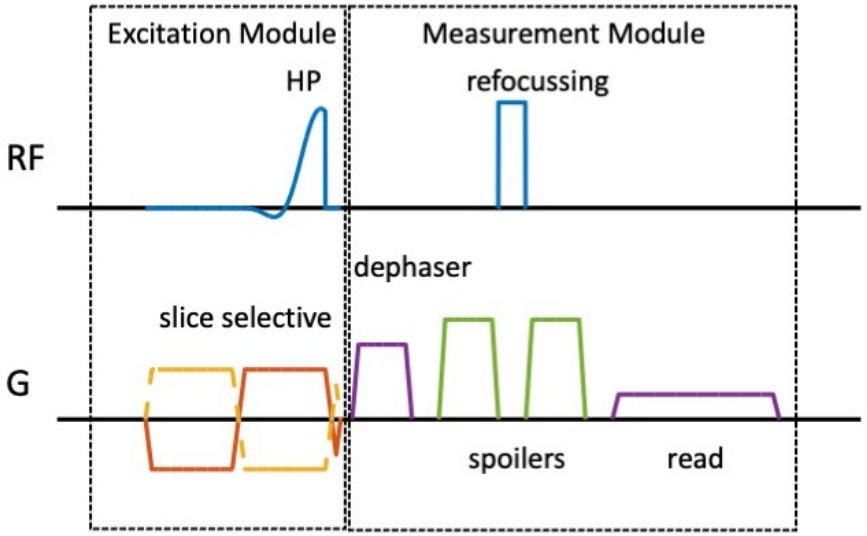

FIGURE 5.2: Pulse sequence diagram for measuring the HP slice profile. The 180° refocussing pulse is phase-cycled with a step of 90°. The dephaser gradient and the read gradient are applied in the same direction as the slice-selective gradients. The sequence is iterated four times with the refocussing pulse phase cycling. The acquired signals are then averaged to result in the slice profile for an HP excitation partition. This procedure is repeated for the other partition, which has an oppositely polarised slice selective gradient. The summation of the slice profile from each partition forms the full-pulse slice selection profile.

of 4-ms pulse length and 80° flip angle produced a prescribed 5-mm slice, corresponding to a slice BW of 500 Hz and gradient magnitude of 8.9 mT/m accordingly. Each measurement was acquired with TE/TR = 27/200 ms in 4 minutes. As a reference, the experiments were also performed in the ^{1}H channel. The slice-selective gradient and TR were adjusted to 2.3 mT/m and 4000 ms. Given sufficiently strong ^{1}H NMR signals, the acquisition time for one slice was reduced to 32 seconds. In addition, the measurement was repeated with HPs shortened to 1 ms, resulting in a slice bandwidth of 2 kHz, gradient magnitude of 32.5 mT/m for ^{23}Na and 8.9 mT/m for ^{1}H. Actual flip angles were measured by the double-angle method (Insko & Bolinger, 1993) using additionally acquired slice profiles produced by 40° excitation.

Phantom experiments

A cylindrical phantom, which consisted of saline and sodium-resolved agar and had a physical size comparable to the human head, was used for comparison. HP 2DPR signals were acquired with TP = 3 ms, slice-selective gradient = 11.8 mT/m, slice thickness = 5 mm, number of projections per HP = 500, maximum k-space radius = 0.37 mm^{-1},

BW per sample = 41.7 Hz, number of averages = 6, TE/TR = 0.25/150 ms and readout duration = 18.3 ms. TE is defined as the delay from the end of the pulse to the start of the acquisition. Considering the radial sampling (Rahmer et al., 2006) and apodization effects (Qian, Zhao, Zheng, et al., 2012), the prescribed voxel in-plane FWHM of the reconstructed image was 5×5 mm^2. The scan was repeated for two consecutive slices in order to cover a sufficiently large region of interest (ROI) for analysis. For 3DPR, a rectangular pulse (TP = 0.5 ms) was used. TE/TR = 0.15/150 ms, readout duration = 20.8 ms, BW = 41.7 Hz, number of projections = 12000. The reconstructed image has a voxel FWHM of $5 \times 5 \times 5$ mm^3. 2DPR images were registered to the 3DPR ones using the scanner coordinate system. Images with various retrospective downsampling were compared in terms of RMSE, MI and SSIM in an ROI defined by an intensity-thresholded mask, with the densely sampled 3DPR as the reference.

In-vivo experiments

In-vivo brain imaging was performed on a healthy volunteer with their consent given, using a scan protocol similar to the phantom experiments. For 2DPR, three axial slices were acquired with 1000 projections, resulting in an individual TA of 2.5 minutes. An additional sagittal slice was also acquired with 2000 projections in 5 minutes. 3DPR was obtained with 10000 projections, which were downsampled to match the 2DPR counterparts in the subsequent comparison. The densely sampled 3DPR image was used as the reference.

5.3 Results

5.3.1 Slice Profiles

Eddy current effects led to distortion in both magnitude and phase profiles, which were more manifest further away from the isocentre or with a higher slice BW as expected (Figure 5.3A). The targeted region of the slice with a BW of 500 Hz at the isocentre, which was least affected, contributed 90% of the magnitude accumulation, while the most affected slice region, with a BW of 2000 Hz and a slice shift of -40 mm, contributed 79% of the generated magnetisation (Figure 5.3B). The accumulative complex magnitude was approximately 10% smaller than the ideal value, 5 a.u. mm in the ^{23}Na slices (Figure 5.3C), indicating that HP excitation can cause signal losses. The measured ^{23}Na slices were similar to the ^{1}H counterparts.

FAs at the peak of the slice profiles were measured to be 78.8°, 78.9°, 75.5° in the ^{23}Na channel and 80.4°, 70.8°, 66.6° in the ^{1}H channel, at the slice offset of 0, -20 and -40 mm, respectively. Given such insignificant variation, their influence on the outcome can be neglected.

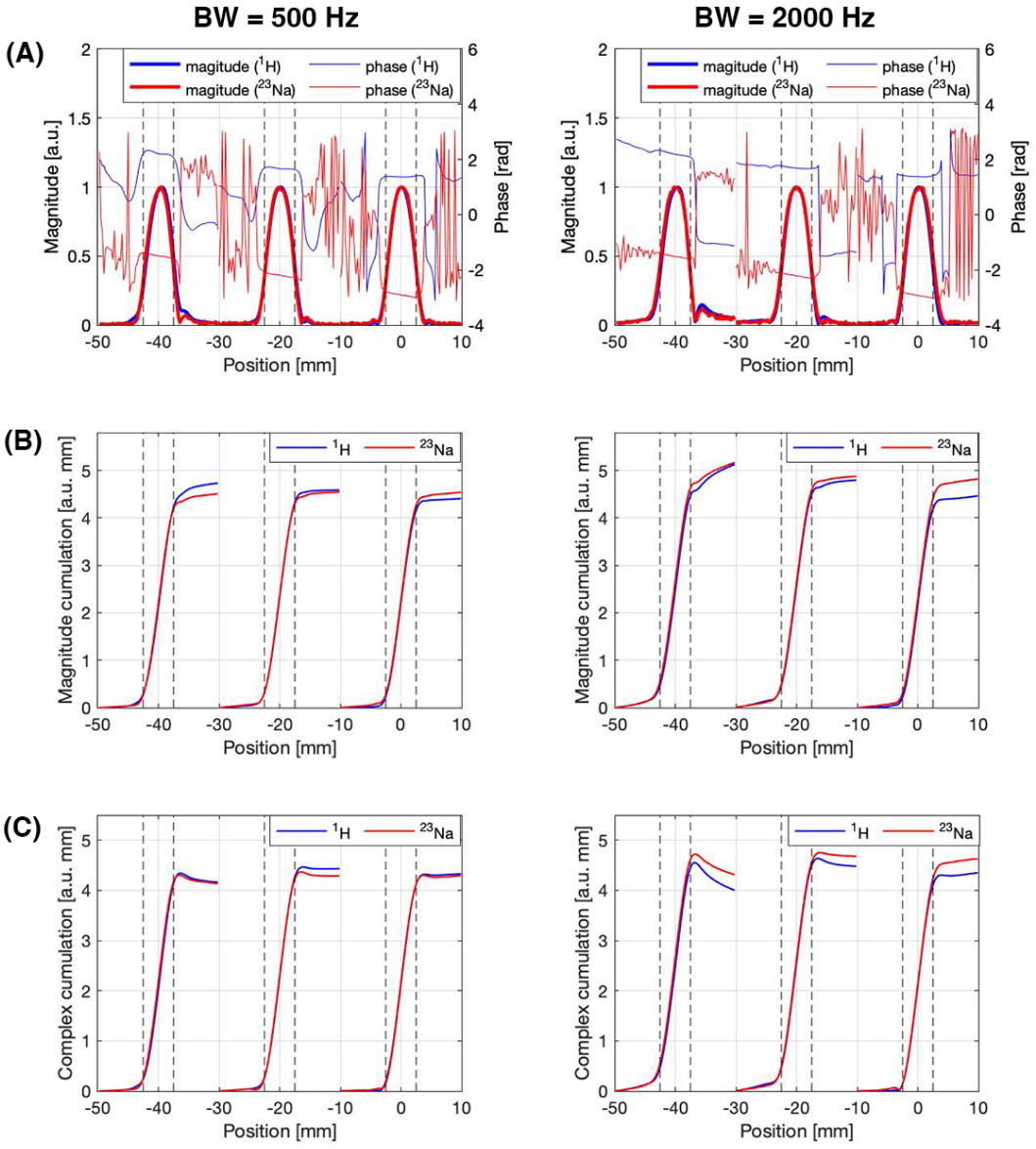

FIGURE 5.3: The measured HP slices with a bandwidth of 500 Hz in the left column and 2000 Hz in the right column. (A) The normalised magnitude and phase profiles. (B) The accumulative magnitude and (C) the accumulative complex magnitude was calculated across the ±10 mm range of each slice. The arbitrary unit (a.u.) is specifically used as the unit for the slice magnitude in this chapter. Dash lines indicate targeted slice regions.

5.3.2 Simulation

Comparisons were performed on axial slices, which were indexed from foot to head. In the cases with a low number of projections, 2DPR images exhibit significantly higher RMSE, lower MI and SSIM compared to 3DPR images, which suffered from insufficient sampling (Figure 5.4). The image quality of 3DPR became almost identical to the one of 2DPR with 20,000 projections, as the k-space was densely sampled (Figure 5.4), confirming that aliasing was the primary impact to the undersampled 3DPR.

Visual inspection on an exemplary slice validated the quantitative measurements (Figure 5.5). With 1000 projections, 2DPR and 3DPR were both affected by high noise. However, 2DPR was still able to resolve more details, as the 3DPR image contained severe streaking artifacts (Figure 5.5). Increasing the number of projections reduced the noise and, particularly for 3DPR, effectively suppressed the artifacts, reducing the performance gap between these two frameworks.

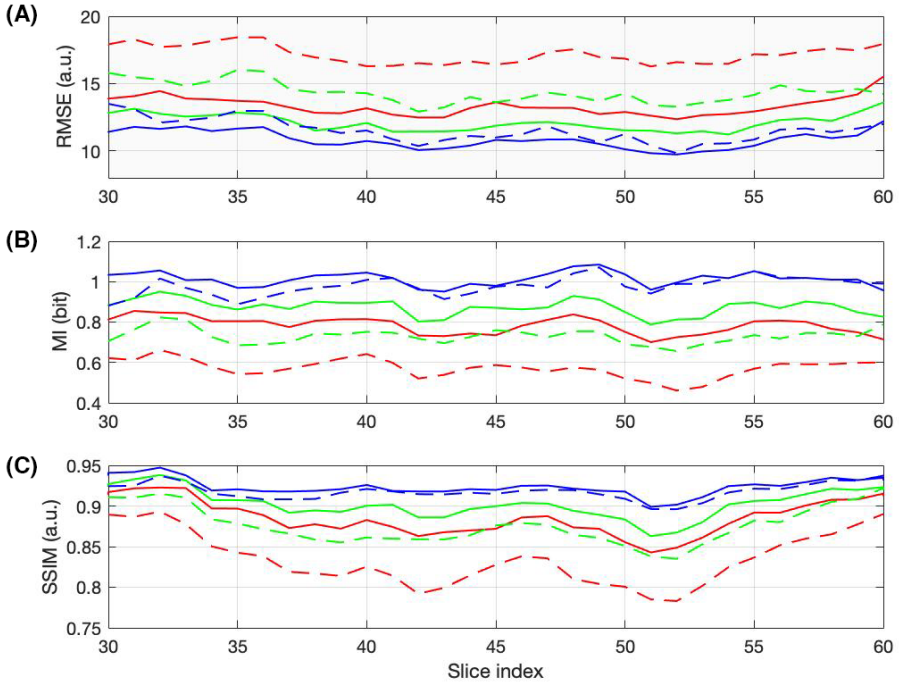

FIGURE 5.4: The 2DPR axial images (solid line) and the 3DPR images (dash line) with a total projection number of 1000 (red), 2000 (green) and 20,000 (blue) were compared in terms of (A) RMSE, (B) MI and (C) SSIM between Slice 30 and Slice 60, which cover most of the brain region.

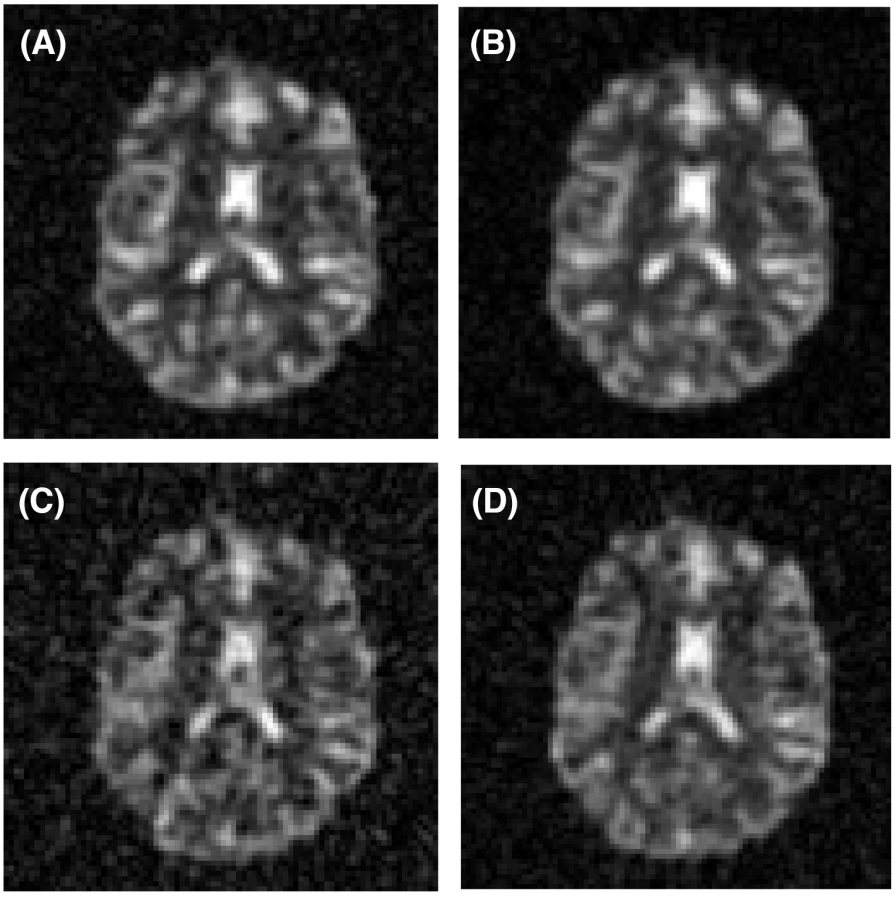

FIGURE 5.5: Simulated image Slice 48 reconstructed by 2DPR with (A) 1000 and (B) 2000 total projections and the corresponding 3DPR results reconstructed from (C) 1000 and (D) 2000 projections.

5.3.3 Phantom Experiments

In the phantom experiments, the three metrics, RMSE, MI and SSIM, demonstrated a similar trend. The difference in SSIM was minuscule, probably due to a relatively simple phantom structure. With 1000 projections, 2DPR achieved better fidelity than 3DPR, as indicated by a $\sim 30\%$ lower RMSE and a $\sim 17\%$ higher MI (Figure 5.6). As the scan extended, the fidelity scores achieved by 2DPR appear to approach certain asymptotes, which might be due to image misalignment to the referenced image. Conversely, all results showed that 3DPR performance significantly improved with more projections and indicated comparable fidelity between 2DPR and 3DPR when the number of projections is more than 2000.

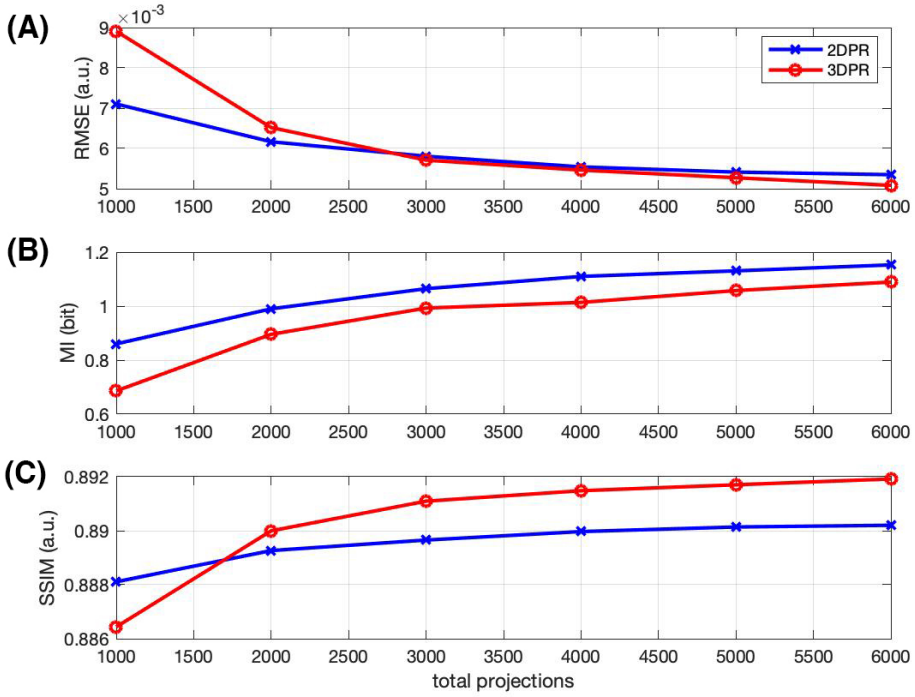

FIGURE 5.6: The phantom images of 2DPR and 3DPR with various total projections were evaluated based on (A) RMSE, (B) MI and (C) SSIM.

5.3.4 *In-vivo* Experiments

In-vivo results were similar to the simulations and phantom experiments and validated the advantage of 2DPR in rapid SDW scanning. 2DPR with 1000 projections in 2.5 minutes was able to reveal most fluid structures, while the brain structure in 3DPR images was manifestly affected by streaking artifacts (Figure 5.7).

With the number of projections doubled from 1000 to 2000, the 2DPR image achieved noise reduction while the 3DPR image experienced more significant improvement as some brain structures were recovered, including the ventricles and large sulcus (Figure 5.8). With 2000 projections, 2DPR only achieved slightly higher performance, as demonstrated by clearer fluid-tissue boundaries and smoother tissue regions. The results were in agreement with the findings from both simulations and phantom experiments.

5.4 Discussion

In this work, HP slice profiles in ^{23}Na MRI have been measured. The findings revealed that eddy currents contributed to HP profile distortion, SNR loss and out-of-slice signals as expected. However, these adverse effects were maintained at an acceptable level

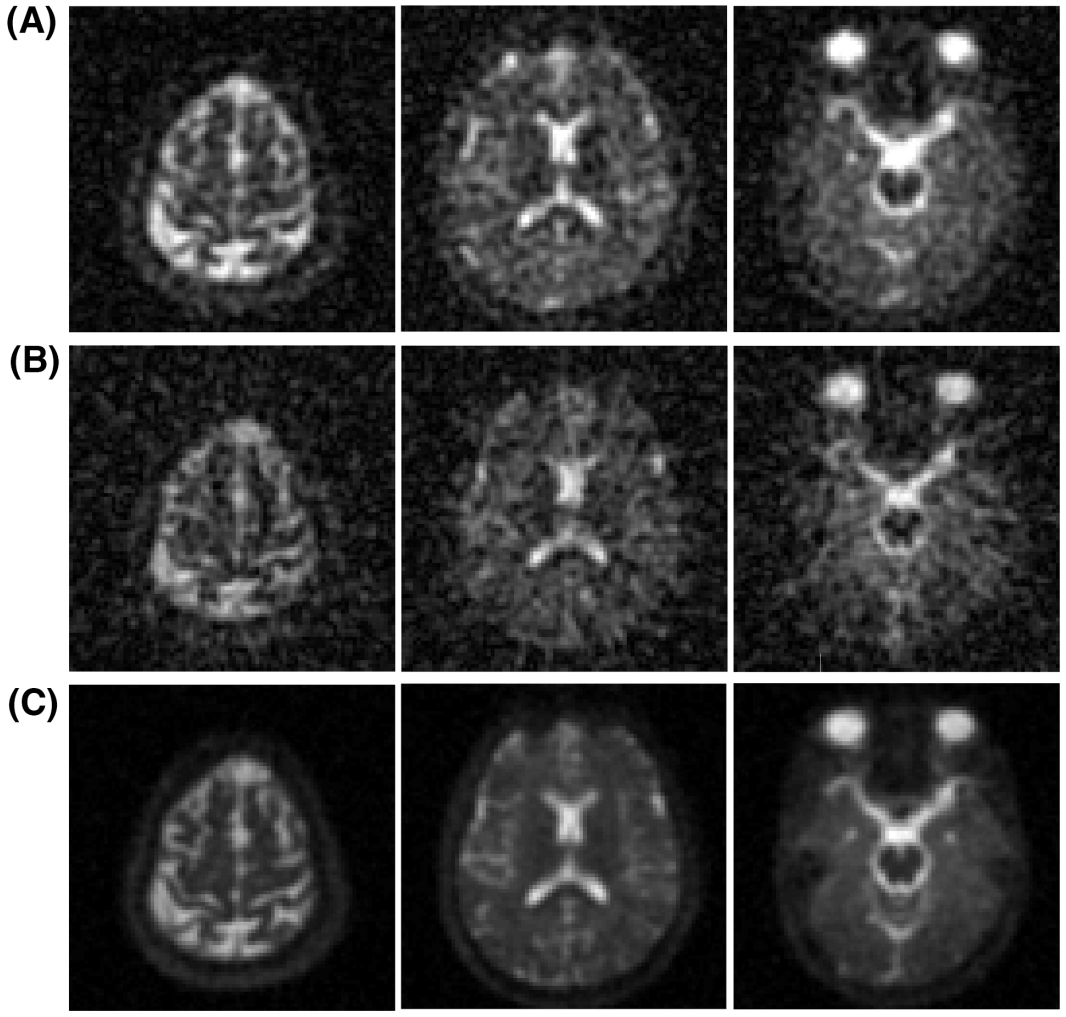

FIGURE 5.7: Acquired *in-vivo* brain images. (A) Three 2DPR axial slices are presented in the first row, each was acquired in 1000 projections in 2.5 minutes. (B) Corresponding axial slices from 3DPR with 1000 projections are displayed. (C) Densely-sampled 3DPR with 10000 projections are shown for reference.

up to a slice BW of 2000 Hz within a typical slice offset range. In an extreme slice position, for example, -40 mm along the gradient z-direction, the slice profile degradation can be substantial. Nevertheless, such a large slice offset is not typically employed for head imaging. In addition, it has been demonstrated that the quality of ^{23}Na HP excitation is comparable to the ^{1}H counterpart, despite the use of a much stronger slice-selective gradient. This is because the lower ^{23}Na gyromagnetic ratio, compared to ^{1}H, restrains phase accrual and thus counters the increased eddy current effects induced by the requirement of a longer gradient ramping duration.

2DPR and 3DPR were compared in terms of image fidelity in SDW ^{23}Na MRI of the brain. In both simulations and phantom experiments, quantitative fidelity measures, including RMSE, MI and SSIM, suggested that 2DPR can achieve superior accuracy

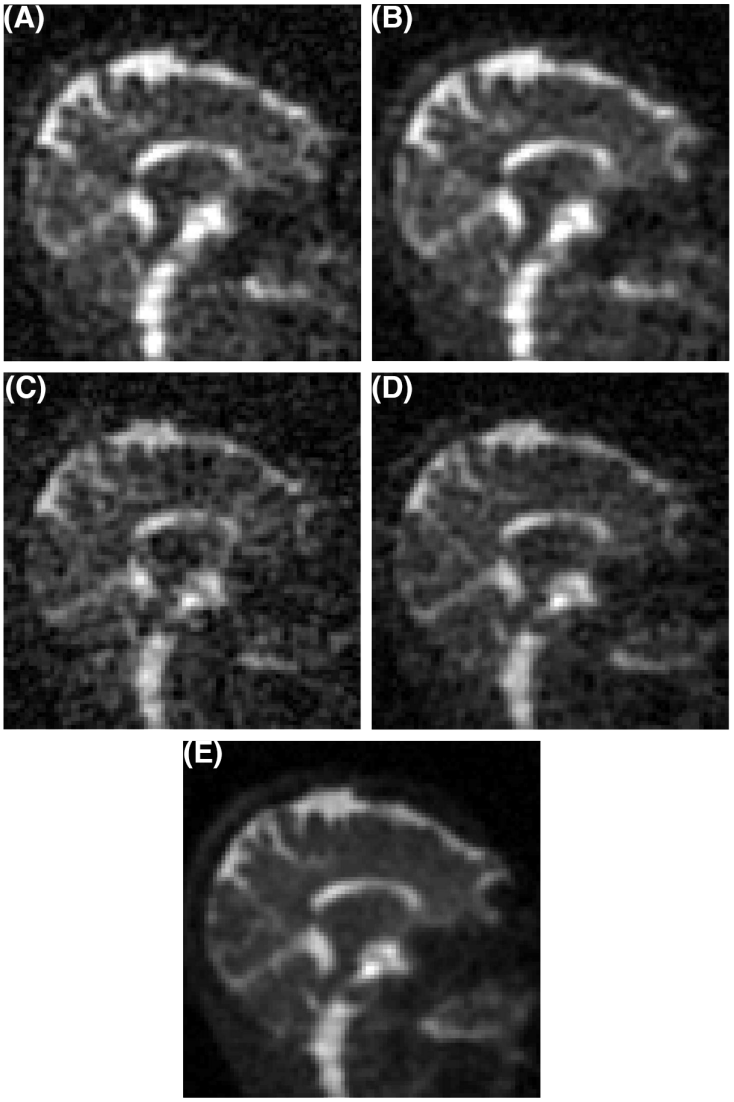

FIGURE 5.8: *In-vivo* sagittal slices reconstructed by 2DPR with (A) 1000 projections and (B) 2000 projections. Corresponding slices from the undersampled 3DPR with (C) 1000 projections, (D) 2000 projections and (E) 10000 projections.

when the number of sequence repetitions is limited. Indeed, its advantage of sampling efficiency outweighed the disadvantages of slice distortion and signal decay. Conversely, 3DPR excessively violated the Nyquist criterion under such a constraint, inevitably resulting in strong undersampling aliasing. These artifacts remained at a significant level even after mitigative effects, including relaxation blurring during readouts and low pass-filtered reconstruction.

Despite its low SNR, rapid SDW 2DPR may have several potential applications in neuroimaging. In stroke research, initial studies have indicated that ^{23}Na concentrations are associated with ischemic stroke onset times (Hussain et al., 2009; Neumaier-Probst et al., 2015). Rapid SDW 2DPR can be added to a stroke imaging protocol, which

usually includes several fundamental ^{1}H sequences, extending the total acquisition time by only a few minutes. This advantage may benefit studies recruiting acute stroke patients, where saving scan time is crucial. In the research field of ^{23}Na fMRI, recent studies using 3D sequences can acquire a single time frame in 60 seconds with 4-fold undersampling (Gandini Wheeler-Kingshott et al., 2018) or in 30 seconds using view-sharing (Bydder et al., 2019). With higher efficiency, 2DPR can improve the temporal resolution of ^{23}Na fMRI. The low SNR issue in rapid ^{23}Na imaging can be addressed by recruiting more participants or increasing image frames in these studies.

2D imaging and 3D imaging are different in other aspects besides the fidelity performance tested in this work. On the one hand, 3D imaging can cover a large imaging volume, whereas multi-slice 2D ^{23}Na MRI to match such 3D volume might be challenging due to specific absorption rate constraints. On the other hand, 2D imaging has flexibility in slice thickness, which is sorely determined by excitation. This allows a straightforward formation of elongated voxels that are beneficial for in-plane resolution and SNR. In contrast, attaining anisotropic voxels with 3D UTE sequences faces several challenges: (i) Post-acquisition slice combination can increase SNR but suffer SNR efficiency loss because this operation, which is equivalent sinc-windowing in the k-space, attenuates high-frequency signals; (ii) Simple adapted acquisition trajectories with reduced gradient amplitude along the voxel longitudinal direction also results in low SNR efficiency due to increased sampling inhomogeneity; (iii) Specialised methods such as acquisition weighted stack of spirals (Qian, Zhao, Zheng, et al., 2012) and anisotropic density-adaptive 3DPR (Nagel et al., 2012) can attain optimal SNR efficiency. However, since the k-space sampling along the voxel longitudinal direction is substantially truncated, anisotropic 3D imaging may be sensitive to spectral leakage. This effect could become pronounced in coarse ^{23}Na images. In practice, these aspects should also be considered in addition to image fidelity.

This study has a few limitations. Firstly, the implemented HP excitation required a small refocusing gradient to offset the ramp-down of the slice-selective gradient that delayed the subsequent readout by a few hundred milliseconds. This refocusing gradient can be removed using the variable-rate selective excitation technique (Conolly et al., 1988). In addition, the HP excitation in this work used large FAs. For improved large-FA slice profiles, the Shinnar-Le Roux algorithm can be used to design the pulse shape (Pauly, 2006). Secondly, the work focuses on only the standard PR sequences and traditional reconstruction methods. Future assessment and comparison can be extended to advanced PR schemes, such as density adaptive PR (Nagel et al., 2009; Konstandin et al., 2011) and twist projection imaging (Boada, Gillen, et al., 1997), as well as compressed sensing recontruction (Madelin, Chang, Otazo, Jerschow, & Regatte, 2012; Behl et al., 2016; Blunck et al., 2020; Utzschneider et al., 2021).

5.5 Conclusion

In conclusion, the HP slice profile measurement in this work confirmed that satisfactory slice quality can be attained for ^{23}Na imaging. Moreover, the comparison results suggested that 2DPR can achieve higher image fidelity than undersampled 3DPR in rapid SDW ^{23}Na MRI. Future comparisons can focus on SNR-optimised density-adapted sequences.

Chapter 6

Conclusion

6.1 Thesis Contribution

This thesis investigates ^{23}Na MRI sequences with the purpose of advancing their performances for *in-vivo* brain imaging. Particularly, the presented work investigated the ^{23}Na MRI sequence concerning the theory, simulation, designs and analysis.

In MRI research, simulation is an effective method to provide efficient solutions, serving as an alternative to actual experiments which can be time-consuming or infeasible. ^{23}Na MRI particularly relies on simulations as part of its methodology to tackle the sophisticated spin-3/2 dynamics.

The knowledge of ^{23}Na spin-3/2 dynamics underpins the sequence design. This concerns quantum mechanics and was extended from the field of NMR. One of the theories that have a profound influence on ^{23}Na MRI was first proposed in Hancu et al. (2000) and further elaborated in van der Maarel (2003a, 2003b), which formulated the relaxation using spectral densities based on the Redfield theory. It elucidated relaxation formulas for different conditions and derived an approximation for biological environments. However, as it served as a theory for NMR experiments, this formalism did not adequately address the off-resonance effect. Succeeding *in-vivo* MRI simulators have included the terms for the off-resonance evolution to simulate the gradient and the susceptibility effect, presuming that the relaxation expressions do not change (R. Stobbe, 2010; Madelin, Lee, et al., 2014; Kratzer et al., 2021).

Chapter 3 described a mathematical treatment to prove that the relaxation formalism is applicable to typical spin-3/2 nuclei MRI for biological environments (as opposed to other environments such as crystal liquid), taking a step forward to consolidate the formalism by Hancu et al. (1999). The proposed "Spin-3/2 Bloch Equation" is straightforward and well posed to be integrated with the Runge-Kutta algorithm, which is a versatile solver with a dynamically optimised step size. This is beneficial for the simulation efficacy, especially for scenarios with time-varying inputs, for example, adiabatic excitation.

The combination of spin-density weighting and fluid suppression, which are among the most common ^{23}Na MRI contrast, has gained increasing interest as its clinical potential has been shown by recent studies (Nunes Neto et al., 2018; Mennecke et al., 2021). The spin-density weighting as a standard UTE MRI is straightforward. Improvements for ^{23}Na MRI can be realised primarily on the readout aspect where the gradient waveforms were optimised for SNR. In terms of fluid suppression, an inversion preparation step is necessitated in addition to the UTE acquisition. Current practice has widely adopted

the SIRFLA method which extends the duration of the inversion pulse to reduce the SAR and enhance the tissue signal strength. This, however, can result in undesired fluid residue artifacts as the elongated inversion pulse inevitably becomes sensitive to the B_0 inhomogeneity.

Chapter 4 proposed a novel design, Triple Pulse ^{23}Na MRI Sequence (TriNa), which integrates the acquisition of the dual contrast that attains several benefits. Firstly, sequence TR is shorter when compared to the sum of TRs of the standalone sequences. Secondly, similar to the SIRFLA, the tissue signal strength of the fluid-suppressed image is enhanced by relaxation differentiation. Lastly, a post-processing method is available for B_0 inhomogeneity artifact correction. Phantom and *in-vivo* experiments have validated the overall SNR efficiency improvement and the correction method.

The rapid acquisition capability of ^{23}Na MRI can be of particular interest, given that it is usually a scan supplementary to ^{1}H MRI, especially for certain multiple-sequence imaging protocols aiming to shorten the total scanning session into a practical duration. In this case, one might consider 2D imaging which is favoured for reduced encoding requirements, following the conventions in ^{1}H MRI. However, it is unclear if this approach can sustain such an advantage in ^{23}Na MRI over the 3D imaging sequence. This is because the differences in the underlying mechanisms, including ^{23}Na magnetisation relaxation, sampling patterns, reconstruction weighting, readout noise and hardware-induced artifacts, jointly contribute to the image quality. While existing literature has developed numerous theories for the MRI sequence design (Rahmer et al., 2006; Pipe, 2000; Tsai & Nishimura, 2000; Lauzon & Rutt, 1996), they are limited to specific aspects and unable to predict the overall effect. Therefore, simulations and experiments are needed to complement the theory in terms of the sequences' actual performance, particularly for ^{23}Na MRI on which knowledge and experience are scarce.

Chapter 5 compared the image fidelity between 2D radial acquisition and the 3D counterpart for the spin density-weighted ^{23}Na MRI. The study consists of two parts. First, as self-refocussing half pulses were implemented for the best SNR of 2D ^{23}Na MRI (Wittrich et al., 2022), concerns arose regarding the potential compromise of slice profile due to the half pulse's susceptibility to gradient eddy currents. Our phantom experiment suggests that the slice profile can be satisfactory for a moderately intensive half pulse, and the ^{23}Na slice profile quality is comparable to the ^{1}H counterpart even though a higher gradient strength that induces stronger eddy currents is used. Second, the 2D and 3D sequences were compared by comprehensive simulations with a numeric brain and further validated by phantom and *in-vivo* experiments. The study confirmed that the half pulse 2D radial sequence can achieve higher fidelity in rapid spin density-weighted ^{23}Na MRI.

6.2 Future Work

Over the past two decades, the development of ^{23}Na MRI has made significant progress and ongoing preclinical research continues exploring its clinical applicability (Madelin & Regatte, 2013; Gast et al., 2023). Research in ^{23}Na MRI sequence techniques was fueled by the hardware advancement during that time, especially the increased capacity of ultra high-field scanners and dedicated ^{23}Na-tuned or ^{1}H/^{23}Na dual-tuned coils (Giovannetti et al., 2021; Gast et al., 2023), which together have ensured image quality for preclinical *in-vivo* experiments.

The ongoing development of ^{23}Na phased array receiver coils (Lommen et al., 2016; Qian, Zhao, Wiggins, et al., 2012) will bring in both sequence innovation opportunities and challenges. Array coils provide enhanced sensitivity, alleviating the low-SNR bottleneck so that sequence design can focus on improvements such as faster encoding or artifact reduction. Moreover, to meet the need for accurate quantification and to minimise SNR loss in coil combination, dedicated techniques for accelerated ^{23}Na MRI, aiming to achieve a uniform image and optimal SNR, are warranted.

The trend of combined ^{1}H and ^{23}Na MRI has become increasingly popular with the emergence of the multinuclear receiver module that enables interleaved or simultaneous readout. Various functionalities have developed, such as ^{1}H MR fingerprinting/^{23}Na imaging (Yu et al., 2020) and ^{1}H navigator/motion-corrected ^{23}Na imaging (Wilferth et al., 2022). More combinations are waiting to be explored.

In summary, the development of sequence design will continue to foster the growth of ^{23}Na MRI and realise its clinical potential.

References

Abe, T. (2013). Half radiofrequency pulse excitation with a dedicated prescan to correct eddy current effect and gradient delay. *Medical Physics*, *40*(3), 032304.

Baron, P., Potze, J. H., & Sijens, P. E. (2023). Influence of reference tube location on the measured sodium concentrations in calf muscles using a birdcage coil at 3T. *Magnetic Resonance in Medicine*.

Behl, N. G., Gnahm, C., Bachert, P., Ladd, M. E., & Nagel, A. M. (2016). Three-dimensional dictionary-learning reconstruction of ^{23}Na MRI data. *Magnetic Resonance in Medicine*, *75*(4), 1605–1616.

Berg, J., Tymoczko, J., & Stryer, L. (2002). The transport of molecules across a membrane may be active or passive. *Biochemistry. 5th edition. New York, WH Freeman & Co*, 1119-1120.

Bernstein, M. A., King, K. F., & Zhou, X. J. (2004). Correction gradients. In *Handbook of MRI Pulse Sequences* (pp. 292–362). Elsevier.

Biller, A., Pflugmann, I., Badde, S., Diem, R., Wildemann, B., Nagel, A. M., ... Kleesiek, J. (2016). Sodium MRI in multiple sclerosis is compatible with intracellular sodium accumulation and inflammation-induced hyper-cellularity of acute brain lesions. *Scientific Reports*, *6*(1), 1–10.

Blunck, Y. (2018). *Techniques for signal acquisition, reconstruction and analysis in sodium magnetic resonance imaging* (PhD thesis). The University of Melbourne.

Blunck, Y., Josan, S., Taqdees, S. W., Moffat, B. A., Ordidge, R. J., Cleary, J. O., & Johnston, L. A. (2018). 3D-multi-echo radial imaging of ^{23}Na (3D-MERINA) for time-efficient multi-parameter tissue compartment mapping: 3D-Multi-Echo Radial Imaging of ^{23}Na (3D-MERINA). *Magnetic Resonance in Medicine*, *79*(4), 1950–1961.

Blunck, Y., Kolbe, S. C., Moffat, B. A., Ordidge, R. J., Cleary, J. O., & Johnston, L. A. (2020). Compressed sensing effects on quantitative analysis of undersampled human brain sodium MRI. *Magnetic Resonance in Medicine*, *83*(3), 1025–1033.

Boada, F. E., Gillen, J. S., Shen, G. X., Chang, S. Y., & Thulborn, K. R. (1997). Fast three dimensional sodium imaging. *Magnetic Resonance in Medicine*, *37*(5),

706–715.

Boada, F. E., Shen, G. X., Chang, S. Y., & Thulborn, K. R. (1997). Spectrally weighted twisted projection imaging: reducing T_2 signal attenuation effects in fast three-dimensional sodium imaging. *Magnetic Resonance in Medicine*, *38*(6), 1022–1028.

Bowden, G. J., & Hutchison, W. D. (1986). Tensor operator formalism for multiple-quantum NMR: 1. spin-1 nuclei. *Journal of Magnietc Resonance*, *67*, 415-437.

Bracewell, R. N., & Bracewell, R. N. (1986). *The fourier transform and its applications* (Vol. 31999). McGraw-Hill New York.

Brown, R. W., Cheng, Y.-C. N., Haacke, E. M., Thompson, M. R., & Venkatesan, R. (2014). *Magnetic resonance imaging: physical principles and sequence design.* John Wiley & Sons.

Burstein, D., & Springer Jr, C. S. (2019). Sodium MRI revisited. *Magnetic Resonance in Medicine*, *82*(2), 521–524.

Bydder, M., Zaaraoui, W., Ridley, B., Soubrier, M., Bertinetti, M., Confort-Gouny, S., ... Ranjeva, J.-P. (2019). Dynamic 23Na MRI - A non-invasive window on neuroglial-vascular mechanisms underlying brain function. *NeuroImage*, *184*, 771–780.

Chapman, B. E., Naumann, C., Philp, D. J., Eliav, U., Navon, G., & Kuchel, P. W. (2010). z-spectra of $^{23}Na^{+}$ in stretched gels: Quantitative multiple quantum analysis. *Journal of Magnetic Resonance*, *205*(2), 260–268.

Conolly, S., Nishimura, D., Macovski, A., & Glover, G. (1988). Variable-rate selective excitation. *Journal of Magnetic Resonance*, *78*(3), 440–458.

Coste, A., Boumezbeur, F., Vignaud, A., Madelin, G., Reetz, K., Le Bihan, D., ... Romanzetti, S. (2019). Tissue sodium concentration and sodium T_1 mapping of the human brain at 3 T using a Variable Flip Angle method. *Magnetic Resonance Imaging*, *58*, 116–124.

Fabich, H. T., Benning, M., Sederman, A. J., & Holland, D. J. (2014). Ultrashort echo time (UTE) imaging using gradient pre-equalization and compressed sensing. *Journal of Magnetic Resonance*, *245*, 116–124.

Feldman, R. E., Stobbe, R., Watts, A., & Beaulieu, C. (2013). Sodium imaging of the human knee using soft inversion recovery fluid attenuation. *Journal of Magnetic Resonance*, *234*, 197–206.

Fiege, D. P., Romanzetti, S., Mirkes, C. C., Brenner, D., & Shah, N. J. (2013). Simultaneous single-quantum and triple-quantum-filtered MRI of ^{23}Na (SISTINA). *Magnetic Resonance in Medicine*, *69*(6), 1691–1696.

Fleysher, L., Oesingmann, N., & Inglese, M. (2010). B_0 inhomogeneity-insensitive triple-quantum-filtered sodium imaging using a 12-step phase-cycling scheme. *NMR in Biomedicine*, *23*(10), 1191–1198.

Gandini Wheeler-Kingshott, C. A. M., Riemer, F., Palesi, F., Ricciardi, A., Castellazzi, G., Golay, X., ... D'Angelo, E. U. (2018). Challenges and Perspectives of Quantitative Functional Sodium Imaging (fNaI). *Frontiers in Neuroscience*, *12*.

Garren, K. R. (1968). Bounds for the eigenvalues of a matrix. In (Vol. 4373, p. 6-7). National Aeronautics and Space Administration.

Gast, L. V., Platt, T., Nagel, A. M., & Gerhalter, T. (2023). Recent technical developments and clinical research-applications of sodium (^{23}Na) MRI. *Progress in Nuclear Magnetic Resonance Spectroscopy*.

Gast, L. V., Völker, S., Utzschneider, M., Linz, P., Wilferth, T., Müller, M., ... Nagel, A. M. (2021). Combined imaging of potassium and sodium in human skeletal muscle tissue at 7 T. *Magnetic Resonance in Medicine*, *85*(1), 239–253.

Gerhalter, T., Chen, A. M., Dehkharghani, S., Peralta, R., Adlparvar, F., Babb, J. S., ... Madelin, G. (2021). Global decrease in brain sodium concentration after mild traumatic brain injury. *Brain Communications*, *3*(2), fcab051.

Gilles, A., Nagel, A. M., & Madelin, G. (2017). Multipulse sodium magnetic resonance imaging for multicompartment quantification: Proof-of-concept. *Scientific Reports*, *7*(1), 17435.

Giovannetti, G., Flori, A., Martini, N., Francischello, R., Aquaro, G. D., Pingitore, A., & Frijia, F. (2021). Sodium radiofrequency coils for magnetic resonance: From design to applications. *Electronics*, *10*(15), 1788.

Gudbjartsson, H., & Patz, S. (1995). The Rician distribution of noisy MRI data. *Magnetic Resonance in Medicine*, *34*(6), 910–914.

Hancu, I., Boada, F. E., & Shen, G. X. (1999). Three-dimensional triple-quantum-filtered ^{23}Na imaging of in vivo human brain. *Magnetic Resonance in Medicine*, *42*, 1146-54.

Hancu, I., van der Maarel, J. R. C., & Boada, F. E. (2000). A model for the dynamics of spins 3/2 in biological media: Signal loss during radiofrequency excitation in triple-quantum-filtered sodium MRI. *Journal of Magnetic Resonance*, *147*(2), 179–191.

Hoesl, M. A., Schad, L. R., & Rapacchi, S. (2020). Efficient ^{23}Na triple-quantum signal imaging on clinical scanners: Cartesian imaging of single and triple-quantum ^{23}Na (CRISTINA). *Magnetic Resonance in Medicine*, *84*(5), 2412–2428.

Huhn, K., Engelhorn, T., Linker, R. A., & Nagel, A. M. (2019). Potential of sodium MRI as a biomarker for neurodegeneration and neuroinflammation in multiple sclerosis. *Frontiers in Neurology*, 84.

Hussain, M. S., Stobbe, R. W., Bhagat, Y. A., Emery, D., Butcher, K. S., Manawadu, D., ... Beaulieu, C. (2009). Sodium imaging intensity increases with time after human ischemic stroke. *Annals of Neurology*, *66*(1), 55–62.

Inglese, M., Madelin, G., Oesingmann, N., Babb, J., Wu, W., Stoeckel, B., ... Johnson, G. (2010). Brain tissue sodium concentration in multiple sclerosis: a sodium imaging study at 3 Tesla. *Brain*, *133*(3), 847–857.

Insko, E., & Bolinger, L. (1993). Mapping of the radiofrequency field. *Journal of Magnetic Resonance*, *103*(1), 82–85.

Jackson, J. I., Meyer, C. H., Nishimura, D. G., & Macovski, A. (1991). Selection of a convolution function for Fourier inversion using gridding. *IEEE Transactions on Medical Imaging*, *10*(3), 473–478.

Josan, S., Pauly, J. M., Daniel, B. L., & Pauly, K. B. (2009). Double half RF pulses for reduced sensitivity to eddy currents in UTE imaging. *Magnetic Resonance in Medicine*, *61*(5), 1083–1089.

Keeler, J. (2010). *Understanding NMR spectroscopy*. John Wiley & Sons.

Kharrazian, R., & Jakob, P. M. (2006). Dynamics of ^{23}Na during completely balanced steady-state free precession. *Journal of Magnetic Resonance*, *179*(1), 73–84.

Konstandin, S., & Nagel, A. M. (2013). Performance of sampling density-weighted and postfiltered density-adapted projection reconstruction in sodium magnetic resonance imaging. *Magnetic Resonance in Medicine*, *69*(2), 495–502.

Konstandin, S., & Nagel, A. M. (2014). Measurement techniques for magnetic resonance imaging of fast relaxing nuclei. *Magnetic Resonance Materials in Physics, Biology and Medicine*, *27*(1), 5–19.

Konstandin, S., Nagel, A. M., Heiler, P. M., & Schad, L. R. (2011). Two-dimensional radial acquisition technique with density adaption in sodium MRI. *Magnetic Resonance in Medicine*, *65*(4), 1090–1096.

Konstandin, S., & Schad, L. R. (2013). Two-dimensional radial sodium heart MRI using variable-rate selective excitation and retrospective electrocardiogram gating with golden angle increments: 2D radial sodium heart MRI. *Magnetic Resonance in Medicine*, *70*(3), 791–799.

Kratzer, F. J., Flassbeck, S., Nagel, A. M., Behl, N. G., Knowles, B. R., Bachert, P., ... Schmitter, S. (2020). Sodium relaxometry using ^{23}Na MR fingerprinting: A proof of concept. *Magnetic Resonance in Medicine*, *84*(5), 2577–2591.

Kratzer, F. J., Flassbeck, S., Schmitter, S., Wilferth, T., Magill, A. W., Knowles, B. R., ... Nagel, A. M. (2021). 3D sodium (^{23}Na) magnetic resonance fingerprinting for time-efficient relaxometric mapping. *Magnetic Resonance in Medicine*, *86*(5), 2412-2425.

Latta, P., Starčuk Jr, Z., Kojan, M., Gruwel, M. L., Tomanek, B., Trattnig, S., & Juras, V. (2020). Simple compensation method for improved half-pulse excitation profile with rephasing gradient. *Magnetic Resonance in Medicine*, *84*(4), 1796–1805.

Lauzon, M. L., & Rutt, B. K. (1996). Effects of polar sampling in k-space. *Magnetic Resonance in Medicine*, *36*(6), 940–949.

Lee, J.-S., Regatte, R. R., & Jerschow, A. (2009). Optimal excitation of ^{23}Na nuclear spins in the presence of residual quadrupolar coupling and quadrupolar relaxation. *The Journal of Chemical Physics*, *131*(17), 174501.

Lee, J.-S., Xia, D., Madelin, G., & Regatte, R. R. (2016). Sodium inversion recovery MRI on the knee joint at 7 T with an optimal control pulse. *Journal of Magnetic Resonance*, *262*, 33–41.

Levitt, M. H. (2008). *Spin dynamics: basics of nuclear magnetic resonance*. John Wiley & Sons.

Liesen, J., & Mehrmann, V. (2015). Linear algebra. In (p. 85-86). Springer.

Lommen, J. M., Flassbeck, S., Behl, N. G., Niesporek, S., Bachert, P., Ladd, M. E., & Nagel, A. M. (2018). Probing the microscopic environment of ^{23}Na ions in brain tissue by MRI: on the accuracy of different sampling schemes for the determination of rapid, biexponential decay at low signal-to-noise ratio. *Magnetic Resonance in Medicine*, *80*(2), 571–584.

Lommen, J. M., Resmer, F., Behl, N. G., Sauer, M., Benkhedah, N., Bitz, A. K., ... Nagel, A. M. (2016). Comparison of a 30-channel head array with a birdcage for ^{23}Na MRI at 7 Tesla. In *Proceedings of the international society for magnetic resonance in medicine* (Vol. 24, p. 3974).

Lu, A., Atkinson, I. C., Claiborne, T. C., Damen, F. C., & Thulborn, K. R. (2010). Quantitative sodium imaging with a flexible twisted projection pulse sequence. *Magnetic Resonance in Medicine*, *63*(6), 1583–1593.

Lu, A., Daniel, B. L., Pauly, J. M., & Butts Pauly, K. (2008). Improved slice selection for R_2^* mapping during cryoablation with eddy current compensation. *Journal of Magnetic Resonance Imaging*, *28*(1), 190–198.

Madelin, G., Babb, J., Xia, D., Chang, G., Krasnokutsky, S., Abramson, S. B., ... Regatte, R. R. (2013). Articular cartilage: evaluation with fluid-suppressed 7.0-T sodium MR imaging in subjects with and subjects without osteoarthritis. *Radiology*, *268*(2), 481–491.

Madelin, G., Chang, G., Otazo, R., Jerschow, A., & Regatte, R. R. (2012). Compressed sensing sodium MRI of cartilage at 7T: Preliminary study. *Journal of Magnetic Resonance*, *214*, 360–365.

Madelin, G., Kline, R., Walvick, R., & Regatte, R. R. (2014). A method for estimating intracellular sodium concentration and extracellular volume fraction in brain in vivo using sodium magnetic resonance imaging. *Scientific Reports*, *4*, 4763.

Madelin, G., Lee, J.-S., Inati, S., Jerschow, A., & Regatte, R. R. (2010). Sodium inversion recovery MRI of the knee joint in vivo at 7T. *Journal of Magnetic Resonance*, *207*(1), 42–52.

Madelin, G., Lee, J.-S., Regatte, R. R., & Jerschow, A. (2014). Sodium MRI: Methods

and applications. *Progress in Nuclear Magnetic Resonance Spectroscopy*, *79*, 14–47.

Madelin, G., & Regatte, R. R. (2013). Biomedical applications of sodium MRI in vivo. *Journal of Magnetic Resonance Imaging*, *38*(3), 511–529.

Man, P. P. (2006). Quadrupole Couplings in Nuclear Magnetic Resonance, General. In R. A. Meyers (Ed.), *Encyclopedia of Analytical Chemistry* (p. 12224–12265). John Wiley & Sons, Ltd.

Maril, N., Rosen, Y., Reynolds, G. H., Ivanishev, A., Ngo, L., & Lenkinski, R. E. (2006). Sodium MRI of the human kidney at 3 Tesla. *Magnetic Resonance in Medicine*, *56*(6), 1229–1234.

Matthies, C., Nagel, A. M., Schad, L. R., & Bachert, P. (2010). Reduction of B_0 inhomogeneity effects in triple-quantum-filtered sodium imaging. *Journal of Magnetic Resonance*, *202*(2), 239–244.

Mennecke, A. B., Nagel, A. M., Huhn, K., Linker, R. A., Schmidt, M., Rothhammer, V., ... Doerfler, A. (2021). Longitudinal sodium MRI of multiple sclerosis lesions: Is there added value of sodium inversion recovery MRI. *Journal of Magnetic Resonance Imaging*, *55*, 140–151.

Nagel, A. M., Bock, M., Hartmann, C., Gerigk, L., Neumann, J.-O., Weber, M.-A., ... Biller, A. (2011). The potential of relaxation-weighted sodium magnetic resonance imaging as demonstrated on brain tumors. *Investigative Radiology*, *46*(9), 539–547.

Nagel, A. M., Laun, F. B., Weber, M.-A., Matthies, C., Semmler, W., & Schad, L. R. (2009). Sodium MRI using a density-adapted 3D radial acquisition technique. *Magnetic Resonance in Medicine*, *62*(6), 1565–1573.

Nagel, A. M., Weber, M.-A., Wolf, M. B., & Semmler, W. (2012). 3D density-adapted projection reconstruction ^{23}Na-MRI with anisotropic resolution and field-of-view. In *Proceedings of the international society for magnetic resonance in medicine.*

Neumaier-Probst, E., Konstandin, S., Ssozi, J., Groden, C., Hennerici, M., Schad, L. R., & Fatar, M. (2015). A double-tuned ^{1}H/^{23}Na resonator allows ^{1}H-guided ^{23}Na-MRI in ischemic stroke patients in one session. *International Journal of Stroke*, *10*(SA100), 56–61.

Nielles-Vallespin, S., Weber, M.-A., Bock, M., Bongers, A., Speier, P., Combs, S. E., ... Schad, L. R. (2007). 3D radial projection technique with ultrashort echo times for sodium MRI: clinical applications in human brain and skeletal muscle. *Magnetic Resonance in Medicine*, *57*(1), 74–81.

Nunes Neto, L. P., Madelin, G., Sood, T. P., Wu, C.-C., Kondziolka, D., Placantonakis, D., ... Jain, R. (2018). Quantitative sodium imaging and gliomas: a feasibility study. *Neuroradiology*, *60*(8), 795–802.

Ouwerkerk, R., Bottomley, P. A., Solaiyappan, M., Spooner, A. E., Tomaselli, G. F., Wu, K. C., & Weiss, R. G. (2008). Tissue sodium concentration in myocardial infarction in humans: A quantitative ^{23}Na MR imaging study. *Radiology*, *248*(1), 88–96.

Ouwerkerk, R., & Morgan, R. H. (2007). ^{23}Na MRI: from research to clinical use. *Journal of the American College of Radiology*, *4*(10), 739-741.

Pauly, J. (2006). Design of large-flip-angle half pulses. In *Proceedings of the international society for magnetic resonance in medicine.*

Pauly, J., Nishimura, D., & Macovski, A. (1989). A k-space analysis of small-tip-angle excitation. *Journal of Magnetic Resonance*, *81*(1), 43–56.

Pipe, J. G. (2000). Reconstructing MR images from undersampled data: data-weighting considerations. *Magnetic Resonance in Medicine*, *43*(6), 867–875.

Pohl, H. R., Wheeler, J. S., & Murray, H. E. (2013). Sodium and potassium in health and disease. In A. Sigel, H. Sigel, & R. K. Sigel (Eds.), *Interrelations between essential metal ions and human diseases* (Vol. 13, pp. 29–47). Springer Netherlands.

Qian, Y., Zhao, T., Wiggins, G. C., Wald, L. L., Zheng, H., Weimer, J., & Boada, F. E. (2012). Sodium imaging of human brain at 7 T with 15-channel array coil. *Magnetic Resonance in Medicine*, *68*(6), 1807–1814.

Qian, Y., Zhao, T., Zheng, H., Weimer, J., & Boada, F. E. (2012). High-resolution sodium imaging of human brain at 7T. *Magnetic Resonance in Medicine*, *68*(1), 227–233.

Ra, J. B., Hilal, S. K., Oh, C. H., & Mun, I. K. (1988). In vivo magnetic resonance imaging of sodium in the human body. *Magnetic Resonance in Medicine*, *7*(1), 11–22.

Rahmer, J., Börnert, P., Groen, J., & Bos, C. (2006). Three-dimensional radial ultrashort echo-time imaging with T_2 adapted sampling. *Magnetic Resonance in Medicine*, *55*(5), 1075–1082.

Rooney, W. D., & Springer, C. S. (1991). A comprehensive approach to the analysis and interpretation of the resonances of spins 3/2 from living systems. *NMR in Biomedicine*, *4*(5), 209–226.

Rooney, W. D., & Springer Jr, C. S. (1991). The molecular environment of intracellular sodium: ^{23}Na NMR relaxation. *NMR in Biomedicine*, *4*(5), 227–245.

Saff, E. B., & Kuijlaars, A. B. (1997). Distributing many points on a sphere. *The mathematical intelligencer*, *19*(1), 5–11.

Shekar, S. C., Tang, J. A., & Jerschow, A. (2010). Dynamics of I=3/2 nuclei in isotropic slow motion, anisotropic and partially ordered phases. *Concepts in Magnetic Resonance Part A*, *36*(6), 362–387.

Shymanskaya, A., Worthoff, W. A., Stoffels, G., Lindemeyer, J., Neumaier, B., Lohmann, P., ... Shah, N. J. (2020). Comparison of [^{18}F] fluoroethyltyrosine

PET and sodium MRI in cerebral gliomas: A pilot study. *Molecular Imaging and Biology*, *22*(1), 198–207.

Somjen, G. G. (2004). *Ions in the brain: normal function, seizures, and stroke*. Oxford University Press.

Stobbe, R. (2010). *Sodium MRI optimization for the human head with application to acute stroke* (PhD thesis). University of Alberta.

Stobbe, R., & Beaulieu, C. (2005). In vivo sodium magnetic resonance imaging of the human brain using soft inversion recovery fluid attenuation. *Magnetic Resonance in Medicine*, *54*(5), 1305–1310.

Stobbe, R., & Beaulieu, C. (2008a). Advantage of sampling density weighted apodization over postacquisition filtering apodization for sodium mri of the human brain. *Magnetic Resonance in Medicine*, *60*(4), 981–986.

Stobbe, R., & Beaulieu, C. (2008b). Sodium imaging optimization under specific absorption rate constraint. *Magnetic Resonance in Medicine*, *59*(2), 345–355.

Stobbe, R., Boyd, A., Smyth, P., Emery, D., Cabrera, D. V., & Beaulieu, C. (2021). Sodium intensity changes differ between relaxation-and density-weighted MRI in multiple sclerosis. *Frontiers in Neurology*, *12*.

Stobbe, R. W., & Beaulieu, C. (2014). Exploring and enhancing relaxation-based sodium MRI contrast. *Magnetic Resonance Materials in Physics, Biology and Medicine*, *27*(1), 21–33.

Stolte, H., Hare, D., & Boylan, J. (1972). D-glucose and fluid reabsorption in proximal surface tubule of the rat kidney. *Pflügers Archiv*, *334*(3), 193–206.

Syeda, W., Blunck, Y., Kolbe, S., Cleary, J. O., & Johnston, L. A. (2019). A continuum of T_2^* components: Flexible fast fraction mapping in sodium MRI. *Magnetic Resonance in Medicine*, *81*(6).

Syková, E., & Nicholson, C. (2008). Diffusion in brain extracellular space. *Physiological Reviews*, *88*(4), 1277–1340.

Tanase, C., & Boada, F. E. (2005a). Algebraic description of spin 3/2 dynamics in NMR experiments. *Journal of Magnetic Resonance*, *173*(2), 236–253.

Tanase, C., & Boada, F. E. (2005b). Triple-quantum-filtered imaging of sodium in presence of B_0 inhomogeneities. *Journal of Magnetic Resonance*, *174*(2), 270–278.

Thulborn, K., Lui, E., Guntin, J., Jamil, S., Sun, Z., Claiborne, T. C., & Atkinson, I. C. (2016). Quantitative sodium MRI of the human brain at 9.4 T provides assessment of tissue sodium concentration and cell volume fraction during normal aging. *NMR in Biomedicine*, *29*(2), 137–143.

Thulborn, K. R. (2018). Quantitative sodium MR imaging: A review of its evolving role in medicine. *NeuroImage*, *168*, 250–268.

Tsai, C.-M., & Nishimura, D. G. (2000). Reduced aliasing artifacts using variable-density k-space sampling trajectories. *Magnetic Resonance in Medicine*, *43*, 452–458.

Tsang, A., Stobbe, R. W., & Beaulieu, C. (2012). Triple-quantum-filtered sodium imaging of the human brain at 4.7 T. *Magnetic Resonance in Medicine*, *67*(6), 1633–1643.

Utzschneider, M., Müller, M., Gast, L. V., Lachner, S., Behl, N. G., Maier, A., ... Nagel, A. M. (2021). Towards accelerated quantitative sodium MRI at 7T in the skeletal muscle: Comparison of anisotropic acquisition and compressed sensing techniques. *Magnetic Resonance Imaging*, *75*, 72–88.

van der Maarel, J. R. (2003a). Thermal relaxation and coherence dynamics of spin 3/2. II. Strong radio-frequency field. *Concepts in Magnetic Resonance*, *19A*(2), 117–133.

van der Maarel, J. R. (2003b). Thermal relaxation and coherence dynamics of spin 3/2. I. Static and fluctuating quadrupolar interactions in the multipole basis. *Concepts in Magnetic Resonance*, *19A*(2), 97–116.

Wheaton, A. J., Borthakur, A., Shapiro, E. M., Regatte, R. R., Akella, S. V., Kneeland, J. B., & Reddy, R. (2004). Proteoglycan loss in human knee cartilage: quantitation with sodium MR imaging—feasibility study. *Radiology*, *231*(3), 900–905.

Wilferth, T., Gast, L. V., Lachner, S., Behl, N. G., Schmidt, M., Dörfler, A., ... Nagel, A. M. (2020). X-nuclei MRI on a 7T MAGNETOM terra: Initial experiences. *MAGNETOM Flash*, *76*, 45–51.

Wilferth, T., Gast, L. V., Stobbe, R. W., Beaulieu, C., Hensel, B., Uder, M., & Nagel, A. M. (2019). ^{23}Na MRI of human skeletal muscle using long inversion recovery pulses. *Magnetic Resonance Imaging*, *63*, 280–290.

Wilferth, T., Müller, M., Gast, L. V., Ruck, L., Meyerspeer, M., Lopez Kolkovsky, A. L., ... Nagel, A. M. (2022). Motion-corrected ^{23}Na MRI of the human brain using interleaved ^{1}H 3D navigator images. *Magnetic Resonance in Medicine*, *88*(1), 309–321.

Winkelmann, S., Schaeffter, T., Koehler, T., Eggers, H., & Doessel, O. (2006). An optimal radial profile order based on the Golden Ratio for time-resolved MRI. *IEEE transactions on medical imaging*, *26*(1), 68–76.

Wittrich, M. L., Nagel, A. M., Schmitter, S., Bachert, P., Ladd, M. E., & Kratzer, F. J. (2022). 2d 23Na imaging using half-VERSE pulses. In *Proceedings of the international society for magnetic resonance in medicine.*

Wong, E. C., Liu, T. T., Luh, W.-M., Frank, L. R., & Buxton, R. B. (2001). T_1 and T_2 selective method for improved SNR in CSF-attenuated imaging: T_2-FLAIR. *Magnetic Resonance in Medicine*, *45*(3), 529–532.

Worthoff, W. A., Shymanskaya, A., & Shah, N. J. (2019). Relaxometry and quantification in simultaneously acquired single and triple quantum filtered sodium MRI.

Magnetic Resonance in Medicine, *81*(1), 303–315.

Wu, C., Blunck, Y., & Johnston, L. A. (2022). The "Spin-3/2 Bloch Equation": System matrix formalism of excitation, relaxation, and off-resonance effects in biological tissue. *Magnetic Resonance in Medicine*, *88*, 1370-1379.

Yu, Z., Madelin, G., Sodickson, D. K., & Cloos, M. A. (2020). Simultaneous proton magnetic resonance fingerprinting and sodium MRI. *Magnetic Resonance in Medicine*, *83*(6), 2232–2242.

Zhang, Y., Brady, M., & Smith, S. (2001). Segmentation of brain MR images through a hidden markov random field model and the expectation-maximization algorithm. *IEEE transactions on medical imaging*, *20*(1), 45–57.